

Radiative Forcings of Well-Mixed Greenhouse Gases

by

Brendan Byrne

B.Sc., University of Victoria, 2012

A Thesis Submitted in Partial Fulfillment of the  
Requirements for the Degree of

MASTER OF SCIENCE

in the School of Earth and Ocean Sciences

© Brendan Byrne, 2014  
University of Victoria

All rights reserved. This thesis may not be reproduced in whole or in part, by  
photocopying or other means, without the permission of the author.

Radiative Forcings of Well-Mixed Greenhouse Gases

by

Brendan Byrne

B.Sc., University of Victoria, 2012

Supervisory Committee

---

Dr. C. Goldblatt, Supervisor  
(School of Earth and Ocean Sciences)

---

Dr. A. Monahan, Departmental Member  
(School of Earth and Ocean Sciences)

---

Dr. D. Atkinson, Outside Member  
(Department of Geography)

## Supervisory Committee

---

Dr. C. Goldblatt, Supervisor  
(School of Earth and Ocean Sciences)

---

Dr. A. Monahan, Departmental Member  
(School of Earth and Ocean Sciences)

---

Dr. D. Atkinson, Outside Member  
(Department of Geography)

---

## ABSTRACT

A change in the atmospheric inventory of a greenhouse gas produces a radiative forcing on the atmosphere which results in climatic change. Thus to understand climate change resulting from perturbations to atmospheric greenhouse gas concentrations it is necessary to quantify the radiative forcing. Here, radiative forcings are presented for large changes in atmospheric  $\text{CO}_2$ ,  $\text{CH}_4$ , and  $\text{N}_2\text{O}$  in the modern atmosphere and large changes in atmospheric  $\text{CO}_2$ ,  $\text{CH}_4$  and 18 other gases for the Archean atmosphere.

For the modern Earth, I present new calculations of radiative forcing at very high concentrations of  $\text{CO}_2$ ,  $\text{CH}_4$ , and  $\text{N}_2\text{O}$ , relevant to extreme anthropogenic climate change and paleoclimate studies.  $\text{CO}_2$  forcing is calculated over the range 100 ppmv to 50,000 ppmv.  $\text{CH}_4$ , and  $\text{N}_2\text{O}$  forcings are calculated over the range 100 ppbv to 100 ppmv. The sensitivity of these calculations to spatial averaging and tropopause definition are examined. I compare our results with the “simplified expressions” reported by IPCC, and find significant differences at high greenhouse gas concentrations. I provide new simplified expressions which agree much better with the calculated forcings, and suggest that these expressions be used in place of the IPCC expressions. Additionally, I provide meridionally resolved forcings which may be used to force simple and intermediate complexity climate models.

For the Archean Earth, I present new calculations of radiative forcing for CO<sub>2</sub> (10<sup>-6</sup>–1 bar), CH<sub>4</sub> (500 ppbv–10,000 ppmv) and 18 other gases (10 ppbv–10 ppmv). I aim to provide a set of radiative forcing and overlap calculations which can be used as a standard for comparisons. Radiative forcings are calculated for atmospheres with various N<sub>2</sub> inventories (0.5, 1, and 2 bar). The effect of overlap and atmospheric pressure on radiative forcing are examined. The CO<sub>2</sub> radiative forcings are consistent with previous work, however, I find significantly more shortwave absorption by CH<sub>4</sub> than previously reported which may limit warming above 100 ppmv. For the 18 other gases, I find that significant radiative forcings result from low concentrations (<1 ppmv). These forcings are compared to those given in the literature.

# Contents

<b>Supervisory Committee</b>	<b>ii</b>
<b>Abstract</b>	<b>iii</b>
<b>Table of Contents</b>	<b>v</b>
<b>List of Tables</b>	<b>vii</b>
<b>List of Figures</b>	<b>viii</b>
<b>Acknowledgements</b>	<b>ix</b>
<b>1 Introduction</b>	<b>1</b>
<b>2 Background</b>	<b>4</b>
2.1 Molecular Absorption . . . . .	4
2.2 Radiative Transfer . . . . .	8
2.3 Energy Budget and Radiative Forcing . . . . .	10
2.4 Radiative Transfer Codes . . . . .	13
2.4.1 Line-By-Line . . . . .	13
2.4.2 Band Models . . . . .	14
2.4.3 Correlated $\kappa$ . . . . .	14
2.4.4 Mapping Transformations . . . . .	15
2.4.5 Radiative Transfer models in the context of this work . . . . .	18
<b>3 Modern Earth</b>	<b>20</b>
3.1 Introduction . . . . .	20
3.2 Methods . . . . .	21
3.2.1 Radiative Transfer Calculation . . . . .	21
3.2.2 Atmosphere Profiles . . . . .	22

3.2.3	Cloud Climatology . . . . .	23
3.2.4	Radiative Forcing Definition . . . . .	23
3.2.5	Tropopause Definition . . . . .	24
3.3	Results . . . . .	24
3.3.1	Calculated Forcings . . . . .	24
3.3.2	Overlap . . . . .	26
3.3.3	IPCC fits . . . . .	26
3.3.4	New Fits . . . . .	29
3.3.5	Meridional Variation in $F_i$ . . . . .	31
3.4	Conclusions . . . . .	33
<b>4</b>	<b>Early Earth</b>	<b>34</b>
4.1	Introduction . . . . .	34
4.2	Methods . . . . .	37
4.2.1	Overview . . . . .	37
4.2.2	Spectra . . . . .	37
4.2.3	Atmospheric Profile . . . . .	42
4.2.4	Radiative Forcing Calculations . . . . .	44
4.3	Results and Discussion . . . . .	45
4.3.1	CO <sub>2</sub> . . . . .	45
4.3.2	CH <sub>4</sub> . . . . .	48
4.3.3	Trace Gases . . . . .	52
4.4	Conclusions . . . . .	60
<b>5</b>	<b>Conclusions</b>	<b>61</b>
<b>A</b>	<b>Additional Information</b>	<b>64</b>
A.1	Upward and Downward Flux Equations . . . . .	64
A.2	Sensitivity . . . . .	65
A.3	Modern Earth Tables . . . . .	65
A.4	Early Earth Tables . . . . .	70
	<b>Bibliography</b>	<b>83</b>

# List of Tables

Table 3.1 IPCC Radiative Forcing Fits . . . . .	28
Table 3.2 New Radiative Forcing Fits . . . . .	29
Table A.1 $F_i$ ( $\text{Wm}^{-2}$ ) for $\text{CO}_2$ as a function of latitude and concentrations	67
Table A.2 $F_i$ ( $\text{Wm}^{-2}$ ) for $\text{CH}_4$ as a function of latitude and concentrations	68
Table A.3 $F_i$ ( $\text{Wm}^{-2}$ ) for $\text{N}_2\text{O}$ as a function of latitude and concentrations .	69
Table A.4 Atmospheric structure for GAM . . . . .	71
Table A.5 Atmospheric structure for $00^\circ$ - $15^\circ$ . . . . .	72
Table A.6 Atmospheric structure for $15^\circ$ - $30^\circ$ . . . . .	73
Table A.7 Atmospheric structure for $30^\circ$ - $45^\circ$ . . . . .	74
Table A.8 Atmospheric structure for $45^\circ$ - $60^\circ$ . . . . .	75
Table A.9 Atmospheric structure for $60^\circ$ - $75^\circ$ . . . . .	76
Table A.10 Atmospheric structure for $75^\circ$ - $90^\circ$ . . . . .	77
Table A.11 Cloud climatology for GAM Profile . . . . .	78
Table A.12 Cloud climatology for $00^\circ$ - $15^\circ$ . . . . .	78
Table A.13 Cloud climatology for $15^\circ$ - $30^\circ$ . . . . .	78
Table A.14 Cloud climatology for $30^\circ$ - $45^\circ$ . . . . .	78
Table A.15 Cloud climatology for $45^\circ$ - $60^\circ$ . . . . .	78
Table A.16 Cloud climatology for $60^\circ$ - $75^\circ$ . . . . .	78
Table A.17 Cloud climatology for $75^\circ$ - $90^\circ$ . . . . .	79
Table A.18 Atmospheric structure for 0.5 bar of $\text{N}_2$ . . . . .	80
Table A.19 Atmospheric structure for 1 bar of $\text{N}_2$ . . . . .	81

# List of Figures

Figure 2.1 Optical depth and outgoing longwave radiation . . . . .	11
Figure 2.2 Correlated- $\kappa$ Transformation . . . . .	16
Figure 2.3 Spectral Mapping for layer A . . . . .	16
Figure 2.4 Spectral Mapping for layers B and C . . . . .	17
Figure 3.1 Atmospheric profiles . . . . .	22
Figure 3.2 Radiative forcings . . . . .	25
Figure 3.3 Absorption cross-sections . . . . .	27
Figure 3.4 Reduction in $F_i$ due to overlap . . . . .	28
Figure 3.5 Simplified expressions for radiative forcings . . . . .	30
Figure 3.6 Calculated $F_i$ as a function of concentration and latitude . . . . .	32
Figure 4.1 Absorption cross-sections. . . . .	39
Figure 4.2 Atmospheric Profiles . . . . .	43
Figure 4.3 CO <sub>2</sub> Radiative Forcings . . . . .	45
Figure 4.4 Surface temperature as a function of CO <sub>2</sub> concentration for 0.8 S <sub>0</sub>	47
Figure 4.5 Radiative Forcing for CH <sub>4</sub> . . . . .	49
Figure 4.6 Solar absorption cross-sections . . . . .	50
Figure 4.7 Downward shortwave flux . . . . .	51
Figure 4.8 Surface temperature as a function of CH <sub>4</sub> concentration for 0.8 S <sub>0</sub>	53
Figure 4.9 Spectral absorption of blackbody emissions. . . . .	55
Figure 4.10 Trace gas radiative forcings . . . . .	56
Figure 4.11 Overlap with CO <sub>2</sub> and CH <sub>4</sub> . . . . .	58
Figure 4.12 Trace gas overlap . . . . .	58
Figure 4.13 Calculated Radiative forcings and inferred radiative forcings from literature . . . . .	59
Figure A.1 Sensitivity Study . . . . .	66

## ACKNOWLEDGEMENTS

I am grateful to my supervisor, Dr. Colin Goldblatt, whose enthusiasm and dedication have made this experience very enjoyable. I greatly appreciate the time Colin has dedicated to help me form research questions, carry out research and communicate results; his efforts have greatly improved my skills as a scientist.

I thank my thesis committee members Dr. David Atkinson and Dr. Adam Monahan for helping me along the way.

I thank Dr. Ty Robinson for help with SMART and sharing his knowledge of atmospheric radiation. His help has made my more frustrating moments with SMART much shorter.

I thank the climate lab staff for their support. I would also like to thank the fellow climate lab students who have helped me learn the ropes of being a grad student and have made being a graduate student fun.

I am thankful for financial support from the Natural Sciences and Engineering Research Council of Canada (NSERC) CREATE Training Program and from a University of Victoria graduate fellowship.

I am indebted to my parents, Aidan and Karen who have always supported and encouraged me and nurtured my interest in science. Without their ceaseless support I could never have made it this far. And to my siblings Glynis and Liam, who have always been supportive. I would like to thank my partner, Adeeba, for her loving support and for always believing in me.

# Chapter 1

## Introduction

This thesis concerns the radiative forcing produced by extreme changes in greenhouse concentrations for both modern (Phanerozoic) and Archean climate. Understanding the radiative imbalance is important because it initiates climate feedbacks which warm or cool the Earth's surface to restore radiative equilibrium. I quantify radiative imbalances using radiative forcing, the change in the net flux of radiation at the tropopause due to a change in greenhouse gas concentration, which has been used extensively in climate change research (Hansen et al., 1997, 2005; IPCC, 2013). This work is relevant to the modern atmosphere in the context of extreme anthropogenic greenhouse gas emissions and Phanerozoic climate change in general, and to the Archean in the context of the faint young sun problem.

### Modern Earth

As radiative transfer models are rather specialist codes, it is very common to refer to empirical fits or “simplified expressions” of radiative forcing as given by the Intergovernmental Panel on Climate Change, first in IPCC (1990) and updated in IPCC (2001). These expressions are intended for relatively small perturbations in greenhouse gases, relevant to short term anthropogenic climate change. These commonly used expressions have been fitted to radiative forcings for concentrations of up to 1000 ppmv of CO<sub>2</sub>, and 5 ppmv of CH<sub>4</sub> and N<sub>2</sub>O. The limitations of these simplified expressions at higher concentrations have not been documented to my knowledge. Thus the accuracy of these expressions for use in extreme anthropogenic climate change or Phanerozoic paleoclimate studies are unknown.

Here we calculate radiative forcings for CO<sub>2</sub> over the range 100 ppmv to 50,000 ppmv,

and  $\text{CH}_4$  and  $\text{N}_2\text{O}$  forcings over the range 100 ppbv to 100 ppmv. The sensitivity of our calculations to spatial averaging and tropopause definition are examined. I compare our results with the simplified expressions given in IPCC (2001) and find significant differences at high greenhouse gas concentrations. I provide new simplified expressions which agree much better with the calculated forcings and suggest that these expressions be used in place of the IPCC expressions.

Simplified expressions of radiative forcing are commonly used to force climate models ranging from simple box models to models of intermediate complexity (e.g., Weaver et al., 2001). However, there is significant meridional variation in radiative forcing. Therefore, using the IPCC expressions neglects the spatial variation in radiative forcing. We provide meridionally resolved forcings which may be used to force simple and intermediate complexity climate models.

### **Archean Earth**

The standard stellar model predicts that the luminosity of a star increases over its main-sequence lifetime, so, the sun is 30% brighter now than it was when the solar system formed. Despite a dimmer sun, during the Archean (3.8–2.5 Gyr ago) geologic evidence points to surface temperatures similar to today (Donn et al., 1965). This apparent contradiction is known as the faint young sun problem (FYSP). It is thought that warm surface temperatures were sustained, primarily, though a stronger greenhouse effect produced by elevated concentrations of  $\text{CO}_2$ ,  $\text{CH}_4$ , and possibly other greenhouse gases.

Previous studies have examined the warming produced by elevated greenhouse gas concentrations but have typically performed calculations with fast radiative transfer models which may perform quite poorly for large changes in greenhouse gases from the modern climate (Goldblatt et al., 2009a). Examining the Archean greenhouse often involves calculating the radiative effects of greenhouse gases over concentration ranges never before examined. These calculations are often performed in one off calculations with no standard set of forcings available for comparison. The absence of a standard set of forcings has led to errors going undetected. For example, calculations of the warming exerted by  $\text{CH}_4$  was significantly overestimated by Pavlov et al. (2000) due to an error in the numbering of spectral intervals, this mistake went undetected for several years. Furthermore, it would be useful to compare the relative strengths of potential early Earth greenhouse gases. However, it is difficult to compare green-

house gases from the literature because of differences in methods and models between studies.

Here we use an accurate radiative transfer model to calculate radiative forcings of  $\text{CO}_2$ ,  $\text{CH}_4$  and 18 other greenhouse gases on an early Earth atmosphere. The sensitivity of our calculations to atmospheric pressure and background greenhouse gases concentrations are examined. This provides a basis set of radiative forcings which new calculations can be compared to. We compare our results to previous work on the problem.

## **Layout**

Chapter 2 gives a background to longwave molecular absorption, radiative transfer and radiative forcing. Chapter 3 provides radiative forcing calculations in the context of Phanerozoic climate. We compare our calculations with IPCC simplified expressions, and provide improved simplified expressions and meridionally resolved forcings. Chapter 4 provides radiative forcing calculations in the context of the Archean climate. We examine the sensitivity of our results to unconstrained climate parameters and compare our results with those reported in the literature.

The work within this thesis is at a variety of stages with respect to publication. Chapter 3 is already published (Byrne and Goldblatt, 2014). Chapter 4 is soon to be submitted. Chapter 3 and 4 are not modified from the published/submitted versions.

# Chapter 2

## Background

The planetary energy budget is a balance between absorbed incoming solar radiation and outgoing thermal emissions from the Earth's surface and atmosphere. The sun, which has an effective emitting temperature of 5777 K, primarily emits radiation in the wavenumber region  $2000\text{--}30000\text{ cm}^{-1}$  ( $0.33\text{--}5\text{ }\mu\text{m}$ ), whereas, the effective emitting temperature of the Earth's surface is 289 K and emits primarily in the  $50\text{--}2000\text{ cm}^{-1}$  ( $5\text{--}200\text{ }\mu\text{m}$ ) region. For this reason, solar radiation is termed shortwave and thermal radiation is termed longwave.

To understand the Earth's energy balance in detail, it is necessary to have an understanding of the physics of molecular absorption and the propagation of radiation in the atmosphere. I introduce the physics of these phenomena in sections 2.1 and 2.2 and introduce radiative forcing (section 2.3). Finally, I describe how these physical phenomena are modelled using radiative transfer codes (section 2.4).

### 2.1 Molecular Absorption

Thermal radiation is absorbed or emitted by changing a molecule's vibrational and rotation state. A change from one state to another is associated with a quantum of energy,  $E_0$ , such that a photon of frequency  $\nu_0$  with energy  $E_0 = h\nu_0$  can be absorbed or emitted. Each energy transition is associated with a unique frequency of radiation called a spectral absorption line.

For a single spectral line, centred at  $\nu_0$ , the absorption coefficient at  $\nu$  is given by the product of the strength of the line,  $S(T)$ , and the shape of the line,  $f(\nu - \nu_0)$ ,

$$\kappa(\nu - \nu_0) = S(T) f(\nu - \nu_0), \quad (2.1)$$

and has dimensions of area per mass.

Line strength is dependent on the quantum mechanical transition probability between energy levels and the number of molecules in the initial energy state. The number of molecules in a given energy state is dependent on temperature and thus the line strength is dependent on temperature. However, line strength is independent of pressure.

Conversely, line shape is dependent on pressure but not temperature. The line shape is normalized so that it covers an increasing frequency range at the expense of the magnitude of the line centre,

$$\int_{-\infty}^{\infty} f(\nu - \nu_0) d(\nu - \nu_0) = 1. \quad (2.2)$$

If the line were monochromatic then  $f(\nu - \nu_0) = \delta(\nu - \nu_0)$ , where  $\delta(\nu - \nu_0)$  is the Dirac delta function, however, real lines differ from this because of broadening effects.

## Broadening

Broadening is the widening of the line shape to cover a larger range of frequencies. Broadening does not increase the amount of absorption directly because the line shape is normalized. However, line broadening of strong lines can result in an increase in absorption indirectly. If the line center is saturated so that it absorbs all the incident light, then broadening the line will increase absorption in the line wings which are not saturated.

The two most important broadening mechanisms for planetary atmospheres are Doppler and pressure broadening. Doppler broadening is due to the Doppler effect (change in frequency of a photon absorbed due to relative motion of the molecule) and is primarily of importance at low pressures, such as the middle stratosphere (Pierrehumbert, 2010). Pressure (or collisional) broadening is caused by elastic collisions between molecules. As molecules interact they exchange energy which allows a molecule to absorb a photon with different energy than the absorption line, so that energy from the collision and photon combine to the energy required for the transition. Pressure broadening is a function of pressure, and most important in the troposphere (lower atmosphere).

## Continuum Absorption

The line absorption described above is not the whole story. There is absorption caused by more complex interactions between matter and radiation which can cause significant absorption. This absorption is termed continuum absorption because it is relatively smooth as a function of wavenumber, and is caused by 1) far-wing absorption 2) quasi-bound dimers, and 3) bound dimers<sup>1</sup>.

1. Far-wing absorption is caused by collisions between molecules. It is essentially pressure broadening where the molecules spend a longer period of time together; the theory of far wing absorption is derived from assuming collisions take an infinite length of time (Ma et al., 2008). The far wing contribution of the strong spectral lines from neighbouring bands accumulates to cause significant absorption. There is at present no theory for collisions that take place at a finite length and thus far-wing absorption is quite uncertain. A typical practice in radiative transfer models is to include far wing absorption in the continuum spectra.
2. Quasi-bound (or metastable) dimers are a monomer pair which are temporarily stabilized as dimers but have a total internal energy exceeding the dissociation threshold. Quasi-bound states can form when an excess of kinetic energy over the dissociation limit is temporarily transferred to the non-dissociative internal degrees of freedom such as the internal rotation of the monomers within a pair (Ptashnik et al., 2011). The broadening mechanism of quasi-bound dimers is caused by their short lifetime due to the quantum mechanical uncertainty relation for energy (called lifetime broadening, Ptashnik et al., 2011).
3. Bound dimers are dimers formed at an effective potential energy less than zero so that energy needs to be added for the dimer to dissociate. Bound dimers require a third body to remove energy for their formation and to make up energy for their dissociation. Near atmospheric temperatures the width and shapes of dimer lines are uncertain due to high spectral absorption densities (Ptashnik et al., 2011).

At temperatures and pressures characteristic of the atmosphere it is difficult to experimentally determine which physical phenomena are primarily responsible for

---

<sup>1</sup>Dimers are complexes created by two molecules (or monomers) which act optically as a new molecule.

continuum absorption and to what degree. A further complication is that the portion of the continuum attributed to each mechanism is different for different wavenumber bands and at different temperatures. Therefore, continuum absorption is generally treated empirically.

In practice, continuum absorption is defined as the difference between the measured absorption and the absorption calculated from molecular (monomer) spectral lines. Numerically, continuum absorption is dependent on how line absorption is represented. Line absorption is only calculated to a certain distance from the line center (called cutoff width), but this distance varies between models (Halevy et al., 2009a). Radiative transfer calculations have been found to be more sensitive to line cutoff width than integration step or line shape (Hua et al., 2008).

Continuum absorption becomes increasingly important at high concentrations. As the concentration of a gas is increased from zero, strong absorption lines cause the most absorption. As the line centres become saturated, the wings perform most of the absorption. Only when the concentration is very high does the continuum spectra become important. Thus, in the calculations performed in this work the continuum absorption of H<sub>2</sub>O and CO<sub>2</sub> are the most important.

In this work we examine CO<sub>2</sub> radiative forcings at very high partial pressures ( $\leq 1$  bar). The continuum becomes very important at concentrations greater than 0.1 bar. Halevy et al. (2009b) show that different parametrizations of line and continuum absorption in different radiative transfer models can lead to large differences in outgoing longwave radiation at high CO<sub>2</sub> concentrations. The radiative transfer code used in this work, the Spectral Mapping for Atmospheric Radiative Transfer (SMART) code, does not include a separate continuum absorption spectra, but instead uses a  $\chi$ -factor to reduce the opacity of the Voight line shape out to 1000 cm<sup>-1</sup> from the line center to match the background absorption. We add to this collision induced absorption (CIA) which has been updated with recent results of Wordsworth et al. (2010), where CIA is the absorption spectra due to inelastic collisions. We believe that our radiative transfer model is as accurate as possible given the poor understanding of continuum absorption.

### **HITRAN database**

In this work we use line-by-line spectroscopic parameters from the HITRAN 2012 database for high resolution molecular absorption and radiance calculations. Line

parameters supplied in the HITRAN database include intensity, air-broadened half width, self broadened half width, and the temperature-dependence coefficient. The absorption coefficient can be calculated as a function of wavenumber from these parameters. For this work we use the LBLABC code which calculates the absorption from each line to create a spectra of absorption coefficients. The absorption coefficients can then be compared with measured absorption cross-sections ( $\sigma$ ) using the relation,

$$\sigma = \kappa \cdot M_w \quad (2.3)$$

where  $M_w$  is molecular weight.

## 2.2 Radiative Transfer

Assume that radiation is isotropic in the meridional and zonal directions, so that it can be expressed solely as a function of height. This is known as the plane-parallel approximation. The absorption of the light beam or optical depth ( $\tau_\nu^*$ ) of a monochromatic light mean with frequency  $\nu$  propagating a distance  $dz$  vertically in the atmosphere is given by,

$$\tau^*(\nu, p, T) \equiv \int_{z_1}^{z_2} \kappa(\nu, p, T) \rho dz, \quad (2.4)$$

assuming hydrostatic balance this can be written as a function of pressure,

$$\tau^*(\nu, p, T) = - \int_{p_1}^{p_2} \frac{\kappa(\nu, p, T) g dp}{g}$$

equation where  $g$  is the acceleration due to gravity. The optical depth can be thought of as the affinity of a gas to absorb or emit radiation, and is a function of atmospheric composition, pressure and temperature. For a beam propagating at an angle  $\theta$  to the vertical, the optical depth can be written as,

$$\tau_\nu \equiv \frac{\tau_\nu^*}{\cos\theta}. \quad (2.5)$$

If  $\tau_\nu^*$  is taken to be the vertical co-ordinate, the energy budget of a beam of radiation of intensity,  $I$ , at an angle,  $\theta$  (denoted  $\hat{n}$ ), with blackbody emissions,  $B$ , is

given by,

$$I(\tau_\nu^* + \delta\tau_\nu^*, \hat{n}, \nu) = \left(1 - \frac{\delta\tau_\nu^*}{\cos\theta}\right) I(\tau_\nu^*, \hat{n}, \nu) + B(\nu, T(\tau_\nu^*)) \frac{\delta\tau_\nu^*}{\cos\theta}. \quad (2.5)$$

In the limit that  $\delta\tau_\nu^* \rightarrow d\tau_\nu^*$ , this balance can be written as,

$$\frac{d}{d\tau_\nu^*} I(\tau_\nu^*, \hat{n}, \nu) = -\frac{1}{\cos\theta} (I(\tau_\nu^*, \hat{n}, \nu) - B(\nu, T(\tau_\nu^*))) \quad (2.5)$$

This is the general form of the Schwarzschild equation<sup>2</sup> for radiative transfer without scattering. The intensity of a beam is diminished by molecular absorption and strengthened by backbody emissions. This equation is used as the basis for calculating radiative transfer in the atmosphere.

A very useful extension of the Schwarzschild equation are the upward and downward flux equations which represent the intensity of radiation moving upwards and downwards through the atmosphere,

$$\frac{d}{d\tau_\nu} I_+ = -I_+ + \pi B(\nu, T(\tau)), \quad (2.5)$$

$$\frac{d}{d\tau_\nu} I_- = I_- - \pi B(\nu, T(\tau)), \quad (2.5)$$

where,  $I_+$  and  $I_-$  represent the net flux of radiation moving up and down in the atmosphere (derivation given in appendix A.1). The solutions for these equations are given by,

$$I_+(\tau_\nu, \nu) = I_+(\tau_0) e^{-(\tau_\nu - \tau_0)} + \int_0^{\tau_\nu} \pi B(\nu, T(\tau')) e^{-(\tau_\nu - \tau')} d\tau', \quad (2.5)$$

$$I_-(\tau_\nu, \nu) = I_-(\tau_\infty) e^{-(\tau_\infty - \tau_\nu)} + \int_{\tau_\nu}^{\tau_\infty} \pi B(\nu, T(\tau')) e^{-(\tau' - \tau_\nu)} d\tau' \quad (2.5)$$

The weighting function appearing in equations 2.5 and 2.5 is known as the transmission function,

$$\mathcal{T}_\nu \equiv e^{-\int d\tau_\nu} \quad (2.5)$$

The transmission function is a very sensitive function of optical depth. For optical depths less than 1 it increases very rapidly and there is very little radiation emitted

---

<sup>2</sup>Named after the astrophysicist Karl Schwarzschild, who is most famous for finding the first exact solution to the Einstein field equations while serving in the German army during world war 1.

or absorbed; this is called the optically thin regime. For optical depths greater than 1 the transmission function decreases rapidly and nearly all of the radiation is being absorbed and re-emitted; this is called the optically thick regime. Therefore, most of the radiation emitted to space from the atmosphere occurs when the optical thickness is in the order of unity, and the converse for radiation absorbed from space. Since optical depth is wavenumber dependent, an optical depth of unity occurs at different pressures for different wavenumbers.

## 2.3 Energy Budget and Radiative Forcing

Now consider how the optical depth of the atmosphere relates to the energy balance. Most outgoing longwave radiation is emitted from the atmospheric level at which the optical depth is of order unity. Due to greenhouse gases, the optical depth over the depth of the atmosphere is generally greater than 1 (figure 2.1) resulting in emissions from space originating in the atmosphere. An important exception is the water vapor window (800–1200  $\text{cm}^{-1}$ ) where  $\text{H}_2\text{O}$ ,  $\text{CO}_2$  and  $\text{CH}_4$  are not strong absorbers and much of the outgoing longwave radiation is from the surface.

The intensity of radiation emitted from an object is very sensitive to temperature. Because the temperature of the atmosphere varies with altitude, the intensity of radiation emitted to space is sensitive to the altitude at which it is emitted. Generally, energy is emitted below the atmospheric temperature inversion, where the temperature of the atmosphere cools with altitude. Thus, the greater the optical depth of a gas and the higher it emits radiation, the lower the intensity is.

Now consider a perturbation to a planetary energy balance by an increase in the concentration of a greenhouse gas. Most of the energy emitted from the atmosphere originates from the altitude at which the optical depth is of order unity. Increasing the concentration of a greenhouse gas increases the optical depth of the gas and moves the optical depth of unity to a higher atmospheric level. If this level is colder, less radiation will be emitted and the planet will have a net gain of energy. For example, in figure 2.1, the altitude of unity optical depth increases from pre-industrial concentrations to RCP8.5 (representative concentration pathway 8.5, Meinshausen et al., 2011) year 2250 concentrations at wavenumbers where  $\text{CO}_2$ ,  $\text{CH}_4$  and  $\text{N}_2\text{O}$  are optically thick. This results in a decrease in outgoing longwave radiation except at the peak of the 700  $\text{cm}^{-1}$   $\text{CO}_2$  absorption band where the emissions move to a higher point in the stratosphere where temperatures are warmer, resulting in a small

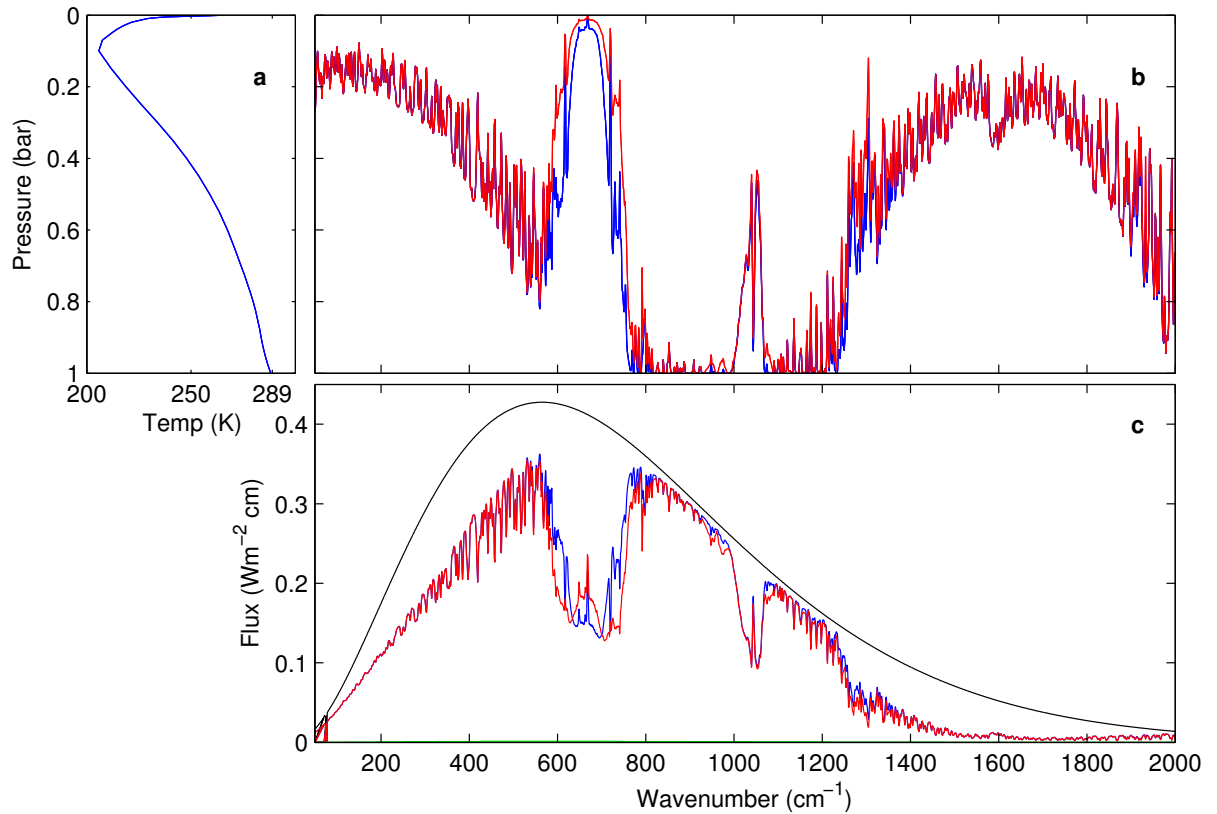


Figure 2.1: **Optical depth and outgoing longwave radiation.** (a) Atmospheric temperature profile. (b) Atmospheric pressure at which optical depth is unity for atmospheres with pre-industrial greenhouse gas concentrations (blue) and RCP8.5 year 2250 concentrations (red). (c) Top of atmosphere outgoing longwave radiation. Black curve shows surface emissions. Other colors are as in (b).

increase in the energy emitted.

A perturbation to the emitted longwave radiation will initiate a change in the atmospheric temperature structure to restore equilibrium. To understand the temperature response of the atmosphere to an initial perturbation it is very useful to consider the atmosphere above and below the tropopause separately. The imbalance of radiation below the tropopause is generally characterized by radiative forcing, defined as, the change in the net flux of radiation at the tropopause. Ramanathan et al. (1987) describe why the tropopause and stratosphere should be considered separately as follows,

“Within the troposphere the vertical mixing of sensible and latent heat by convection and large-scale motions is considered to be quite rapid in comparison to the time scales associated with radiative adjustments. As a result, the vertical distribution of the tropospheric temperature change is largely governed by dynamical processes, while the mass-weighted tropospheric temperature change is governed by the radiative forcing of the column. Hence as a first approximation, we can ignore the details of the vertical distribution of the tropospheric radiative forcing and focus, instead, on the radiative forcing of the entire surface-troposphere system. Since the surface-troposphere radiative forcing is simply the change in the net radiative flux at the tropopause, it is rather straightforward to assess the importance of trace gas radiative forcing. The only minor complication is that we have to account for changes in stratospheric temperature and long-wave emissions in order to compute the flux changed at the tropopause. Within the stratosphere, however, the timescales associated with radiative adjustments are comparable to, or faster than, those associated with dynamical processes. As a result, the magnitude of the stratospheric climate change is influenced strongly by the vertical distribution of the radiative heating rate perturbation within the stratosphere.”

Radiative forcing has been found to be particularly useful in understanding how changes in well-mixed greenhouse gases affect the climate. To first order, the radiative forcing due to changes in well-mixed greenhouse gases has been found to be directly proportional mean surface temperature change,

$$\Delta T = \lambda F \tag{2.5}$$

The climate sensitivity parameter,  $\lambda$ , relates the the change in surface temperature to radiative forcing through feedbacks. Feedbacks affect the planetary energy budget by changing the planetary albedo (e.g., cloud feedbacks), further increasing greenhouse gas concentrations (e.g. water vapor feedback), or changing the atmospheric structure (e.g., stratospheric adjustment). Uncertainties in the magnitude of these feedbacks makes it difficult to determine the exact value of the climate sensitivity parameter.

Of course, the relationship can become quite non-linear for large forcings which initiate non-linear climate feedbacks. Nevertheless, radiative forcing has been found to be the simplest and most effective first order measure of climate change. For more detailed analysis of climate response climate models are required.

## 2.4 Radiative Transfer Codes

To calculate radiative transfer in a non-homogeneous atmosphere, the atmosphere is broken up into a number of homogeneous layers. Within each layer the pressure, temperature and absorber concentration are taken to be constant but are different for each layer (Thomas and Stamnes, 2002). Line absorption is given by a chosen line profile that is parametrized by databases that contain information on line positions, strengths, and broadening parameters for all significant absorbing gases in the modern Earth's atmosphere.

Here we describe line-by-line, band, correlated- $\kappa$ , and spectral mapping radiative transfer models. Line-by-Line models are the most accurate but are very computationally expensive. Much more efficient radiative transfer models are required for running climate models. Therefore, band and correlated- $\kappa$  models are typically used. The vast majority of radiative forcing calculations have been performed using either band or correlated- $\kappa$  models and thus it is important that we outline the limitations of these models here. In this thesis a spectral mapping model is used at line-by-line resolution to ensure results are reliable.

### 2.4.1 Line-By-Line

Line-by-Line calculations are radiative transfer calculations with very fine resolution over wavenumber so that the variation in absorption is captured. For each wavenumber interval, the absorption is summed over the individual contributions of all the

lines in the vicinity of the interval as they add to the absorption (Petty, 2006).

Line-by-line calculations are extremely computationally expensive and are, in general, not used for atmospheric radiation calculations within climate models, but are used as the standard that all other numerical methods are compared to. Any errors that enter in line-by-line calculations are perpetuated in other numerical methods. It is therefore very important to know where uncertainties originate in these calculations. For broadband radiative transfer, Goody and Yung (1995) state that the agreement between the line-by-line calculations and observations is generally within 10%. They cite uncertainties in the spectroscopic data, local variations in temperature and departure from a strictly stratified atmosphere as the cause of the discrepancy. There are a number of parameter choices that are made in line-by-line calculations. The most important of these are the line shape, line cut-off distance, and formulation of continuum absorption. These can be tuned so that the model-generated spectrum fits observational spectra (Halevy et al., 2009a). Melsheimer et al. (2005) performed an inter-comparison of several line-by-line models for atmospheric sounding in the millimetre and sub-millimeter range. They found that the choice of line-shape, continuum absorption and spectroscopic database can cause deviations of about 10%.

### 2.4.2 Band Models

Band models are significantly faster than line-by-line calculations. They average the absorption coefficient over small enough spectral bands so that the blackbody emission is approximately constant with respect to wavenumber but still contain a large number of absorption lines. Several assumptions are used to calculate the average absorption over the band which can introduce significant error. Significant disadvantages of the band model are that it is difficult to incorporate scattering or apply to non-homogeneous atmospheres.

### 2.4.3 Correlated $\kappa$

The correlated  $\kappa$  method has become popular today because of the ease of incorporating scattering into calculations and its computational efficiency. Correlated  $\kappa$  has a gain in efficiency of approximately  $10^5$  in comparison to line-by-line methods (O'Brien and Dilley, 2000). It does, however, have both theoretical and experimental limitations which are discussed.

The idea behind correlated  $\kappa$  is that the absorption coefficients can be re-ordered over small wavenumber bands so that the absorption coefficients are monotonically increasing, resulting in smoothly varying function. For numerical applications it is convenient to write the absorption coefficients in terms of the cumulative wavenumber distribution ( $g$ ). An example is shown in figure 2.2. The absorption coefficients are a much smoother as a function of the cumulative probability than wavenumber, and therefore, much larger step sizes can be used for absorption coefficients as a function of  $g$ . To model vertically inhomogeneous atmospheres the effects of changes in temperature and pressure must be accounted for. To do this it is assumed that the  $\kappa$ -distribution remains monotonically increasing for changes in pressure and temperature. This requires the following conditions,

1. If two frequencies have the same absorption coefficients at the same reference pressure and temperature, then they have the same absorption coefficients at all other temperatures and pressures.
2. The monotonically increasing order of the absorption coefficients at the reference pressure and temperature must remain monotonically increasing for all temperatures and pressures.

In general, these conditions are not satisfied but deviations are generally small. Deviations from these conditions occur because of partial line overlap, the difference of line widths and strengths for absorption lines, and non-unique temperature dependence of line strength (Zhang and Shi, 2002).

#### 2.4.4 Mapping Transformations

Spectral mapping techniques use the same strategy as the correlated  $\kappa$  technique. However, spectral mapping techniques preserve the one-to-one correspondence between the mapped variable and wavenumber. This allows the mapping to be performed multiple times. The process happens as follows,

1. Over a spectral interval  $\nu$  to  $\nu + \Delta\nu$  and at pressure,  $p_0$ , and temperature,  $T_0$ , the absorption coefficients are ordered so that they are monotonically increasing.
2. For an atmospheric level with a different pressure and temperature,  $p_1$  and  $T_1$ , the mapping that resulted in a monotonically increase in absorption coefficients

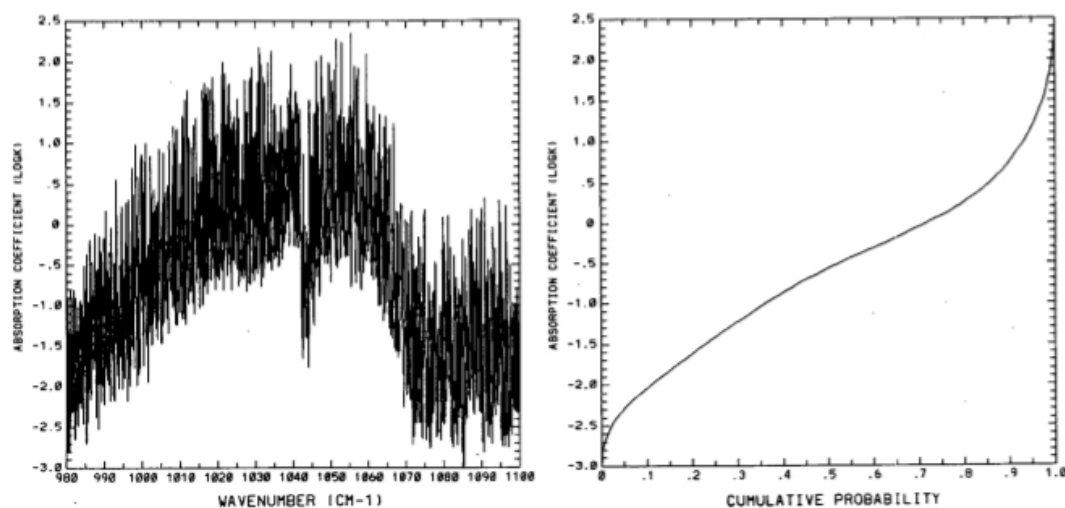


Figure 2.2: **Correlated- $\kappa$  Transformation.** Absorption coefficient  $\kappa$  in  $(\text{cm atm})^{-1}$  as a function of (left) wavenumber and (right) cumulative probability for the  $\text{O}_3$   $9.6\text{-}\mu\text{m}$  band for a pressure of 25 mb and a temperature of 220 K. Taken from Fu and Liou (1992)

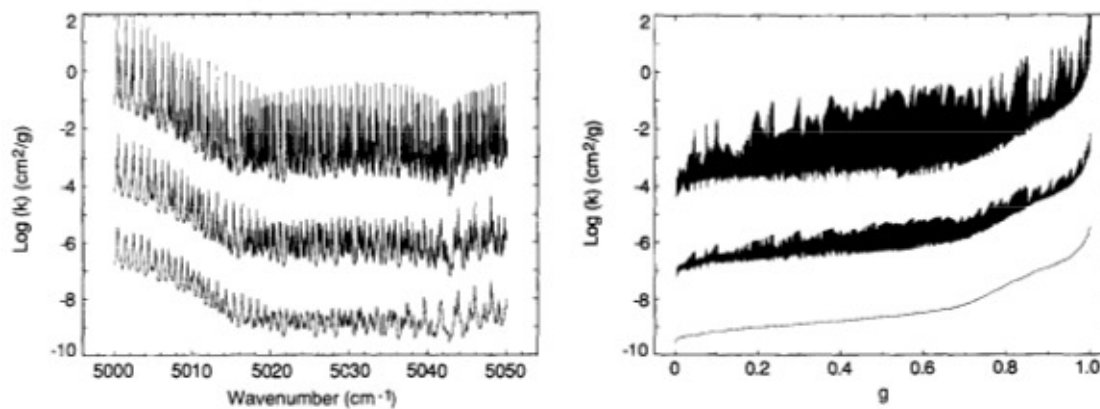


Figure 2.3: **Spectral Mapping for layer A.**  $\text{CO}_2$  absorption coefficient spectra as a function of wavenumber [left] and after sorting  $\kappa$  for layer A. Taken from West et al. (1990)

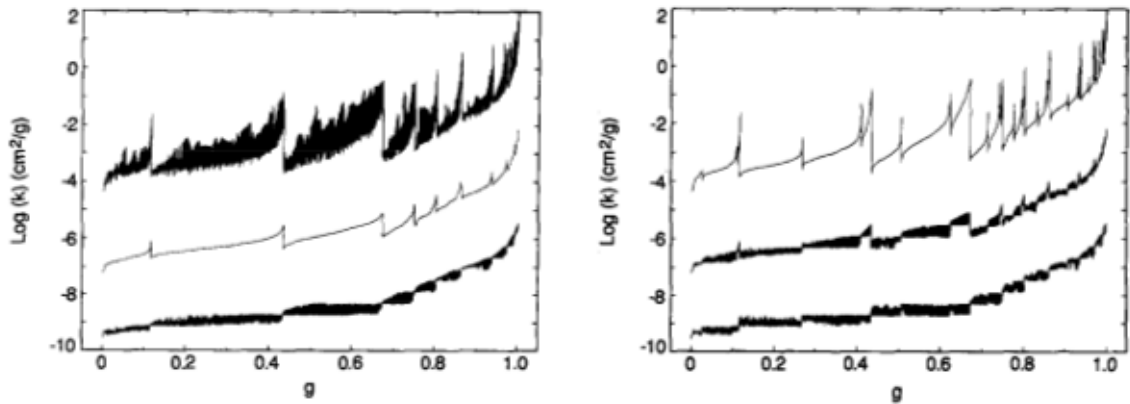


Figure 2.4: **Spectral Mapping for layers B and C.** CO<sub>2</sub> absorption coefficient spectra after sorting  $\kappa$  for layer B (left) and layer C (right) using Method 1 of West et al. (1990). Taken from West et al. (1990)

for  $p_0$  and  $T_0$  results in absorption coefficients that are not monotonically increasing. The frequency interval  $\nu$  to  $\nu + \Delta\nu$  is then split up into several smaller frequency intervals and the absorption coefficients are reordered over each new interval so that absorption coefficients are monotonically increasing.

As an example, consider three layers within an atmosphere (A, B and C) of different pressures and temperatures. The absorption coefficients over a wavenumber range  $5000\text{-}5050\text{ cm}^{-1}$  are shown in figure 2.3 for the layers A, B and C from top to bottom. The absorption coefficients are then mapped so that they are monotonically increasing for layer C (figure 2.3). However, the absorption coefficients are not monotonically increasing for layers A and B. The cumulative probability,  $g$ , can then be subdivided into smaller sections and layer B is rearranged so the the absorption coefficients are monotonically increasing as a function of  $g$  over each new interval (figure 2.4). This is performed again for A. This can be performed as many times as necessary until the error is below a chosen threshold.

### 2.4.5 Radiative Transfer models in the context of this work

As discussed above, band and correlated- $\kappa$  radiative transfer model use various assumptions which are, in general, not true. The accuracy of the non-homogeneous correlated  $\kappa$ -distribution method has been heavily tested by comparisons with line-by-line calculations. It is impossible to a priori specify the accuracy of correlated  $\kappa$  models, so errors must be found by comparisons with line-by-line calculations (West et al., 1990). It is found to generally give good results with errors of order magnitude 1% (Goody et al., 1989) over the concentration range for which they are parametrized. However, outside of this range the errors can become very large.

In the work that follows, we perform radiative forcing calculations for gases and ranges of gas concentrations which have not been performed before. It is therefore critical that we perform our calculations with a radiative transfer code that is known to be accurate. In this way our results are available as a standard for which radiative forcing calculations with faster radiative transfer codes can be compared. Furthermore, we perform calculations over quite extreme changes in concentration. At very high concentrations (e.g.,  $> 5,000$  ppmv of  $\text{CO}_2$ ) it has been found that errors in radiative transfer from simpler models can be very large (Goldblatt et al., 2009b).

For this reason, we use the Spectral Mapping for Atmospheric Radiative Transfer (SMART) code, written by David Crisp (Meadows and Crisp, 1996), for our radiative

transfer calculations. This code works at line-by-line resolution but uses a spectral mapping algorithm to treat different wavenumber regions with similar optical properties together, giving significant savings in computational cost. We evaluate the radiative transfer in the range  $50\text{--}100,000\text{ cm}^{-1}$  ( $0.1\text{--}200\text{ }\mu\text{m}$ ) as a combined solar and thermal calculation. The SMART model has been heavily tested in a wide variety of environments, from remote sensing of the Venusian atmosphere (Meadows and Crisp, 1996) to absorption of solar radiation by water vapour in clouds on Earth (Crisp, 1997). The SMART model has also been used in various radiative transfer code comparisons (Halthore et al., 2005; Halevy et al., 2009b).

# Chapter 3

## Modern Earth

### 3.1 Introduction

Radiative forcing is the change in the net flux of radiation at the tropopause due to a change in greenhouse gas concentration. Given that the tropospheric structure is determined largely by convection, it has been found that the change in surface temperature is directly proportional to the radiative forcing. Hence this becomes the simplest way of quantifying the effect in a perturbation in greenhouse gas inventory, and of comparing greenhouse gases. In this paper, we present new calculations of radiative forcing at very high concentrations of  $\text{CO}_2$ ,  $\text{CH}_4$ , and  $\text{N}_2\text{O}$ , relevant to extreme anthropogenic climate change, paleoclimate studies and models of the carbon cycle evolution.

Calculating a radiative forcing requires running a radiative transfer model for perturbed and unperturbed greenhouse gas concentrations. As these are rather specialist codes, it is very common to refer to empirical fits, or ‘simplified expressions’ of radiative forcing as given by the Intergovernmental Panel on Climate Change, first in IPCC (1990) and updated in IPCC (2001). Using the property that change in surface temperature is proportional to radiative forcing, radiative forcings are often used to force climate models which do not have vertically resolved atmospheres, ranging from simple box models to Earth system models of intermediate complexity, e.g., the UVic model (Weaver et al., 2001), the MICRO-lite model (Tachiiri et al., 2010), and the DCESS Earth System Model (Shaffer et al., 2008).

The existing commonly used simplified expressions (IPCC, 2001) were fitted for  $\text{CO}_2$  concentrations up to 1000 ppmv and  $\text{CH}_4$  and  $\text{N}_2\text{O}$  concentrations up to 5 ppmv

(Hansen et al., 1988). However, some current anthropogenic emission scenarios project higher gas concentrations. For example, representative concentration pathway (RCP) 8.5 projects a concentration of 1962 ppmv CO<sub>2</sub> for year 2250 (Meinshausen et al., 2011). For palaeoclimate, higher concentrations are required. The standard compilation (Royer, 2006) of geological CO<sub>2</sub> proxies for 450 Ma to present shows CO<sub>2</sub> of 1000 to 3000 ppmv to be common, and concentrations of up to 6000 ppmv to occur at times. Beerling et al. (2009) estimate CH<sub>4</sub> concentrations of 10-12 ppmv in Permo-Carboniferous. Modelling of CH<sub>4</sub> concentrations since 400 Ma suggests that 3 ppmv is common, with peak concentrations of 12 ppmv around the Permian-Carboniferous boundary (299 Ma). Destabilization of methane clathrates could give higher concentration still (Schmidt and Shindell, 2003). Given the uncertainties in paleo-concentration estimates, we examine larger concentration ranges to bound these estimates.

In this paper, we calculate radiative forcings for CO<sub>2</sub> up to 50,000 ppmv and CH<sub>4</sub> and N<sub>2</sub>O up to 100 ppmv at line-by-line spectral resolution, for both clear and cloudy skies. We examine the overlap between forcings and propose new simplified expressions for the forcings over the full range of concentrations we consider. We also calculate the meridional variation in forcing, which will be applicable to climate models forced with radiative forcings.

## 3.2 Methods

### 3.2.1 Radiative Transfer Calculation

We use the Spectral Mapping for Atmospheric Radiative Transfer (SMART) code, written by David Crisp (Meadows and Crisp, 1996), for our radiative transfer calculations. This code works at line-by-line resolution, but uses a spectral mapping algorithm to treat different wavenumber regions with similar optical properties together, giving significant savings in computational cost. We evaluate the radiative transfer in the range 50-100,000 cm<sup>-1</sup> (0.1-200 μm) as a combined solar and thermal calculation.

Line data for all radiatively active gases are taken from the HITRAN 2012 database. Cross sections are taken from the NASA Astrobiology Institute Virtual Planetary Laboratory Spectral Database <http://depts.washington.edu/naivpl/content/molecular-database>.

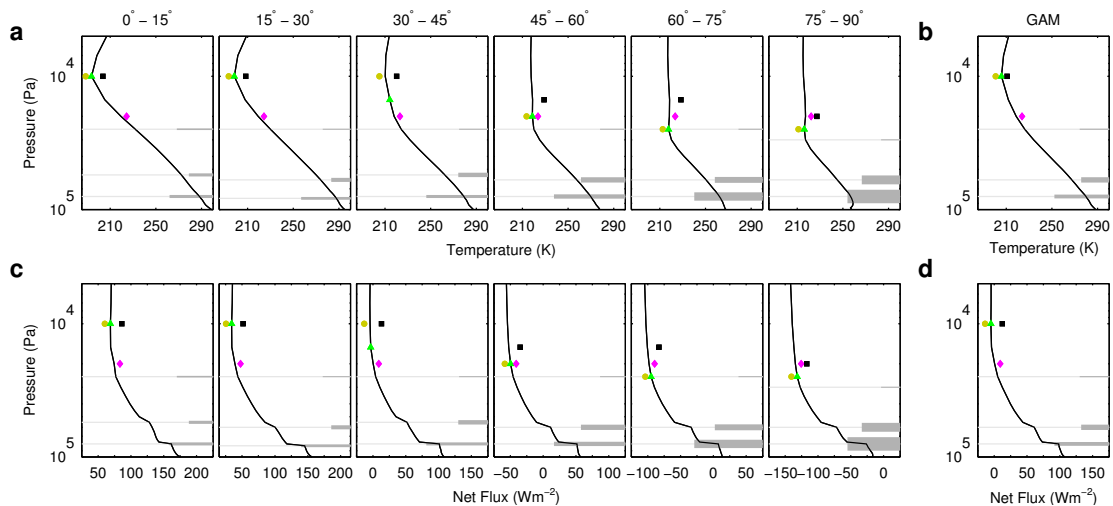


Figure 3.1: **Atmospheric profiles.** Temperature structure of the atmosphere for (a) six profile set and (b) GAM profile and net flux profile at pre-industrial gas concentrations for (c) six profile set and (d) GAM profile. For all panels, the grey lines represent cloud height; line thickness indicates the cloud optical thickness and the width of the thick line corresponds to cloud fraction. Markers represent tropopause height for each tropopause: temperature minimum (yellow circle), lapse rate (green triangle), 200 hPa (magenta diamond) and radiative (black square).

### 3.2.2 Atmosphere Profiles

Appropriate averaging of the atmospheric structure is required to calculate the radiative forcing. It is important to note that a radiative forcing calculated on averaged profiles is not the same as the average radiative forcing. Temporal and zonal averaging leads to small errors (1%) in calculated radiative forcing, whereas meridional averaging gives larger errors (3% for  $\text{CO}_2$ , higher for poorly mixed gases) (Myhre and Stordal, 1997; Freckleton et al., 1998).

We calculate mean profiles from the Modern Era Retrospective-analysis for Research and Applications (MERRA) reanalysis data products (Rienecker et al., 2011). The climatology is averaged zonally and temporally over the period 1979 to 2011. We used two meridional profile sets. **(1)** A single Global Annual Mean (GAM) **(2)**  $15^\circ$  meridional bins, to give six profiles, the area-weighted sum of which gives a global forcing (Figure 3.1). Tables of profiles are provided in appendix A.3. Our solar source is spectrally resolved. We use solar zenith angles of  $60^\circ$  for the GAM profile and  $51.0^\circ$ ,  $54.1^\circ$ ,  $60.0^\circ$ ,  $67.0^\circ$ ,  $75.5^\circ$ , and  $83.7^\circ$  for the profiles in the six profile set. These zenith angles correspond to the average intensity of insolation over the course of a day.

### 3.2.3 Cloud Climatology

Clouds absorb in the same spectral regions as the greenhouse gases we consider, so the presence of clouds will reduce the radiative forcing relative to clear sky conditions. Thus clouds must be resolved. We take our cloud climatology as cloud fractions and optical depths from International Satellite Cloud Climatology Project (ISCCP) D2 data set, averaging from January 1990 to December 1992. This period is used by Rossow et al. (2005) and was chosen so that we could compare cloud fractions. We assume random overlap and average by area to estimate cloud fractions (Figure 3.1). Tables of cloud properties are available are provided in appendix A.3. Scattering and absorption refraction indexes are taken from Hale and Querry (1973) for water droplets and from <http://www.ssec.wisc.edu/baum/index.html> for ice crystals. Water droplets are taken to to be monodisperse with a size of 11  $\mu\text{m}$  following Goldblatt and Zahnle (2011a) and ice crystal diameters were taken to be 70  $\mu\text{m}$ .

### 3.2.4 Radiative Forcing Definition

Two definitions of radiative forcing are relevant to this study. The calculations performed in this study use the instantaneous radiative forcing,  $F_i$ , which is, the change in net flux at the tropopause with no feedbacks. The simplified expressions given by IPCC (2001) are for the adjusted forcing,  $F_a$ , which is the change in net flux at the tropopause after allowing stratospheric temperatures to adjust to equilibrium. The reason for allowing stratospheric adjustment is that the stratosphere adjusts to a radiative perturbation rapidly (months) in comparison to the troposphere (decades) which is tightly coupled to the ocean. Therefore,  $F_a$  should be expected to be a better measure of the expected climate response for long lasting forcings than  $F_i$ .

However, calculating  $F_a$  is much more computationally expensive then calculating  $F_i$ , requiring iterative calculation of stratospheric adjustment. To be confident in the accuracy of the calculated forcings, we use a model which is very computationally expensive. The trade-off is that the computational cost of calculating  $F_a$  would be prohibitive. Calculating  $F_i$  allows us to supply reference flux profiles, against which faster models may be tested for future work calculating  $F_a$ .

The difference in  $F_i$  and  $F_a$  from Hansen et al. (2005) can be used to bound the expected uncertainty from only calculating  $F_i$  here. The difference is largest for  $\text{CO}_2$ , which cools the stratosphere.  $F_i$  is larger than  $F_a$  by 10% for a small increase in  $\text{CO}_2$  from reference conditions (for which the magnitude of the radiative forcing is small),

7.5% larger at  $8 \times \text{CO}_2$  (2328 ppmv) and the difference is expected to decrease further for the higher  $\text{CO}_2$  which we focus on. For  $\text{CH}_4$  and  $\text{N}_2\text{O}$ , the maximum differences are 4.5% and 2.5% respectively.

### 3.2.5 Tropopause Definition

The tropopause is the boundary between the troposphere and the stratosphere. It is commonly seen as the base of the stratospheric temperature inversion. However from a radiative perspective, relevant here, the inversion is somewhat a co-occurrence (due to the particularly high strength of UV absorption by ozone). Our primary concern is the transition from the tropopause temperature structure dominated by large scale air motions and the stratosphere which is largely in radiative equilibrium. Defining the tropopause as the lowest level which is in radiative equilibrium, surface temperature change being proportional to radiative forcing follows directly.

However, the tropopause height varies spatially (higher in tropics) and temporally, so averaging introduces inherent ambiguity in the tropopause height. When a prescribed tropopause definition is used in  $F_a$  calculations, different definitions lead to 10% variation in  $F_a$  calculations (Myhre and Stordal, 1997), comparable to the difference between  $F_a$  and  $F_i$ .

An advantage of calculating  $F_i$  from fixed profiles is we can easily compare different tropopause definitions. We compare: **(1)** The level at which the lapse rate changes sign (temperature minimum tropopause). **(2)** The lowest level at which the temperature lapse rate between this and all higher levels within 2 km falls below  $2 \text{ K km}^{-1}$  (lapse rate tropopause) (WMO, 1985). **(3)** The 200 hPa pressure level (200 hPa pseudo-tropopause) (Collins et al., 2006). **(4)** The lowest level at which the difference in net flux between this level and the next higher level is below an arbitrary threshold, taken as  $3 \text{ Wm}^{-2}$  here (radiative tropopause) (Figure 3.1).

## 3.3 Results

### 3.3.1 Calculated Forcings

We calculated radiative forcings for  $\text{CO}_2$ ,  $\text{CH}_4$  and  $\text{N}_2\text{O}$  on the GAM profile and the six profile set (Figure 3.2). We take the radiative definition of the tropopause on the six profile set to be the most physically realistic, and use this as reference

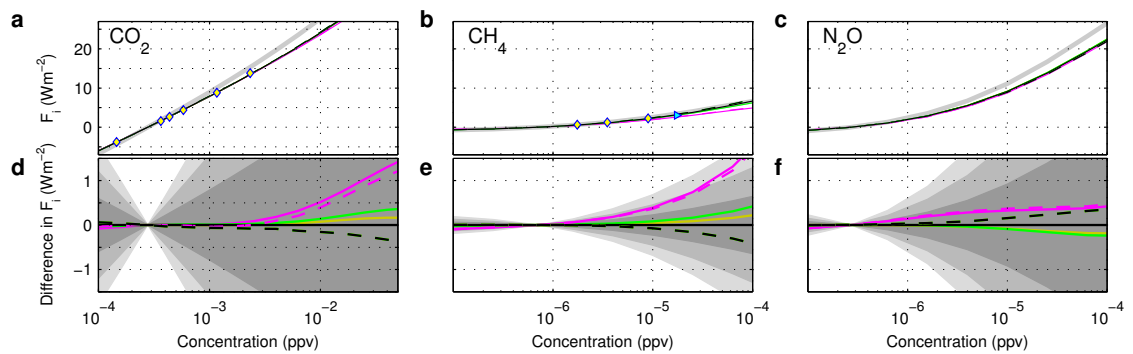


Figure 3.2: **Radiative forcings** (a-c) Calculated radiative forcing for each gas with various tropopause definitions. Coloured lines are all-sky forcings: yellow for temperature minimum, green for lapse rate, magenta for 200 hPa and black for radiative, solid lines from six profile set and dashed from GAM. Grey line is clear-sky radiative forcing for six profile radiative tropopause. The yellow diamonds represent the all sky  $F_a$  from Hansen et al. (2005) and cyan triangle represent clear sky  $F_i$  from Kurten et al. (2011), included for comparison. (d-f) Difference in radiative forcing between each tropopause definition and the radiative tropopause definition. Colours as top row (note that lapse rate, temperature and radiative definitions are coincident for the GAM profile). Shading represents the percentage difference in radiative forcings, from dark grey to white: of 0-10%, 10-20%, 20-30%, and greater than 30%.

for comparison. For all gases, the 200 hPa pseudo-tropopause gives the largest error relative to the reference; we do not recommend this for radiative forcing calculations. In all other cases, the difference in  $F_i$  due to different tropopause definitions is less than  $1 \text{ Wm}^{-2}$ . For the six profile set, the largest percentage differences are 0.9%, 6.8% and 1.7% for  $\text{CO}_2$ ,  $\text{CH}_4$  and  $\text{N}_2\text{O}$  respectively. For the GAM, all tropopause definitions are coincident, and the error (maximum 1.0%, 6.9% and 1.2% for  $\text{CO}_2$ ,  $\text{CH}_4$  and  $\text{N}_2\text{O}$  respectively) arises from meridional averaging. The largest discrepancies are for  $\text{CH}_4$  which is a good solar absorber at higher concentrations. Solar radiation is absorbed around the tropopause so small differences in the vertical position of the tropopause strongly affect the net flux.

### 3.3.2 Overlap

When multiple gases absorb radiation at the same frequencies, the total absorption (and hence radiative forcing) is less than the sum of the absorptions that each gas would contribute in isolation. This difference is known as overlap. It occurs because the absorption is distributed between the gases, so in effect there is less radiation available for each gas to absorb.

Figure 3.3 shows the absorption cross-sections of the main greenhouse gases and highlights overlapping absorption.  $\text{N}_2\text{O}$ – $\text{CO}_2$  overlap occurs around  $600 \text{ cm}^{-1}$ . Over the  $\text{N}_2\text{O}$  concentrations expected due to anthropogenic emissions this absorption feature is not optically thick, so the reduction in  $F_i$  is expected to be small. However, at higher  $\text{N}_2\text{O}$  concentrations the overlap becomes increasingly important as this absorption feature becomes optically thick.  $\text{N}_2\text{O}$  –  $\text{CH}_4$  overlap occurs between  $1150\text{--}1350 \text{ cm}^{-1}$ , the spectral range at which both  $\text{N}_2\text{O}$  and  $\text{CH}_4$  absorb best, so there will be a significant overlap effect. There is minimal overlap between  $\text{CO}_2$  and  $\text{CH}_4$ .

Reduction in radiative forcing due to overlap is shown in Figure 3.4. For all gases, where concentration is less than RCP8.5 year 2250 concentrations the effect of overlap is small ( $< 0.1 \text{ Wm}^{-2}$ ). However,  $\text{N}_2\text{O}$ – $\text{CH}_4$  and  $\text{N}_2\text{O}$ – $\text{CO}_2$  overlap become important (several  $\text{Wm}^{-2}$ ) at higher concentrations and should be accounted for in any applications.

### 3.3.3 IPCC fits

The family of simplified fits from IPCC (2001) are summarised in Table 3.1, and compared to our new  $F_i$  calculations in Figure 3.5. There are various legitimate

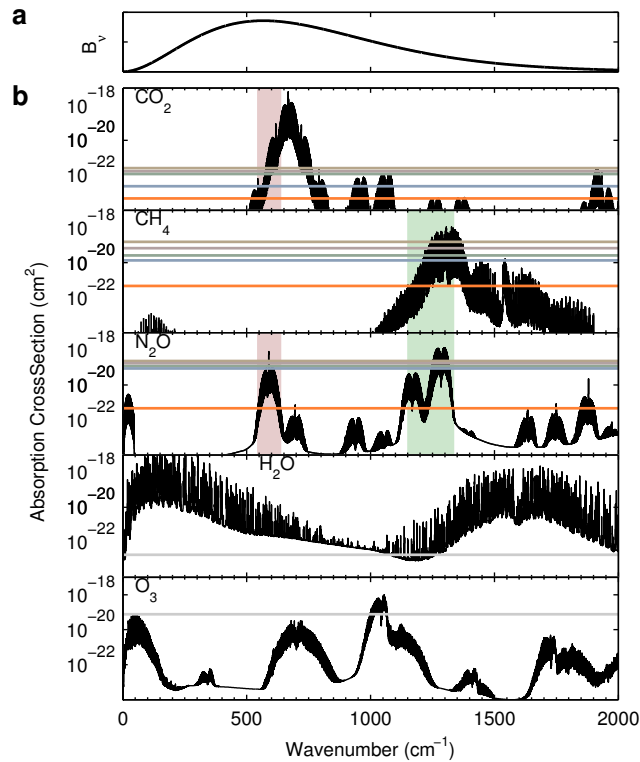


Figure 3.3: **Absorption cross-sections** (a) Spectral radiance ( $B_\nu$ ) emitted by a blackbody of 289 K, for reference. (b) Representative absorption cross sections for each greenhouse gas (calculated for 500 hPa and 260 K). Horizontal lines are the absorption cross section at which the optical depth due to that gas would be unity over the entire atmosphere, given some concentration or column abundance of the gas. Reference gas concentrations: glacial minimum (pastel yellow), pre-industrial (pastel red), present-day (pastel green) and RCP 8.5 year 2250 (pastel blue). Orange is the maximum concentration we consider for each greenhouse gas. For water and ozone, grey lines correspond to column abundance for GAM profile. Shaded areas highlight gas overlap; pink for  $\text{CO}_2\text{-N}_2\text{O}$ , green for  $\text{CH}_4\text{-N}_2\text{O}$ .

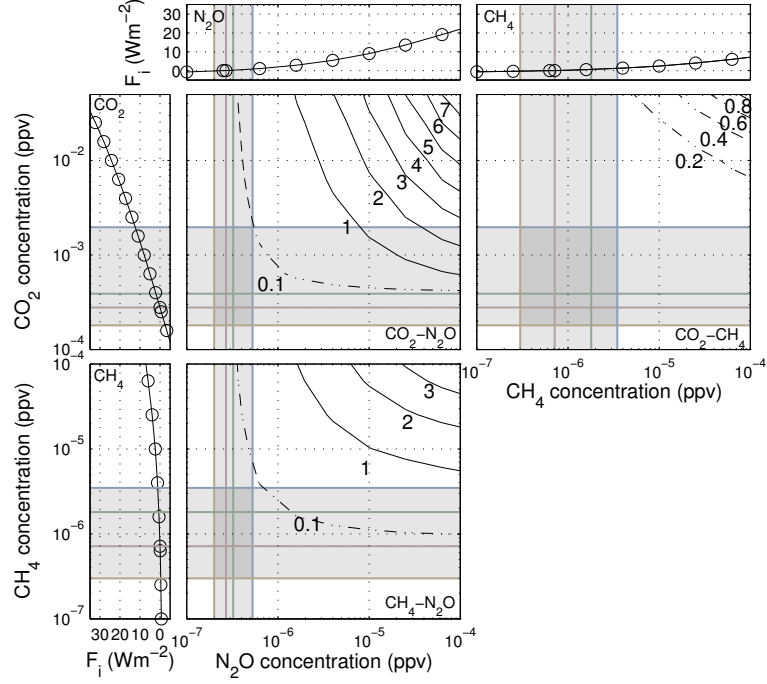


Figure 3.4: **Reduction in  $F_i$  due to overlap.** Peripheral line plots are radiative forcing for each gas, for reference. Contour plots show the reductions in radiative forcing due to overlapping absorption ( $\text{Wm}^{-2}$ ) for  $\text{CH}_4\text{-N}_2\text{O}$  (bottom),  $\text{CO}_2\text{-N}_2\text{O}$  (top left), and  $\text{CO}_2\text{-CH}_4$  (top right). Contours are solid for reductions in radiative forcing greater than  $1 \text{ Wm}^{-2}$  and dash-dot for less than  $1 \text{ Wm}^{-2}$ . Vertical and horizontal pastel lines are reference concentrations, colours as in figure 3.3.

Table 3.1: **IPCC Radiative Forcing Fits.** The simplified expressions of radiative forcing given in IPCC (2001).  $C$  is  $\text{CO}_2$  in ppmv,  $M$  is  $\text{CH}_4$  in ppbv and  $N$  is  $\text{N}_2\text{O}$  in ppbv.

Gas	Expression	Constants	Based On
$\text{CO}_2$	$F_a = \alpha \ln(C/C_0)$	$\alpha = 5.35$	IPCC (1990)
	$F_a = \alpha \ln(C/C_0) + \beta \left( \sqrt{C} - \sqrt{C_0} \right)$	$\alpha = 4.841, \beta = 0.0906$	Shi (1992)
	$F_a = \alpha (g(C) - g(C_0))$	$\alpha = 3.35$	WMO (1999)
where $g(C) = \ln(1 + 1.2C + 0.005C^2 + 1.4 \times 10^{-6}C^3)$			
$\text{CH}_4$	$F_a = \alpha \left( \sqrt{M} - \sqrt{M_0} \right) - (f(M, N_0) - f(M_0, N_0))$	$\alpha = 0.036$	IPCC (1990)
$\text{N}_2\text{O}$	$F_a = \alpha \left( \sqrt{N} - \sqrt{N_0} \right) - (f(M_0, N) - f(M_0, N_0))$	$\alpha = 0.12$	IPCC (1990)
$f(M, N) = 0.47 \ln [1 + 2.01 \times 10^{-5}(MN)^{0.75} + 5.31 \times 10^{-15}M(MN)^{1.52}]$			

Table 3.2: **New Radiative Forcing Fits.** Simplified expressions fit to calculated radiative forcings. C, M, and N represent the concentrations of CO<sub>2</sub>, CH<sub>4</sub>, and N<sub>2</sub>O in ppv.  $C_0 = 278 \times 10^{-6}$ ,  $M_0 = 715 \times 10^{-9}$ ,  $N_0 = 270 \times 10^{-9}$ , and  $N_1 = M_1 = 2.5 \times 10^{-6}$ . All radiative forcings are given from pre-industrial concentrations. N<sub>2</sub>O–CO<sub>2</sub> and N<sub>2</sub>O–CH<sub>4</sub> overlap are the reduction in radiative forcing due to overlapping absorption.

Gas	Simplified Expression	Concentration (ppmv)
CO <sub>2</sub>	$F_i = 5.32\ln(C/C_0) + 0.39\ln(C/C_0)^2$	200-10,000
CH <sub>4</sub>	$F_i = 1173 \left( \sqrt{M} - \sqrt{M_0} \right) - 71636 \left( \sqrt{M} - \sqrt{M_0} \right)^2$	0.1 - 2.5
	$F_i = 0.824 + \frac{4}{5}\ln(M/M_1) + \frac{1}{5}\ln(M/M_1)^2$	2.5-100
N <sub>2</sub> O	$F_i = 3899(\sqrt{N} - \sqrt{N_0}) + 38256(\sqrt{N} - \sqrt{N_0})^2$	0.1-2.5
	$F_i = 4.182 + 3\ln(N/N_1) + 0.5469\ln(N/N_1)^2$	2.5-100
N <sub>2</sub> O–CO <sub>2</sub> overlap	$\Delta F_i = -16.16 \exp(-0.036(\ln(C - C_0) - 0.0024)^2 - 0.05(\ln(N - N_0) + 6.5)^2)$	
N <sub>2</sub> O–CH <sub>4</sub> overlap	$\Delta F_i = -24 \exp(-0.02(\ln(M - M_0) - 0.01)^2 - 0.044(\ln(N - N_0) + 7.73)^2)$	

reasons for there to be a discrepancy between calculated forcings, as discussed above. Conservatively, we take forcings within 10% to be in agreement.

For CO<sub>2</sub>, there are three simplified expressions in IPCC (2001). The fit based on WMO (1999) is in very close agreement with our new calculations. The fit based on Shi (1992) is in less close agreement, but still within 10%. However, the fit based on IPCC (1990) is in poor agreement with our calculated  $F_i$  above 1000 ppmv, underestimating the radiative forcing, so we do not recommend this for high CO<sub>2</sub> concentrations. We note, however, that this is the most commonly used fit.

For CH<sub>4</sub>, the shape of the curve from the IPCC fit is somewhat different from our calculated  $F_i$ , though the absolute differences (in Wm<sup>-2</sup>) are small as CH<sub>4</sub> is a weak greenhouse gas. Divergence becomes large at 20 ppmv, with the radiative forcing overestimated by the IPCC fit. For N<sub>2</sub>O, the IPCC fit is in good agreement with our calculated  $F_i$  up to 10 ppmv, above which it strongly overestimates the radiative forcing. Thus use of the IPCC fits for CH<sub>4</sub> and N<sub>2</sub>O for high greenhouse gas concentrations are not recommended.

### 3.3.4 New Fits

We propose new simplified expressions for radiative forcings for individual gases (Table 3.2). Theoretically, the relationship between radiative forcing and concentration

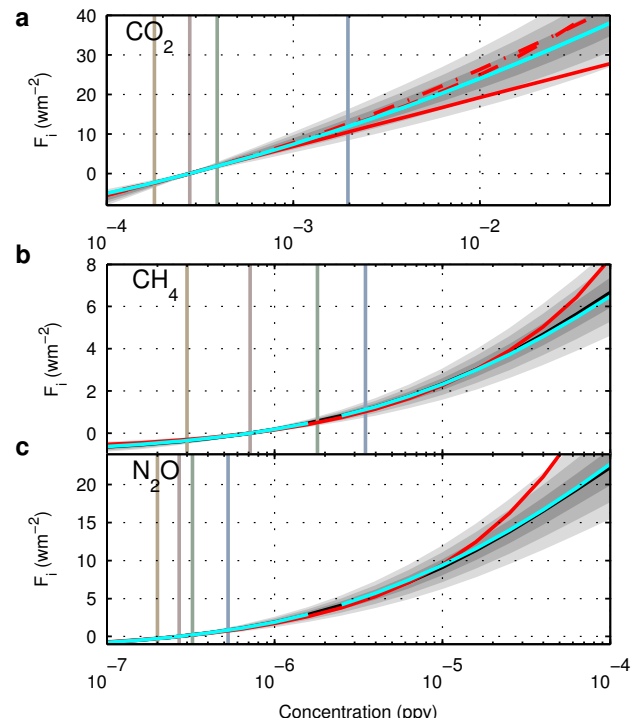


Figure 3.5: **Simplified expressions for radiative forcings.** Fits to radiative forcing for (a)  $\text{CO}_2$ , (b)  $\text{CH}_4$  and (c)  $\text{N}_2\text{O}$ . For all panels, black line is our calculated radiative forcing for six profile radiative tropopause, cyan line is our new fit and red lines are IPCC (2001) simplified expressions (dashed based on IPCC (1990)), dash-dot based on Shi (1992) and solid based on WMO (1999) (solid). Vertical lines are reference concentrations, in colour, are as figure 3.3. Shaded regions correspond to amount of error, as in figure 3.4.

should be linear at low concentrations, square root at intermediate concentrations and logarithmic at high concentrations. These approximate relationships come from the shape of absorption lines. When the entire line is optically thin, increasing the greenhouse gas concentration causes a linear increase in the radiative forcing. As the concentration increases, the line centre becomes saturated and most additional absorption happens in the wings, the shape of which gives a square root dependence on concentration. As the lines become saturated further out, the absorption becomes logarithmic with concentration. Of course, many lines contribute to absorption, not just one, but as dominant absorption is generally in one of the three categories, these approximations work reasonably well over large ranges of concentration. For  $\text{CO}_2$ , the concentration range of interest is all within the logarithmic regime, so a single fit is given. For  $\text{CH}_4$  and  $\text{N}_2\text{O}$ , the range of interest of concentrations straddles the square root and logarithmic regimes, so separate fits are proposed for concentrations above and below 2.5 ppmv. Fit parameters were chosen to minimize least squares errors. The cutoff point between square root and logarithmic concentration was chosen to be both a round number and a number which minimized least square errors.

For gas concentrations beyond RCP8.5 year 2250 projections, accounting for overlap is necessary. In table 3.2, we supply new fits for the overlap, which should be subtracted from the sum of the individual gas forcings. The functional form for overlap was chosen empirically such that it minimized least squared errors. The expressions for overlap should only be trusted in the range for which the simplified expressions are given.

### 3.3.5 Meridional Variation in $F_i$

The radiative forcings described so far are for global annual mean conditions, but at high greenhouse gas concentrations the forcing varies by several  $\text{Wm}^{-2}$  between the tropics and the poles (Figure 3.6). These meridional variations in the radiative forcing are primarily caused by variations in surface temperature and atmospheric water vapour concentrations, though differences in cloud climatology, tropopause height and insolation also contribute.

The simplified expressions from IPCC (2001), which are for global annual mean conditions, are commonly used to force spatially resolved models (e.g. Weaver et al. (2001)) at each grid cell, failing to account for these meridional variations. Hansen et al. (1997) applied a ‘ghost’ forcing of  $8 \text{Wm}^{-2}$  to the surface either poleward or

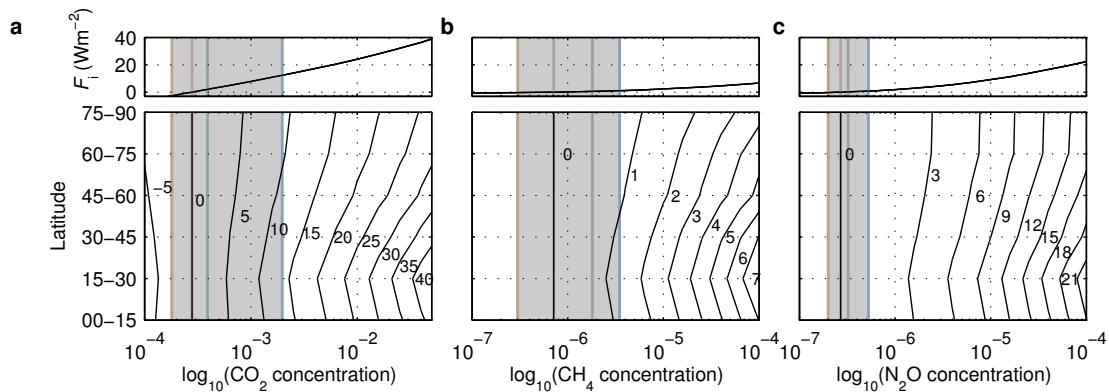


Figure 3.6: **Calculated  $F_i$  as a function of concentration and latitude.** Mean radiative forcing for (a)  $\text{CO}_2$ , (b)  $\text{CH}_4$  and (c)  $\text{N}_2\text{O}$  and latitude-dependent forcing for (d)  $\text{CO}_2$ , (e)  $\text{CH}_4$  and (f)  $\text{N}_2\text{O}$ . Vertical lines are reference concentrations, colours as figure 3.2.

equatorward of  $30^\circ$ , resulting in temperature differences of  $4.39^\circ\text{C}$  and  $2.37^\circ\text{C}$  respectively. Clearly, the climate response has a substantial dependence on the meridional distribution of the forcing.

It is not practical to develop simplified expressions for meridionally resolved forcings. As an alternative, we supply a table of these in appendix A.3, and recommend these be used with appropriate interpolation to force spatially resolved models.

### 3.4 Conclusions

We have performed new radiative forcing calculations for high concentrations of  $\text{CO}_2$ ,  $\text{CH}_4$  and  $\text{N}_2\text{O}$  appropriate for extreme anthropogenic global warming and paleoclimate studies. We provide simplified fits to these radiative forcings which are recommended in place of those from IPCC (2001) for high greenhouse gas concentrations. The reduction in radiative forcings due to overlap between these gases is less than  $0.1 \text{ Wm}^{-2}$  for concentrations up to RCP8.5 year 2250 values. For larger concentrations,  $\text{N}_2\text{O}-\text{CH}_4$  and  $\text{N}_2\text{O}-\text{CO}_2$  overlap can reduce the radiative forcing by several  $\text{Wm}^{-2}$ . We also provide simplified fits to account for this overlap. One should also note that additional products of atmospheric chemistry have radiative effects (IPCC, 2013), but these are not considered here.

The difference in radiative forcing between the tropics and the poles is considerable, and increases with the magnitude of radiative forcing (e.g., the meridional variation in forcing increases monotonically from 37% of the GAM forcing at 100 ppmv to 47% at 50,000 ppmv of  $\text{CO}_2$ ). Tables of these forcings are provided for use forcing climate models.

For deep paleoclimate, high radiative forcings may be necessary to balance reduced insolation and give a similar climate to today. In other cases though, strong radiative forcing will give climates substantially different from today (both “hothouse” and “icehouse” climates existed). Under such large climate changes, substantial non-smooth climate feedbacks are expected and the proportionality between radiative forcing and mean surface temperature will weaken. Such climates are an active area of research with general circulation models (e.g. Abbot et al., 2013; Russell et al., 2013). Nonetheless, radiative forcings and a climate sensitivity parameter of  $\approx 0.5 \text{ K}/(\text{Wm}^{-2})$  (IPCC, 2001) provide a good first-approximation estimate of climate change and are the best way of comparing the relative efficacy of different greenhouse gases.

# Chapter 4

## Early Earth

### 4.1 Introduction

The standard stellar model predicts that the luminosity of a star increases over its main-sequence lifetime (Gough, 1981). Therefore, the sun is 30% brighter now than it was when the solar system formed. Despite a dimmer sun during the Archean (3.8–2.5 Gyr BP) geologic evidence suggests surface temperatures similar to today (Donn et al., 1965); this apparent paradox is known as the faint young sun problem (FYSP). To reconcile this, Earth must have had a lower albedo and/or a stronger greenhouse effect in the past. In this work we focus on a stronger greenhouse effect, which is thought to be the primary mechanism for maintaining warm temperatures (Goldblatt and Zahnle, 2011a; Wolf and Toon, 2013). We focus on the late Archean with a solar constant of  $0.8 S_0$ , resulting in an reduction of  $\approx 50 \text{ Wm}^{-2}$  of insolation.

The most obvious resolution to the FYSP would be higher  $\text{CO}_2$  partial pressures. It is believed that the inorganic carbon cycle provides a strong feedback mechanism which regulates the Earth's temperature over geologic timescales (Walker et al., 1981). The rate of silicate weathering (a sink of atmospheric  $\text{CO}_2$ ) is a function of surface temperature which depends on the carbon dioxide partial pressure through the greenhouse effect. Therefore, reduced insolation requires higher atmospheric  $\text{CO}_2$  concentrations to regulate the surface temperature and balance the sources (volcanoes) and sinks of atmospheric  $\text{CO}_2$ . However, geological constraints have been proposed which limit the atmospheric level of  $\text{CO}_2$  to levels below those required to keep the early Earth warm (Sheldon, 2006; Driese et al., 2011). Sheldon (2006) used a model based on the mass balance of weathering paleosols and find  $\text{CO}_2$  partial pressures between

0.0028-0.026 bar at 2.2 Gyr ago. Driese et al. (2011) use the same method and find  $\text{CO}_2$  partial pressures between 0.003 and 0.02 bar at 2.69 Gyr ago. However, it has been suggested that errors in these analyses may be larger than the authors acknowledge (Kasting, 2013).

Many researchers have recognized that other greenhouse gases may have played an important role in the early Earth's energy budget. Most of the focus has been applied to  $\text{CH}_4$  as there are good reasons to expect higher concentrations during the Archean (Zahnle, 1986; Kiehl and Dickinson, 1987; Pavlov et al., 2000; Haqq-Misra et al., 2008; Wolf and Toon, 2013). The Archean atmosphere was nearly anoxic with very low levels of  $\text{O}_2$ , which would have increased the photochemical lifetime of methane from 10-12 years today to 1000-10,000 years (Kasting, 2005). The concentration of methane in the Archean is not well constrained but Kasting (2005) suggests that 1-10 ppmv could have been sustained from abiotic sources and up to 1000 ppmv could have been sustained by methanogens. Redox balance models suggest concentrations  $\approx 100$  ppmv (Goldblatt et al., 2006).

Other potential greenhouse gases which have been examined previously include  $\text{NH}_3$  (Sagan and Mullen, 1972; Kuhn and Atreya, 1979; Kasting, 1982; Sagan and Chyba, 1997), hydrocarbons (Haqq-Misra et al., 2008),  $\text{N}_2\text{O}$  (Buick, 2007; Roberson et al., 2011), and OCS (Ueno et al., 2009; Hattori et al., 2011).

Examining the Archean greenhouse involves calculating the radiative effects of greenhouse gases over concentration ranges never before examined. Typically, one time calculations are performed with no standard set of radiative forcings available for comparison. The absence of a standard set of forcings has led to errors going undetected. For example, the warming exerted by  $\text{CH}_4$  was significantly overestimated by Pavlov et al. (2000) due to an error in the numbering of spectral intervals (Haqq-Misra et al., 2008) which went undetected for several years.

In previous work, greenhouse gas warming has typically been quantified in terms of the equilibrium surface temperature achieved by running a one-dimensional Radiative-Convective Model (RCM). This metric is sensitive to how climate feedbacks are parametrized in the model and to imposed boundary conditions (e.g., background greenhouse gas concentrations). This makes comparisons between studies and greenhouse gases difficult. It is desirable to document the strengths and relative efficiencies of different greenhouse gases at warming the Archean climate. However, this is near impossible using the literature presently available.

In this study, we use radiative forcing ( $F_i$ ) to quantify changes in the energy budget

from changes in greenhouse gas concentrations for a wide variety of greenhouse gases. We define radiative forcing as the change in the net flux of radiation at the tropopause due to a change in greenhouse gas concentration with no climate feedbacks. The great utility of radiative forcing is that, to first order, it can be related through a linear relationship to global mean temperature change at the surface (Hansen et al., 2005). It therefore, provides a simple and informative metric for understanding perturbations to the energy budget. Furthermore, since radiative forcing is independent of climate response, we get general results which are not affected by uncertainties in the climate response. Radiative forcing has been used extensively to study anthropogenic climate change (IPCC, 2013).

Imposed model boundary conditions significantly affect the warming provided by a greenhouse gas. Boundary conditions that typically vary between studies include: atmospheric pressure, CO<sub>2</sub> concentrations, and CH<sub>4</sub> concentrations. The discrepancies in boundary conditions between studies develop from the poorly constrained climatology of the early Earth. In this work, we examine the sensitivity of radiative forcings to variable boundary conditions.

The atmospheric pressure of the Archean is poorly constrained but there are good theoretical arguments to think it was different from today. For one, the atmosphere is 21% O<sub>2</sub> by volume today, whereas there was very little oxygen in the Archean atmosphere. Furthermore, there are strong theoretical arguments that suggest that the atmospheric nitrogen inventory was different: large nitrogen inventories exist in the mantle and continents, which are not primordial and must have ultimately come from the atmosphere (Goldblatt et al., 2009a). Constraints on the pressure range have recently been proposed, from raindrop imprints (Som et al., 2012) – though this has been challenged (Kavanagh and Goldblatt, 2013), and from noble gas systematics (0.7-1.1 bar, Marty et al., 2013). Atmospheric pressure affects the energy budget in two ways. (1) Increasing pressure increases the moist adiabatic lapse rate, in general suppressing convection and heating the surface and low troposphere at the expense of the upper troposphere. Water concentrations aloft decrease. (2) As the pressure increases, collisions between molecules become more frequent. This results in a broadening of the absorption lines over a larger frequency range. This phenomena is called pressure broadening and generally causes more absorption (Goody and Yung, 1995).

Changes to the concentrations of CO<sub>2</sub> and CH<sub>4</sub> will affect the strength of other greenhouse gases. When multiple gases absorb radiation at the same frequencies, the

total absorption is less than the sum of the absorption that each gas contributes in isolation. This difference is known as overlap. It occurs because the absorption is distributed between the gases, so in effect there is less radiation available for each gas to absorb.

In this thesis, we present calculations of radiative forcings for  $\text{CO}_2$ ,  $\text{CH}_4$  and 18 other gases contained in the HIgh-resolution TRANsmision (HITRAN) molecular database for atmospheres with 0.5 bar, 1 bar, and 2 bar of  $\text{N}_2$ . We aim to provide a complete set of radiative forcing and overlap calculations which can be used as a standard for comparisons. We provide  $\text{CO}_2$  and  $\text{CH}_4$  radiative forcings over large ranges in concentration. We compare our results with calculations in the literature. For the other 18 HITRAN gases, the HITRAN absorption data are compared with measured cross-sections and discrepancies are documented. Radiative forcings are calculated over a concentrations range of 10 ppbv to 10 ppmv. The sensitivities of the radiative forcings to atmospheric pressure and overlapping absorption with other gases are examined, and our results are compared with results from the literature.

This paper is organized as follows. In section 2, we describe our general methods, evaluation of the spectral data and the atmospheric profile we use. In section 3, we examine the radiative forcings due to  $\text{CO}_2$  and  $\text{CH}_4$  and examine how our results compare with previous calculations. In section 4, we provide radiative forcings for 18 other gases from the HITRAN database and examine the sensitivity of these results to atmospheric parameters.

## 4.2 Methods

### 4.2.1 Overview

We calculate absorption cross-sections from HITRAN line parameters and compare our results with measured cross-sections. We develop a single-column atmospheric profile based on constraints of the Archean atmosphere. With this profile, we perform radiative forcing calculations for  $\text{CO}_2$ ,  $\text{CH}_4$  and 18 other HITRAN gases.

### 4.2.2 Spectra

Line parameters are taken from the HITRAN 2012 database (Rothman et al., 2013). We use the LBLABC code, written by David Crisp, to calculate cross-sections from

the line data. Line parameters have a significant advantage over measured absorption cross-sections, in that, absorption can be calculated explicitly as a function of temperature and pressure. The strength of absorption lines is a function of temperature and shape is a function of pressure. Neglecting these dependencies can result in significant errors in radiative transfer calculations.

There are, however, some limitations to using HITRAN data. Rothman et al. (2009) explains that the number of transitions included in the database is limited by: (1) a reasonable minimum cutoff in absorption intensity (based on the sensitivity of instruments that observe absorption over extreme terrestrial atmospheric path lengths), (2) lack of sufficient experimental data, or (3) lack of calculated transitions. The molecules for which data are included in the line-by-line portion of HITRAN are mostly composed of small numbers of atoms and have low molecular weights. Large polyatomic molecules have many normal modes of vibration and have fundamentals at very low wavenumbers (Rothman et al., 2009). This makes it difficult to experimentally isolate individual lines of large molecules, so that a complete set of line parameters for these molecules is impossible to obtain.

Computed cross-sections are compared to measured cross-sections from the Pacific Northwest National Laboratory (PNNL) database (Sharpe et al., 2004) for the strongest HITRAN gases (figure 4.1). Where differences exist, it is not straight forward to say which is in error (for example, potential problems with measurements include contamination of samples). Hence we simply note any discrepancy and do our best to note the consequences of these. The largest concentration of the trace gases examined in this work is 10 ppmv, at this concentration only absorption cross-section greater than  $\approx 5 \times 10^{-21} \text{ cm}^2$  absorb strongly over the depth of the atmosphere. The similarities and differences between the cross-sections for each gas are:

- $\text{CH}_3\text{OH}$ : The HITRAN line data covers the range of 975–1075  $\text{cm}^{-1}$ . In that range the HITRAN cross-sections are an order of magnitude larger than the PNNL cross-sections. Therefore, the PNNL data suggests the concentrations should be an order of magnitude larger to obtain the same forcings as the HITRAN data. PNNL cross-sections indicate that there is missing HITRAN line data over the range 1075–1575  $\text{cm}^{-1}$  with peaks of  $\approx 5 \times 10^{-20} \text{ cm}^2$ , which would be optically thick for concentrations  $\geq 10^{-6}$  ppv. There is also missing HITRAN data at 550–750  $\text{cm}^{-1}$  with peaks of  $\approx 5 \times 10^{-21} \text{ cm}^2$ , which would be optically thick for concentrations  $\geq 10^{-5}$  ppv.

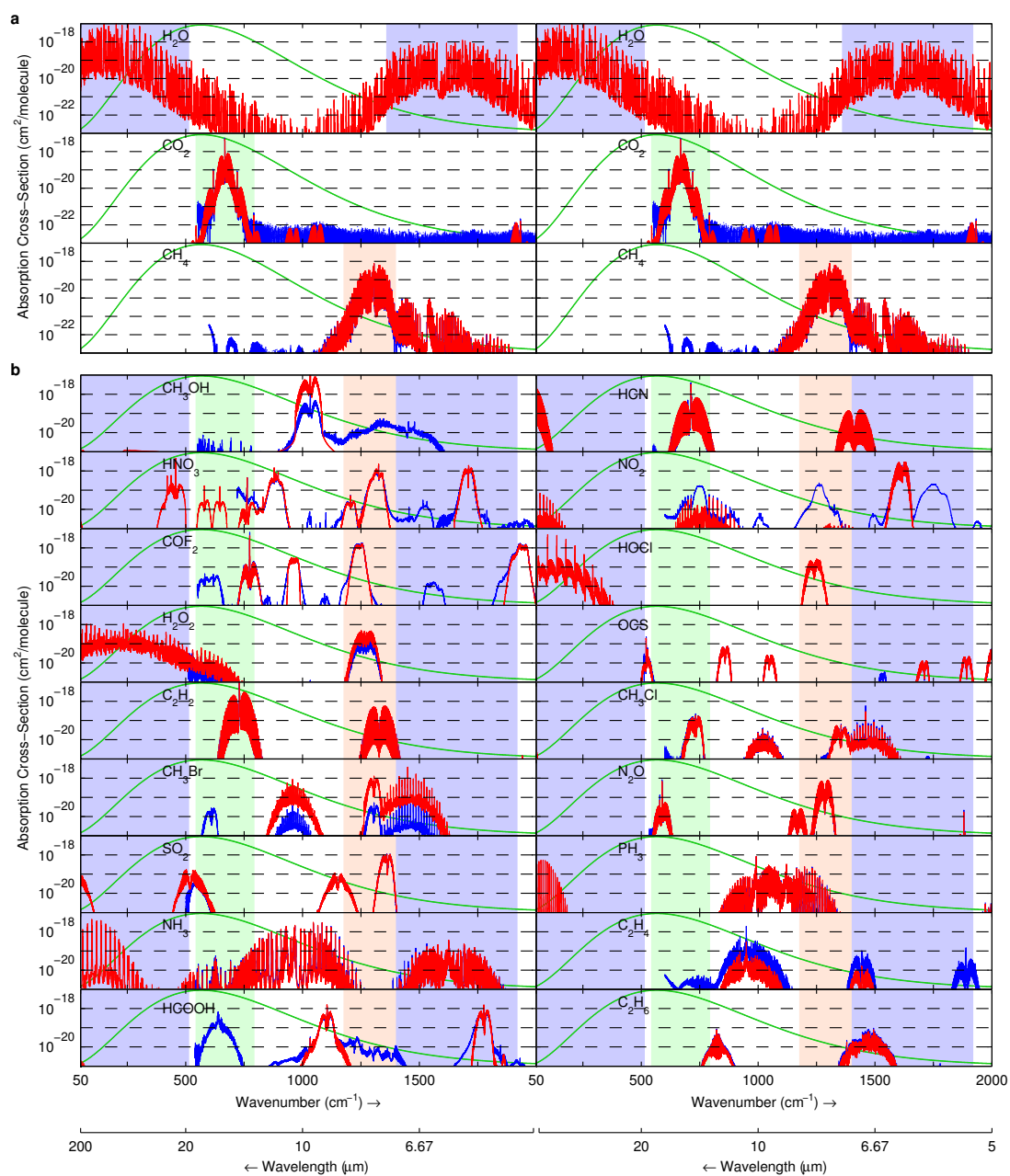


Figure 4.1: **Absorption cross-sections.** Absorption cross-sections of (a)  $\text{H}_2\text{O}$ ,  $\text{CO}_2$ , and  $\text{CH}_4$  and (b) potential early Earth trace gases. Cross-sections are calculated from HITRAN line data (red) and measured from the PNNL database (blue) at 1013 hPa and 278 K. The gases are ordered from strongest to weakest based on the analysis in section 4.3.3 (figure 4.9) in columns from top left to bottom right. Colored shaded areas show wavenumbers at which absorption is strongest for  $\text{H}_2\text{O}$  (blue),  $\text{CO}_2$  (green), and  $\text{CH}_4$  (red). Grey shaded areas show absorption cross-sections at which HITRAN and PNNL absorption disagree or PNNL data are not available. The green curve shows the shape of the blackbody emissions from a 289 K blackbody.

- $\text{HNO}_3$ : The HITRAN data covers the range of 550–950  $\text{cm}^{-1}$ , 1150–1400  $\text{cm}^{-1}$ , and 1650–1750  $\text{cm}^{-1}$ . Over this range, HITRAN and PNNL data agree well except between 725–825  $\text{cm}^{-1}$  where the PNNL cross-sections are larger (relevant for concentrations of  $\geq 5 \times 10^{-7}$  ppv). PNNL cross-sections indicate that there is significant missing HITRAN line data in the ranges 1000–1150  $\text{cm}^{-1}$ , 1400–1650  $\text{cm}^{-1}$ , and 1750–2000  $\text{cm}^{-1}$ , which would be optically thick for concentrations  $\geq 5 \times 10^{-6}$  ppv.
- $\text{COF}_2$ : The HITRAN cross-sections cover the range of 725–825  $\text{cm}^{-1}$ , 950–1000  $\text{cm}^{-1}$ , 1175–1300  $\text{cm}^{-1}$ , and 1850–2000  $\text{cm}^{-1}$ . The PNNL and HITRAN cross-sections agree over this range. HITRAN is missing bands around 650 and 1600  $\text{cm}^{-1}$  with peaks of  $\approx 10^{-20} \text{cm}^2$ , which would be optically thick for concentrations  $\geq 5 \times 10^{-6}$  ppv. Additionally, wings of 950–1000  $\text{cm}^{-1}$ , 1175–1300  $\text{cm}^{-1}$ , and 1850–2000  $\text{cm}^{-1}$  bands appear missing in HITRAN, relevant at similar concentrations.
- $\text{H}_2\text{O}_2$ : Above 500  $\text{cm}^{-1}$ , the HITRAN and PNNL cross-sections cover the same wavenumber range. Over this range, HITRAN cross-sections are about twice the value of the PNNL cross-sections. Therefore, the PNNL data suggests the concentrations should be about twice those of the HITRAN data to obtain the same forcings.
- $\text{C}_2\text{H}_2$ : The HITRAN and PNNL cross-sections agree well.
- $\text{CH}_3\text{Br}$ : HITRAN cross-sections are over an order of magnitude greater than the PNNL cross-sections. Therefore, the PNNL data suggests the concentrations should be  $\approx 13$  times those of the HITRAN data to obtain the same forcings. The PNNL cross-sections indicate missing HITRAN line data over the range of 575–650  $\text{cm}^{-1}$  with peaks of  $\approx 10^{-20} \text{cm}^2$ , which would be optically thick for concentrations  $\geq 5 \times 10^{-6}$  ppv.
- $\text{SO}_2$ : The HITRAN and PNNL cross-sections agree well except between 550–550  $\text{cm}^{-1}$  where HITRAN cross-sections are larger with peaks of  $\approx 5 \times 10^{-20} \text{cm}^2$ , which would be optically thick for concentrations  $\geq 10^{-7}$  ppv.
- $\text{NH}_3$ : The HITRAN and PNNL cross-sections agree well.
- $\text{HCOOH}$ : The HITRAN data between 1000–1200 and 1725–1875  $\text{cm}^{-1}$  agrees with the PNNL data. The PNNL cross-sections indicate missing line data

over the range 550–1000  $\text{cm}^{-1}$  with peaks of  $\approx 5 \times 10^{-19} \text{cm}^2$ , which would be optically thick for concentrations  $\geq 10^{-8}$  ppv., 1200–1725  $\text{cm}^{-1}$ , and 1875–2000  $\text{cm}^{-1}$  with peaks of  $\approx 5 \times 10^{-20} \text{cm}^2$ , which would be optically thick for concentrations  $\geq 10^{-7}$  ppv.

- HCN: The HITRAN and PNNL cross-sections agree well.
- NO<sub>2</sub>: The HITRAN and PNNL cross-sections agree well in the range 1550–1650  $\text{cm}^{-1}$ . The PNNL cross-sections are up to an order of magnitude larger than HITRAN for cross-sections in the range 650–850  $\text{cm}^{-1}$  and around 1400  $\text{cm}^{-1}$ . PNNL cross-sections indicate missing line data over the ranges 850–1100  $\text{cm}^{-1}$  and 1650–2000  $\text{cm}^{-1}$  with peaks of  $\approx 10^{-19} \text{cm}^2$ , which would be optically thick for concentrations  $\geq 5 \times 10^{-7}$  ppv.
- HOCl: There is no PNNL data for this gas.
- OCS: The HITRAN and PNNL cross-sections agree well.
- CH<sub>3</sub>Cl: The HITRAN and PNNL cross-sections agree well. PNNL cross-sections indicate missing line data around 600  $\text{cm}^{-1}$ .
- N<sub>2</sub>O: The HITRAN and PNNL cross-sections agree well.
- PH<sub>3</sub>: The HITRAN and PNNL cross-sections agree well.
- C<sub>2</sub>H<sub>4</sub>: The HITRAN data is about an order of magnitude less than PNNL. Therefore, the PNNL data suggests the concentrations should be an order of magnitude less to obtain the same forcings as the HITRAN data.
- C<sub>2</sub>H<sub>6</sub>: The HITRAN and PNNL cross-sections agree well.

The spectral data described above only covers the longwave spectrum. HITRAN line parameters are not available for the solar spectrum. We are unaware of any absorption data for these gases in the solar spectrum. If these gases are strong absorbers in the solar spectrum (e.g., O<sub>3</sub>) the radiative forcing calculations could be significantly affected. Very strong heating in the stratosphere would cause dramatic differences in the stratospheric structure which would significantly affect the radiative forcing.

### 4.2.3 Atmospheric Profile

We perform our calculations for a single-column atmosphere. Performing radiative forcing calculations for a single profile rather than multiple profiles representing the meridional variation in the Earth’s climatology introduces only small errors (Myhre and Stordal, 1997; Freckleton et al., 1998; Byrne and Goldblatt, 2014).

The tropospheric temperature structure is dictated largely by convection. We approximate the tropospheric temperature structure with the pseudo-adiabatic lapse rate. The lapse rate is dependent on both pressure and temperature. There is a large range of uncertainty in the surface temperatures of the Archean, we take the surface temperature to be the Global and Annual Mean (GAM) temperature on the modern Earth (289 K). We chose this temperature for two reasons. (1) It makes comparisons with the modern Earth straight forward. (2) It is likely a lower limit for the GAM surface temperature in the Archean. It is thought that temperatures were at-least as warm as present due to the modern glacial climate, given that there is a near-complete absence of evidence of glaciation throughout the Archean (Young, 1991).

In the troposphere, radiative equilibrium would result in a lapse rate that is super-adiabatic (greater than the dry-adiabatic lapse rate). Studies using radiative-convective models have found that within region where the radiative equilibrium lapse rate is super-adiabatic convective adjustment adjusts the temperature gradient such that the lapse rate is almost adiabatic (Ramanathan and Coakley, 1978). In particular, the moist adiabatic lapse rate has been found to closely reproduce the observed mid-latitude atmospheric temperature structure and results from radiative convective models. Thus, approximating the tropospheric temperature profile using the moist adiabatic lapse results in good agreement with radiative convective models.

We calculate three atmospheric profiles for  $N_2$  inventories of 0.5 bar, 1 bar, and 2 bar. Atmospheric pressure varies with the addition of  $CO_2$  and  $CH_4$ . We use the GAM relative humidity from Modern Era Retrospective-analysis for Research and Applications reanalysis data products (Rienecker et al., 2011) over the period 1979 to 2011.

In contrast to the troposphere, the stratosphere (taken to be from the tropopause to the top of the atmosphere) is near radiative equilibrium. The stratospheric temperature structure is therefore sensitive to the concentrations of radiatively active gases. If the stratosphere is optically thin and heated by upwelling radiation, it will be isothermal at the atmospheric skin temperature ( $T = (I(1 - \alpha)/8\sigma)^{1/4} \approx 203$  K,

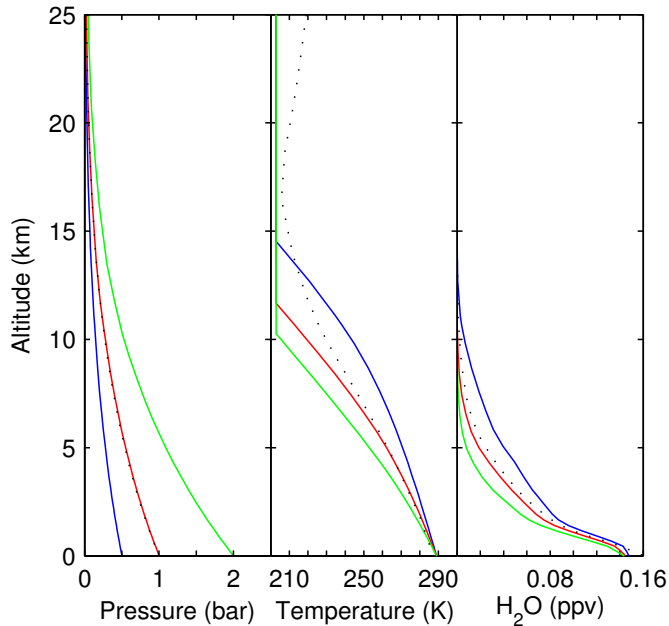


Figure 4.2: **Atmospheric Profiles.** Pressure, temperature and water vapor structure of atmospheres with 0.5 bar (blue), 1 bar (red), and 2 bar (green) of  $\text{N}_2$ . The modern atmosphere is also shown (dotted). The water vapor concentrations are scaled to an atmosphere with 1 bar of  $\text{N}_2$ .

Pierrehumbert, 2010). We take this to be the case in our calculations. In reality, the stratosphere would not have been optically thin, as  $\text{CO}_2$  (and possibly other gases) were likely optically thick for some wavelengths, which would have cooled the stratosphere. Other gases, such as  $\text{CH}_4$ , may have significantly warmed the stratosphere by absorbing solar radiation. However, the concentrations of these gases are poorly constrained. Since there is no convincing reason to choose any particular profile, we keep the stratosphere at the skin temperature for simplicity. The atmospheric profiles are shown in figure 4.2. We take the tropopause as the atmospheric level at which the pseudoadiabatic lapse rate reaches the skin temperature. Sensitivity tests were performed to examine the sensitivity of radiative forcing to the temperature and water vapour structure. We find that differences in radiative forcing are generally small ( $\leq 10\%$ , appendix A.2).

In this study, we explicitly include clouds in our radiative transfer calculations. Following Kasting et al. (1984), many RCMs used to study the Archean climate have omitted clouds, and adjusted the surface albedo such that the modern surface temperatures can be achieved with the current atmospheric composition and inso-

lation. Goldblatt and Zahnle (2011a) showed that neglecting the effects of clouds on longwave radiation can lead to significant over-estimates of radiative forcings, as clouds are strong absorbers of longwave radiation, which is largely independent of wavenumber. Clouds act as a new surface of emission to the top of the atmosphere and, therefore, the impact on the energy budget of molecular absorption between clouds and the surface is greatly reduced. We take our cloud climatology as cloud fractions and optical depths from International Satellite Cloud Climatology Project D2 data set, averaging from January 1990 to December 1992. This period is used by Rossow et al. (2005) and was chosen so that we could compare cloud fractions. We assume random overlap and average by area to estimate cloud fractions. The clouds were placed at 226 K for high clouds, 267 K for middle clouds and 280 K for low clouds, this corresponds to the average temperature levels of clouds on the modern Earth. The cloud climatology of the Archean atmosphere is highly uncertain. Recent GCM studies have found that there may have been less cloud cover due to less surface heating from reduced insolation (Charnay et al., 2013; Wolf and Toon, 2013). Other studies have suggested other mechanisms which could have caused significant changes in cloud cover during the Archean (Rondanelli and Lindzen, 2010; Rosing et al., 2010; Shaviv, 2003) although theoretical problems have been found with all of these studies (Goldblatt and Zahnle, 2011a,b). Nevertheless, given the large uncertainties in the cloud climatology in the Archean the most straight forward assumption is to assume modern climatology, even though there were likely differences in the cloud climatology. Furthermore, the goal of this study is to examine greenhouse forcings and not cloud forcings. Therefore, we want to capture the longwave effects of clouds to a first order degree. Differences in cloud climatology have only secondary effects on the results given here.

Atmospheric profiles are provided in appendix A.4. Cloud properties are the same as chapter 3 and are provided in appendix A.3.

#### 4.2.4 Radiative Forcing Calculations

Radiative forcing is calculated by performing radiative transfer calculations on atmospheric profiles with perturbed and unperturbed greenhouse gas concentrations and taking the difference in net flux of radiation at the tropopause. We assume the gases examined here are well-mixed.

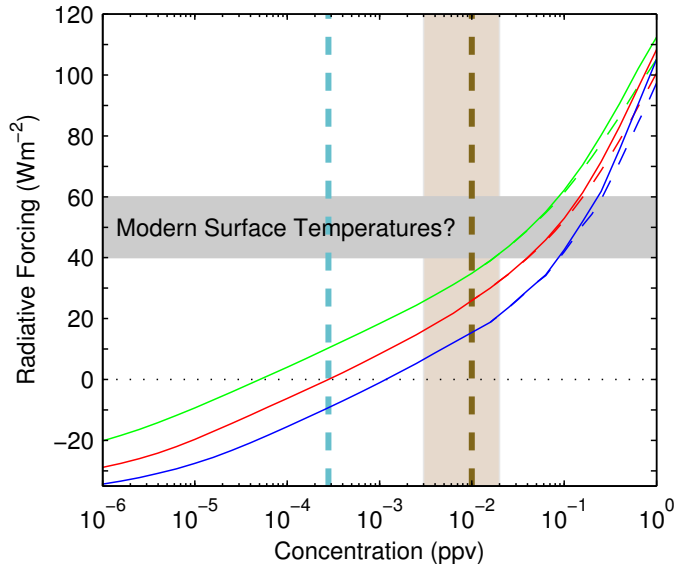


Figure 4.3: **CO<sub>2</sub> Radiative Forcings.** Radiative forcing as a function of CO<sub>2</sub> concentration, relative to pre-industrial CO<sub>2</sub> (1 bar N<sub>2</sub>). Colors are for atmospheres with 0.5 bar, 1 bar, and 2 bar of N<sub>2</sub>. Solid lines are calculated with CIA and dashed lines are calculated without CIA. The shaded region shows the range of CO<sub>2</sub> for the early Earth (3,000-20,000 ppmv, Driese et al., 2011). The vertical dashed blue and brown lines give the pre-industrial and early Earth best guess (10,000 ppmv) concentrations of CO<sub>2</sub>. Shaded grey region shows the range of radiative forcings over which a GAM surface temperature of 290 K could be sustained, depending on the climate sensitivity.

## 4.3 Results and Discussion

### 4.3.1 CO<sub>2</sub>

We calculate CO<sub>2</sub> radiative forcings up to 1 bar (figure 4.3). Our results show that at 10,000 ppmv, the radiative forcings are 35 Wm<sup>-2</sup> (2 bar), 26 Wm<sup>-2</sup> (1 bar), and 15 Wm<sup>-2</sup> (0.5 bar), which is considerably short of the forcing required to solve the FYSP, consistent with previous work. The CO<sub>2</sub> forcings given here account for changes in the atmospheric structure due to changes in the N<sub>2</sub> inventory and thus are non-zero at pre-industrial CO<sub>2</sub> for 0.5 bar and 2 bar of N<sub>2</sub>. This results in forcings of about 10 Wm<sup>-2</sup> (2 bar) and -9 Wm<sup>-2</sup> (0.5 bar) at pre-industrial CO<sub>2</sub> concentrations (see Goldblatt et al., 2009a, for a detailed physical description).

At very high CO<sub>2</sub> concentrations (> 0.1 bar), CO<sub>2</sub> becomes a significant fraction of the atmosphere. This complicates radiative forcing calculations by changing (1)

the atmospheric structure, (2) shortwave absorption/scattering, and (3) uncertainties in the parametrization of continuum absorption. These need careful consideration in studies of very high atmospheric CO<sub>2</sub>, so we describe these factors in detail:

1. Large increases in CO<sub>2</sub> appreciably increases the atmospheric pressure, and therefore, also increases the atmospheric lapse rate. This results in a cooling of the tropopause and reduction to the emission temperature. The atmospheric H<sub>2</sub>O concentration decreases and the absorption lines of all of the radiatively active gases are broadened. This increases absorption of CO<sub>2</sub> due to line broadening, but also effects the overlap with H<sub>2</sub>O. The changes in climatology with increasing pressure are also highly idealized using our simple atmospheric profile.
2. Shortwave radiation is also affected by very high CO<sub>2</sub> concentrations. The shortwave forcing is 2 Wm<sup>-2</sup> at 0.01 bar, 4 Wm<sup>-2</sup> at 0.1 bar and 18 Wm<sup>-2</sup> at 1 bar. There are two separate reasons for this. The smaller effect is absorption of shortwave radiation by CO<sub>2</sub> which primarily affects wavenumbers less than  $\approx 10,000$  cm<sup>-1</sup> (figure 4.9). The most important effect (CO<sub>2</sub> > 0.1 bar) is increased Rayleigh scattering due to the increase in the size of the atmosphere. This primarily affects wavenumbers larger than  $\approx 10,000$  cm<sup>-1</sup> and is the primary reason for the large difference in insulations through the tropopause between 0.1 and 1 bar of CO<sub>2</sub>.
3. There is significant uncertainty in the CO<sub>2</sub> spectra at very high concentrations. This is primarily due to absorption that varies smoothly with wavenumber that cannot be accounted for by nearby absorption lines. This absorption is termed continuum absorption and is caused by the far wings of strong lines and collision induced absorption (CIA) (Halevy et al., 2009b). Halevy et al. (2009b) show that different parametrizations of line and continuum absorption in different radiative transfer models can lead to large differences in outgoing longwave radiation at high CO<sub>2</sub> concentrations. SMART treats the continuum by using a  $\chi$ -factor to reduce the opacity of the Voigt line shape out to 1000 cm<sup>-1</sup> from the line center to match the background absorption. We add to this CIA absorption which has been updated with recent results of Wordsworth et al. (2010). We believe that our radiative transfer runs are as accurate as possible given the poor understanding of continuum absorption. Furthermore, large

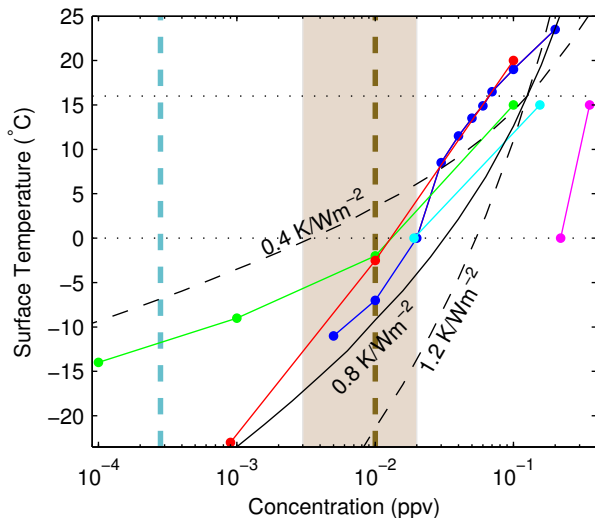


Figure 4.4: **Surface temperature as a function of CO<sub>2</sub> concentration for 0.8 S<sub>0</sub>.** Temperatures are calculated from radiative forcings assuming climate sensitivity parameters of 0.4 K/Wm<sup>-2</sup> (dashed black), 0.8 K/Wm<sup>-2</sup> (solid black) and 1.2 K/Wm<sup>-2</sup> (dashed black) and a surface temperature of 289 K at 0.13 bar of CO<sub>2</sub> (when our model is in energy balance). The results of Wolf and Toon (2013) (blue), Haqq-Misra et al. (2008) (green), Charnay et al. (2013) (red), von Paris et al. (2008) (cyan), and Kienert et al. (2012) (magenta) are also shown. Vertical dashed lines and shaded region are as in figure 4.3.

difference attained in outgoing longwave fluxes do not necessarily translate to large differences in radiative forcing. In radiative forcings calculations, the absolute value of outgoing longwave radiation is not important, but the change in fluxes with changing CO<sub>2</sub> concentrations are what matters.

It is worthwhile comparing our calculated radiative forcings with previous results. In most studies, the greenhouse warming from a perturbation in greenhouse gas concentration is quantified as a change of the GAM surface temperature. We convert our radiative forcings to surface temperatures for comparison using equation 2.14. Assuming the climate sensitivity to be in the range 1.5–4.5 Wm<sup>-2</sup> (medium confidence range, IPCC, 2013) for a doubling of atmospheric CO<sub>2</sub> and the radiative forcing for a doubling of CO<sub>2</sub> to be 3.7 Wm<sup>-2</sup>, we find a range of climate sensitivity parameters of 0.4–1.2 K/Wm<sup>-2</sup> with a best guess of 0.8 K/Wm<sup>-2</sup>. For a reference state, we take the CO<sub>2</sub> concentration (0.13 bar) which gives energy balance at the tropopause to be the concentration that gives a surface temperature of 289 K.

The calculated temperature curves are plotted with the results of previous studies

(figure 4.4). For all of the studies, surface temperatures were calculated for  $0.8S_0$ . However there were differences in the atmospheric pressure: von Paris et al. (2008) and Kienert et al. (2012) have 0.77 bar and 0.8 bar of  $N_2$  respectively, while Haqq-Misra et al. (2008), Wolf and Toon (2013) and Charnay et al. (2013) hold the surface pressure at 1 bar, and remove  $N_2$  to add  $CO_2$ .

We examine the range of climate sensitivities to a doubling of  $CO_2$  from the literature. The sensitivities can be grouped by the type of climate model used. Simple 1-D RCMs (Haqq-Misra et al., 2008; von Paris et al., 2008) have the lowest climate sensitivities (1-4 K). The 3-D models had higher climate sensitivities, but the sensitivities were also more variable between models. Kienert et al. (2012) use a model with a fully dynamic ocean but a statistical dynamical atmosphere. The sea-ice albedo feedback makes the climate highly sensitive to  $CO_2$  concentration and has the largest climate sensitivity ( $\approx 18.5$  K). Charnay et al. (2013) and Wolf and Toon (2013) use models with fully dynamic atmosphere but with simpler oceans. They generally have climate sensitivities between 2.5-4.5 K but Wolf and Toon (2013) find higher climate sensitivities (7-11 K) for  $CO_2$  concentrations of 10,000–30,000 ppmv due to changes in surface albedo (sea ice extent). The climate sensitivities are larger for the 3-D models compared to the RCMs primarily because of the ice-albedo feedback. It should also be noted that variations in climate sensitivity parameters mask variations in radiative forcings.

The concentration of  $CO_2$  required to reach modern day surface temperatures is variable between models. Charnay et al. (2013) and Wolf and Toon (2013) require the least  $CO_2$  to sustain modern surface temperatures, primarily because there are less clouds (low and high), the net effect of which is a decrease in albedo. The cloud feedback in these models works as follows: the reduced insolation results in less surface heating, which results in less evaporation and less cloud formation. The RCM studies require  $CO_2$  concentration very close to our results, especially considering differences in atmospheric pressure. Kienert et al. (2012) requires very high  $CO_2$  concentrations to prevent runaway glaciation because of the high sensitivity of the ice-albedo feedback in this model.

### 4.3.2 $CH_4$

We calculate  $CH_4$  radiative forcings up to 10,000 ppmv (figure 4.5). We find considerable shortwave absorption at concentrations  $> 100$  ppmv. For an atmosphere

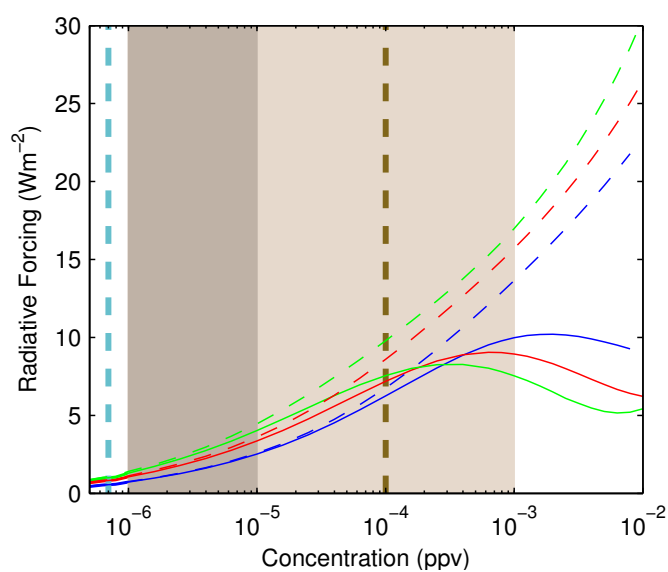


Figure 4.5: **Radiative Forcing for  $\text{CH}_4$ .** Radiative forcing as a function of  $\text{CH}_4$  for atmospheres with 0.5 bar (blue), 1 bar (red) and 2 bar (green) of  $\text{N}_2$ . Dashed curves show the longwave forcing. Shaded region shows the range of  $\text{CH}_4$  for the early Earth that could be sustained by abiotic (dark) and biotic (light) sources. The vertical dashed blue and brown lines give the pre-industrial and early earth best guess (100 ppmv, Goldblatt et al., 2006) concentrations of  $\text{CH}_4$ , respectively.

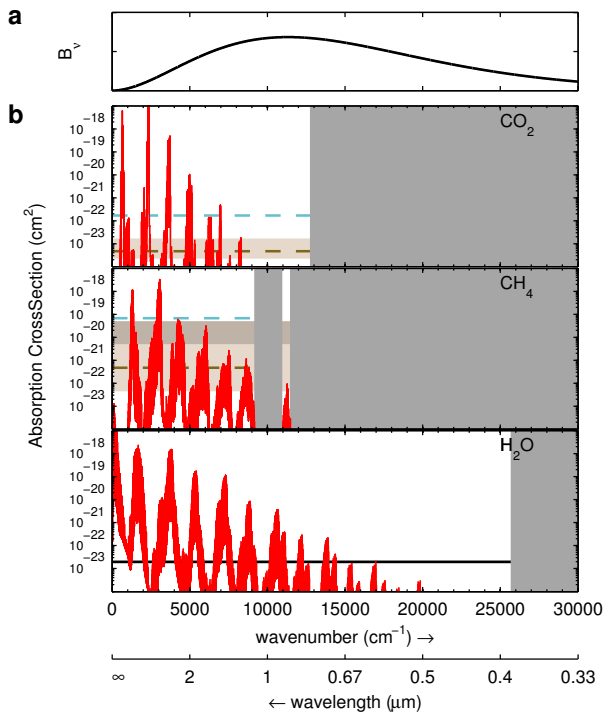


Figure 4.6: **Solar absorption cross-sections.** (a) Emission spectrum for an object of 5777 K (Effective emitting temperature of modern sun). (b) Absorption cross-sections of  $\text{CO}_2$ ,  $\text{CH}_4$  and  $\text{H}_2\text{O}$  calculated from line data (red) and measured cross-sections from the PNNL database (blue). Solid black line shows where HITRAN line data are available. Shaded and dashed lines show absorption cross-sections of unity optical depth for concentrations given in figures 4.3 and 4.5.

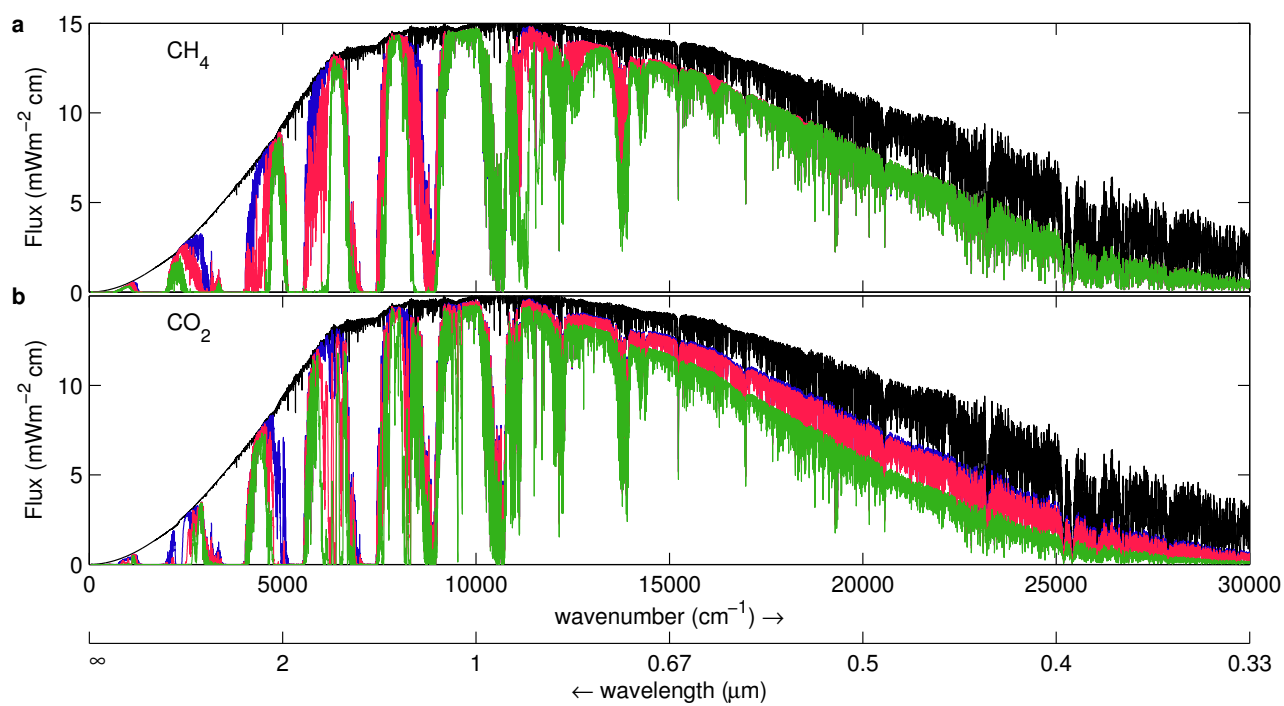


Figure 4.7: **Downward shortwave flux.** (a) Insolation at the top of the atmosphere (black) and surface for CH<sub>4</sub> concentrations 1 ppmv (blue), 100 ppmv (red), and 10,000 ppmv (green). (b) Insolation at the top of the atmosphere (black) and surface for CO<sub>2</sub> concentrations of 1,000 ppmv (blue), 0.1 bar (red), and 1 bar (green).

with 1 bar of  $N_2$ , the absorption of solar radiation in the stratosphere is  $\approx 1.4 \text{ Wm}^{-2}$  at 100 ppmv,  $\approx 6.7 \text{ Wm}^{-2}$  at 1000 ppmv, and  $\approx 20 \text{ Wm}^{-2}$  at 10,000 ppmv. Studies from Jim Kasting’s group (Pavlov et al., 2000; Haqq-Misra et al., 2008) parameterize solar absorption, but have much less absorption than found here. The HITRAN line data does not cover the entire solar spectrum but only goes up to  $11,502 \text{ cm}^{-1}$  (figure 4.6). Above this wavenumber we use absorption cross-sections to parameterize absorption. We find that the majority of the solar absorption occurs over wavelengths where HITRAN line data exists (figure 4.7).

Very strong shortwave absorption would have a significant effect on the temperature structure of the stratosphere. Strong absorption would lead to strong stratospheric warming which would limit the usefulness of our results. Nevertheless, our calculations indicate that at 100 ppmv of  $CH_4$  the combined thermal and solar radiative forcings are  $7.6 \text{ Wm}^{-2}$  (2 bar of  $N_2$ ),  $7.2 \text{ Wm}^{-2}$  (1 bar of  $N_2$ ), and  $6.2 \text{ Wm}^{-2}$  (0.5 bar of  $N_2$ ) and the thermal radiative forcings are  $9.8 \text{ Wm}^{-2}$  (2 bar of  $N_2$ ),  $8.6 \text{ Wm}^{-2}$  (1 bar of  $N_2$ ), and  $6.8 \text{ Wm}^{-2}$  (0.5 bar of  $N_2$ ). Therefore, excluding the effects of overlap (which are minimal, Byrne and Goldblatt, 2014), the combined thermal and solar radiative forcing due to 1000 ppmv of  $CO_2$  and 100 ppmv of  $CH_4$  are  $42.6 \text{ Wm}^{-2}$  (2 bar of  $N_2$ ),  $33.2 \text{ Wm}^{-2}$  (1 bar of  $N_2$ ) and  $21.2 \text{ Wm}^{-2}$  (0.5 bar of  $N_2$ ), significantly short of the forcings needed to sustain modern surface temperatures.

As with  $CO_2$ , we compare our  $CH_4$  radiative forcings to values given in literature (figure 4.8). Temperatures are calculated from radiative forcings assuming a surface temperature of 271 K for 0 ppmv of  $CH_4$  and climate sensitivity parameters of  $0.4 \text{ K/Wm}^{-2}$ ,  $0.8 \text{ K/Wm}^{-2}$  and  $1.2 \text{ K/Wm}^{-2}$ , and a background  $CO_2$  concentration of 10,000 ppmv. Due to absorption of shortwave radiation, our calculated surface temperatures decrease for concentrations above 1,000 ppmv. Results from Pavlov et al. (2000) are included even though they are known to be erroneous as an illustration of the utility of these comparisons. All other studies give similar surface temperatures.

### 4.3.3 Trace Gases

The chemical cycles of several other greenhouse gases have been studied in the Archean. It has been hypothesized that higher atmospheric concentrations could have been sustained making these gases important for the planetary energy budget. High concentrations of  $NH_3$  (Sagan and Mullen, 1972),  $C_2H_6$  (Haqq-Misra et al.,

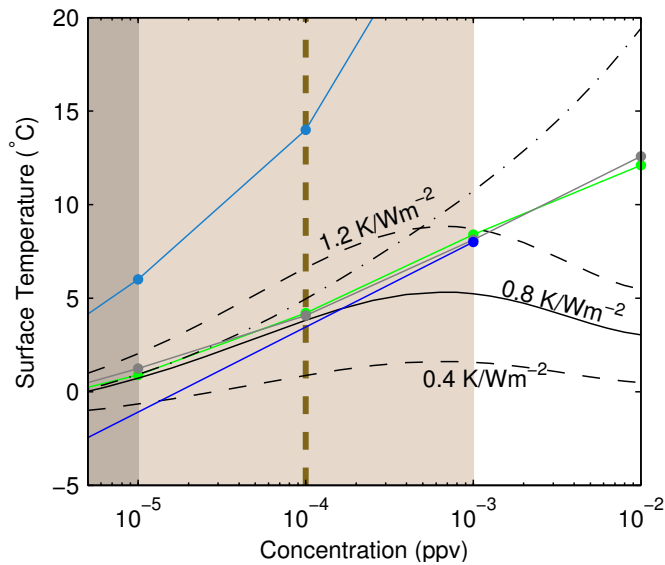


Figure 4.8: **Surface temperature as a function of CH<sub>4</sub> concentration for 0.8 S<sub>0</sub>.** Temperatures are calculated from radiative forcings assuming a surface temperature of 271 K for 0 ppmv of CH<sub>4</sub> and climate sensitivity parameters of 0.4 K/Wm<sup>-2</sup> (dashed black), 0.8 K/Wm<sup>-2</sup> (solid black) and 1.2 K/Wm<sup>-2</sup> (dashed black) and a background CO<sub>2</sub> concentration of 10,000 ppmv. Dashed-Dotted black line shows the longwave radiative forcing. The results of Wolf and Toon (2013) (blue), Haqq-Misra et al. (2008) (green), Pavlov et al. (2000) (turquoise), and Kiehl and Dickinson (1987) (grey) are also plotted. Temperatures for Kiehl and Dickinson (1987) are found from radiative forcings assuming a climate sensitivity parameter of 0.81 K/Wm<sup>-2</sup> and a surface temperature of 271 K for 0 ppmv of CH<sub>4</sub>.

2008),  $\text{N}_2\text{O}$  (Buick, 2007), and  $\text{OCS}$  (Ueno et al., 2009) have all been proposed in the Archean. There are many other greenhouse gases in the HITRAN database that have not been studied, whether these gases could have been sustained at radiatively important concentrations is beyond the scope of this paper. Here we quantify the warming these gases could have provided in the Archean.

### Radiative Forcings

We produce a first order estimate of the relative absorption strength of the HITRAN gases by taking the product of the irradiance produced by a blackbody of 289 K and the absorption cross-sections to get the absorption per molecule of a gas when saturated with radiation (Figure 4.9). Using this metric,  $\text{H}_2\text{O}$  ranks as the 11<sup>th</sup> strongest greenhouse gas, and  $\text{CO}_2$  and  $\text{CH}_4$  rank 16<sup>th</sup> and 27<sup>th</sup> respectively. This demonstrates that many of the HITRAN gases are strong greenhouse gases and that it is conceivable that low concentrations of these gases could have a significant effect on the energy budget.

We calculate the radiative forcings for the strongest HITRAN gases over the range of 10 ppbv to 10 ppmv (figure 4.10), assuming the gases are well-mixed. The radiative forcings are calculated in an atmosphere which contains only  $\text{H}_2\text{O}$  and  $\text{N}_2$ . Many of the gases reach forcings greater than  $10 \text{ Wm}^{-2}$  at concentrations less than 1 ppmv. Gases for which the measured and calculated cross-sections disagree, we give rough estimates of the expected radiative forcings assuming the PNNL cross-sections are correct. We have made approximate corrections to the forcings as follows. For some gases the shape of the absorption cross-sections were the same but the magnitude was offset. For these gases, we adjust the concentrations required for a given forcing, this was done for  $\text{CH}_3\text{OH}$  (x10),  $\text{CH}_3\text{Br}$  (x13),  $\text{C}_2\text{H}_4$  (x0.1), and  $\text{H}_2\text{O}_2$  (x2). Missing spectra was compensated for by adding the radiative forcings from other gases that had similar spectra. For  $\text{CH}_3\text{OH}$  the  $\text{C}_2\text{H}_4$  forcings were added. For  $\text{HCOOH}$  we added the  $\text{HCN}$  forcing. For  $\text{NO}_2$  we added the  $\text{HOCl}$  forcing.

There are significant differences in radiative forcing due to different  $\text{N}_2$  inventories. The differences in radiative forcing due to difference in atmospheric pressure varies from gas to gas. Generally, the differences in forcing due to differences in atmospheric structure are similar, but the differences due to pressure broadening are more variable. Broadening is most effective for gases which have broad absorption features with highly variable cross-sections, because the broadening of the lines covers the areas

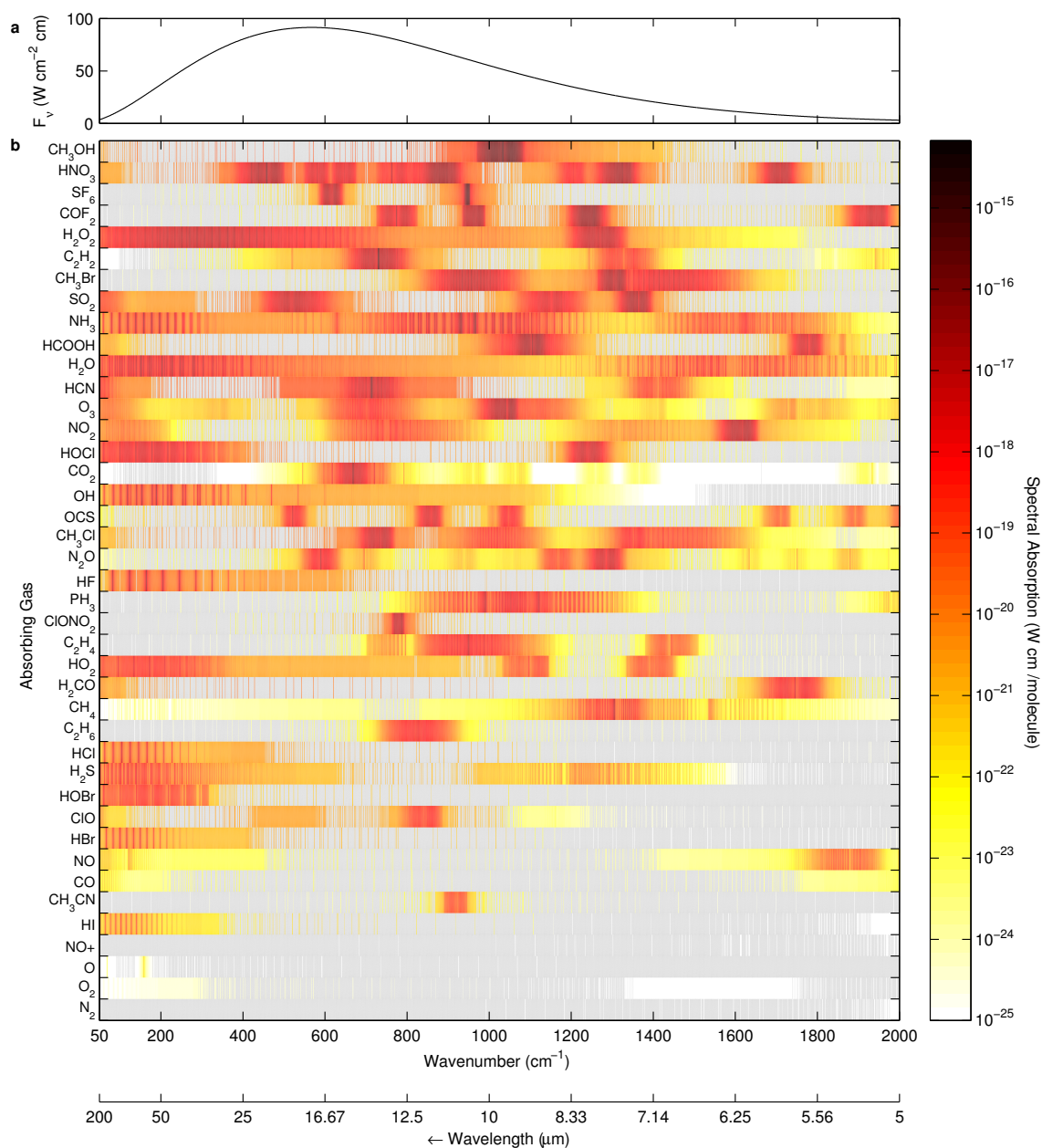


Figure 4.9: **Spectral absorption of blackbody emissions.** (a) Emission intensity from a blackbody of 289 K. (b) Product of emission intensity and absorption cross-sections for gases from the HITRAN 2012 database. Gases are ordered by decreasing spectrum integrated absorption strength from top to bottom. Grey indicates wavenumbers where no absorption data are available. Absorption coefficients were calculated at 500 hPa and 260 K.

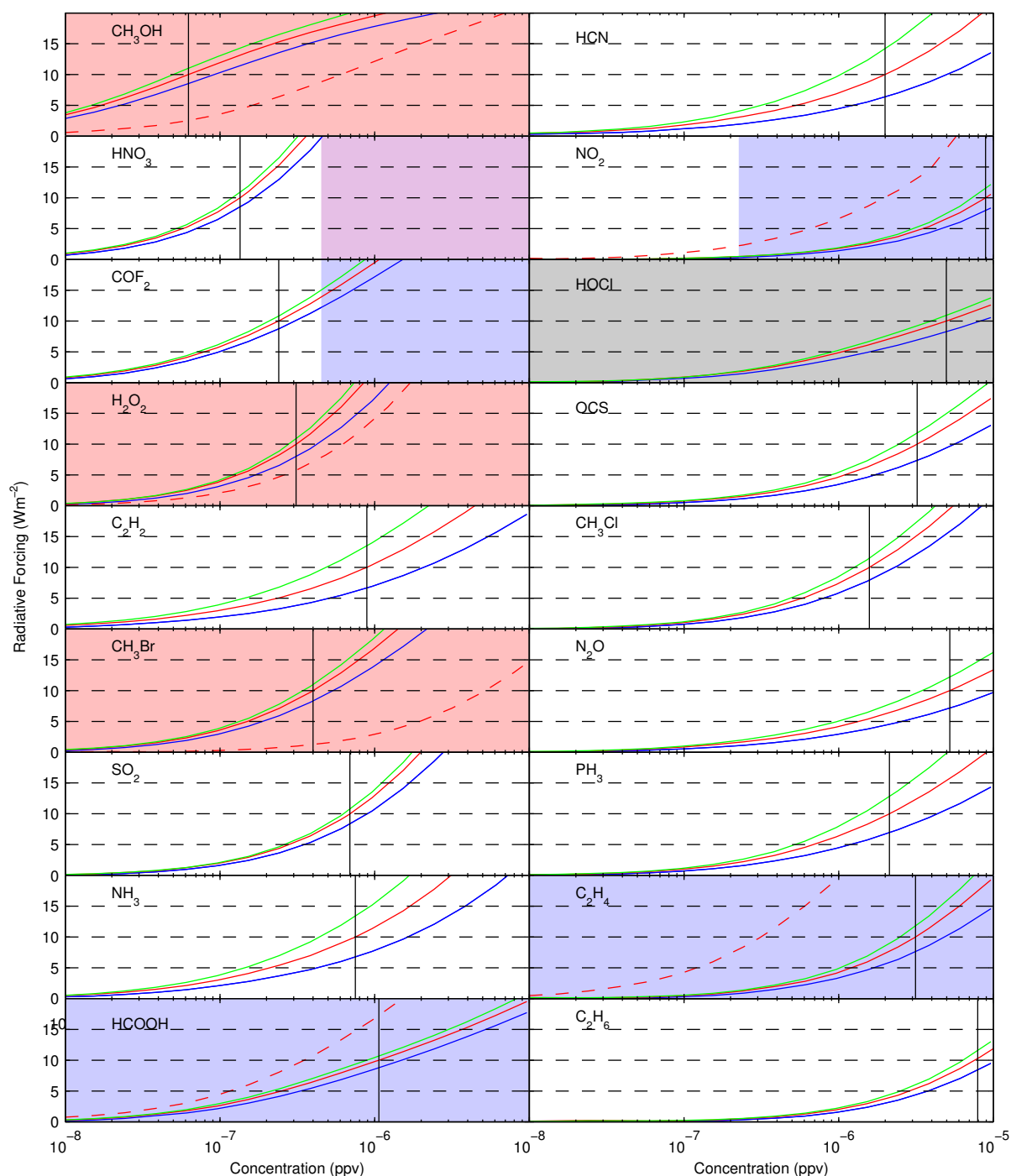


Figure 4.10: **Trace gas radiative forcings.** All sky radiative forcings for potential early Earth trace gases, colors are as in figure 4.2. Gases are ordered as in figure 4.3. Shading indicates concentrations where computed cross-sections from HITRAN data were in poor agreement with the PNNL data. The colors indicate areas where HITRAN data underestimates (blue), overestimates (red), or both at different frequencies (purple). Grey shading indicates where no PNNL data were available. Vertical black lines show the concentration at which the radiative forcing is  $10 \text{ W m}^{-2}$  for a 1 bar atmosphere. Dotted red lines give rough estimates of the radiative forcing accounting for incorrect spectral data. Concentrations are scaled to an atmosphere with 1 bar of  $\text{N}_2$ .

with weak absorption. Such gases include  $\text{NH}_3$ ,  $\text{HCN}$ ,  $\text{C}_2\text{H}_2$  and  $\text{PH}_3$ . At 5 ppmv, 55-60 percent of the difference in radiative forcing between atmospheres can be attributed to pressure broadening for these gases. Where as,  $\text{NO}_2$  and  $\text{HOCl}$  which have strong but narrow absorption features show the least difference in forcing due to pressure broadening (20-23%).

## Overlap

Here we examine the reduction in radiative forcing due to overlap. The concentrations of  $\text{CO}_2$  and  $\text{CH}_4$  are expected to be quite high in the Archean. Trace gases which have absorption bands coincident with the absorption bands of  $\text{CO}_2$  and  $\text{CH}_4$  will be much less effective at warming the Archean atmosphere.

We examine the effect of overlap on radiative forcing by looking at several cases with varying concentrations of  $\text{CO}_2$ ,  $\text{CH}_4$  (figure 4.11), and other trace gases (figure 4.12). The magnitude of overlap can vary substantially between the gases in question. For the majority of gases overlap with  $\text{CO}_2$  is the largest. The reduction in forcing is generally between 10–30% but can be as high as 86%. The reduction in forcing are largest for  $\text{HCN}$  (86%)  $\text{C}_2\text{H}_2$  (78%),  $\text{CH}_3\text{Cl}$  (71%)  $\text{NO}_2$  (52%), and  $\text{N}_2\text{O}$  (33%) all with 0.01 bar of  $\text{CO}_2$ . All of these gases have significant absorption bands in the 550-850  $\text{cm}^{-1}$  wavenumber region where  $\text{CO}_2$  absorbs the strongest. Of particular interest is  $\text{N}_2\text{O}$  which has previously been proposed to have built up to significant concentrations on the early Earth (Buick, 2007).  $\text{C}_2\text{H}_2$  could also have been produced by a hypothetical early Earth haze, although previous studies have found that it would not build up to radiatively important concentrations (Haqq-Misra et al., 2008).

The reduction in forcing due to  $\text{CH}_4$  is generally less than 20% but can be as high as 37%. The reductions in forcing are largest for  $\text{HOCl}$  (33%)  $\text{N}_2\text{O}$  (32%)  $\text{COF}_2$  (25%)  $\text{H}_2\text{O}_2$  (21%) all with 100 ppmv of  $\text{CH}_4$ . All of which have absorption bands in 1200–1350  $\text{cm}^{-1}$ . As with  $\text{CO}_2$ , the radiative forcing from  $\text{N}_2\text{O}$  is significantly reduced due to overlap with  $\text{CH}_4$ , suggesting that  $\text{N}_2\text{O}$  is not a good candidate to produce significant warming on early Earth except at very high concentrations.

We calculate the reduction in radiative forcing due to overlap between trace gases (figure 4.12). There is a large amount of overlap between  $\text{C}_2\text{H}_2$ ,  $\text{CH}_3\text{Cl}$  and  $\text{HCN}$  resulting in a reduction in radiative forcing of  $\approx 30\%$ . All three gases have their strongest absorption bands in the region 700–850  $\text{cm}^{-1}$  and have a secondary absorption band in the region 1250–1500  $\text{cm}^{-1}$  which are on the edges of the water vapour

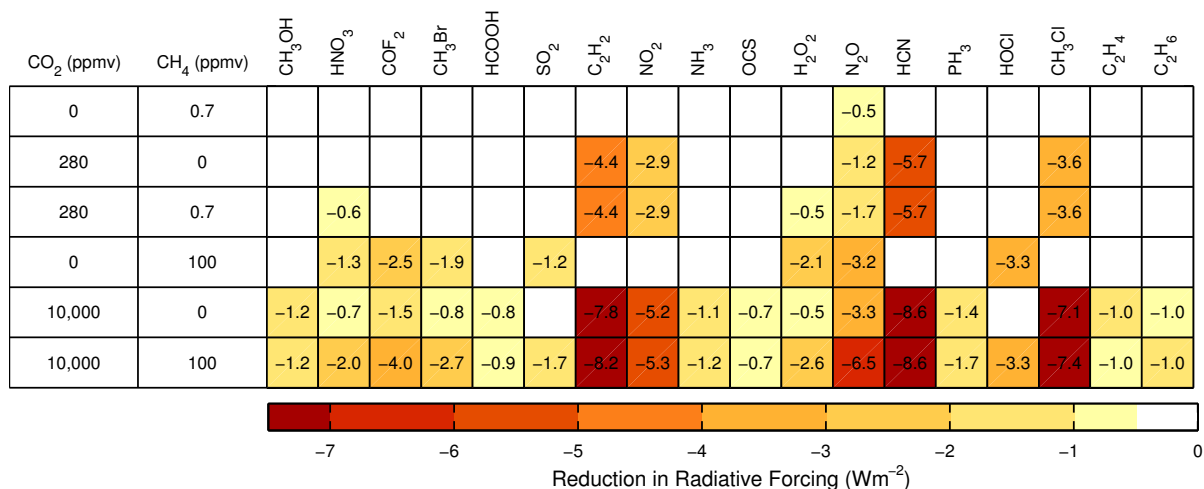


Figure 4.11: **Overlap with CO<sub>2</sub> and CH<sub>4</sub>.** Reduction in radiative forcing due to overlapping absorption. Trace gas concentrations are held at the concentrations which gives a 10 Wm<sup>-2</sup> radiative forcing for an atmosphere with 1 bar of N<sub>2</sub>.

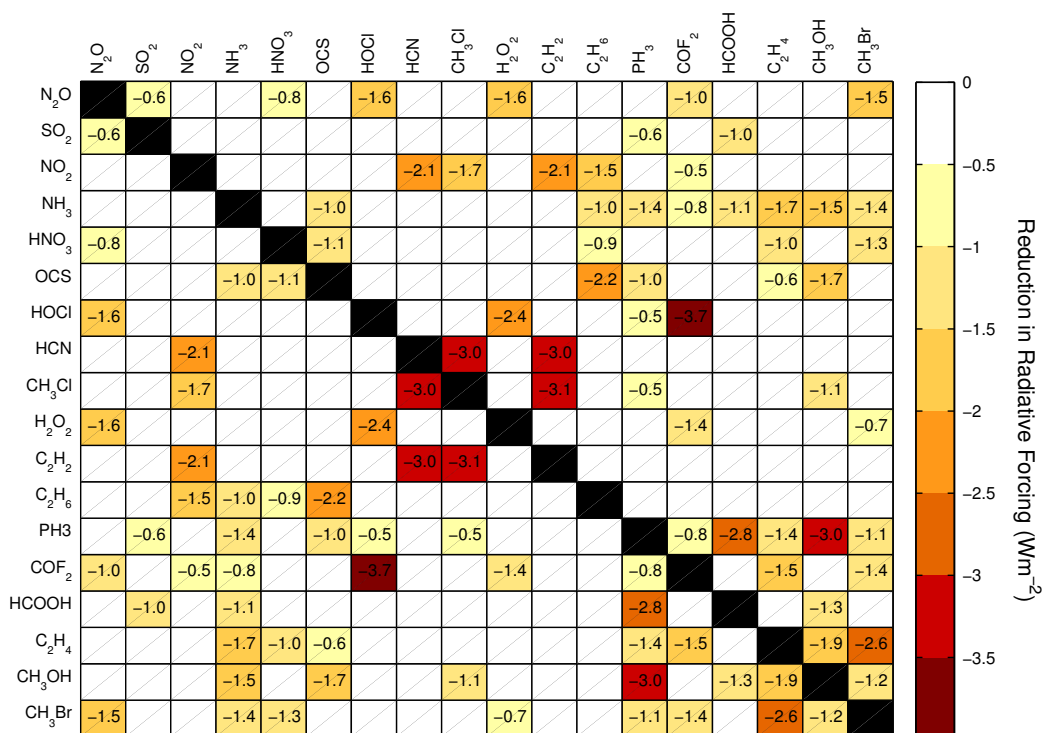


Figure 4.12: **Trace gas overlap.** Reduction in radiative forcing due to overlapping absorption. Gas concentrations are held at concentrations which give a 10 Wm<sup>-2</sup> radiative forcing for an atmosphere with 1 bar of N<sub>2</sub>.

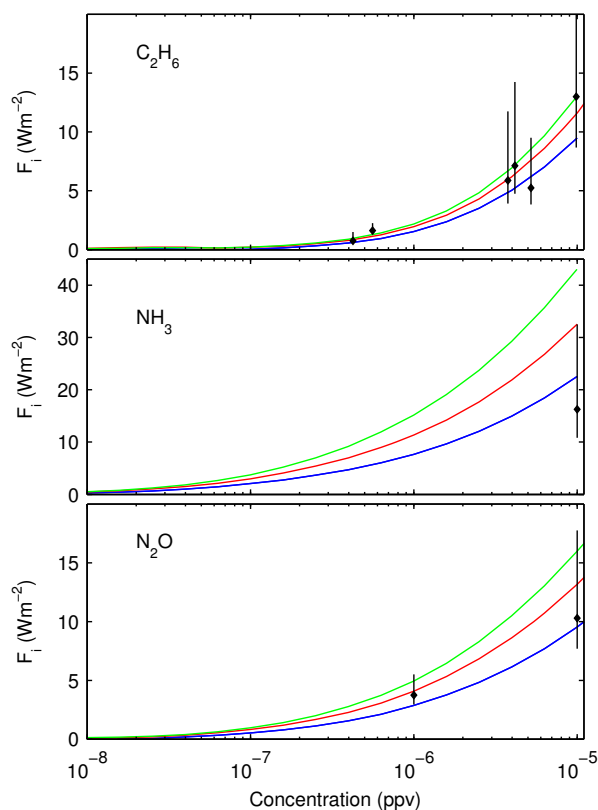


Figure 4.13: **Calculated Radiative forcings and inferred radiative forcings from literature.** Literature radiative forcings are inferred from temperature changes reported by Haqq-Misra et al. (2008) ( $\text{C}_2\text{H}_6$ ), Kuhn and Atreya (1979) ( $\text{NH}_3$ ) and Roberson et al. (2011) ( $\text{N}_2\text{O}$ ). Radiative forcings are calculated assuming a range of climate sensitivity parameters of  $0.4 \text{ K/Wm}^{-2}$  to  $1.2 \text{ K/Wm}^{-2}$  with a best guess of  $0.8 \text{ K/Wm}^{-2}$ .

window. All three gases have significant overlap with  $\text{CO}_2$ , for an atmosphere with 0.01 bar of  $\text{CO}_2$  the reductions in forcing are  $> 70\%$ .

Other traces gases with significant overlap are  $\text{COF}_2$  and  $\text{HOCl}$  (37%) due to coincident absorption bands at  $\approx 1250\text{cm}^{-1}$ , and  $\text{CH}_3\text{OH}$  and  $\text{PH}_3$  (30%) due to coincident absorption around  $\approx 1000\text{cm}^{-1}$ .

### Comparison between our results and previous calculations

We compare inferred radiative forcings from prior work to ours using the same method as for  $\text{CO}_2$  and  $\text{CH}_4$  (figure 4.13).

Inferred  $\text{C}_2\text{H}_6$  radiative forcings from Haqq-Misra et al. (2008) for a 1 bar atmosphere agree well with our results. Inferred  $\text{NH}_3$  from Kuhn and Atreya (1979) for

a 0.78 bar atmosphere agree well with our results, although, our results suggest that the results of Kuhn and Atreya (1979) are on the lower end of possible temperature changes. Inferred  $\text{N}_2\text{O}$  from Roberson et al. (2011) for a 1 bar atmosphere agree well with our results. Roberson et al. (2011) perform radiative forcing calculations with  $\text{CO}_2$  and  $\text{CH}_4$  concentrations of 320 ppmv and 1.6 ppmv. Due to overlap this forcing is likely reduced by  $\approx 50\%$  with early Earth  $\text{CO}_2$  and  $\text{CH}_4$  concentrations of 10,000 ppmv and 100 ppmv. Ueno et al. (2009) give a rough estimate of the radiative forcing due to 10 ppmv of OCS to be  $60 \text{ Wm}^{-2}$ . In this work we find the forcing to be much less than this ( $\approx 20 \text{ Wm}^{-2}$ ).

## 4.4 Conclusions

Using the SMART radiative transfer model and HITRAN line data, we have calculated radiative forcings for  $\text{CO}_2$ ,  $\text{CH}_4$  and 18 other HITRAN greenhouse gases on a hypothetical early Earth atmosphere. These forcings are available at several background pressures and we account for overlap between gases. We recommend the forcings provided here be used both as a first reference for which gases are likely good greenhouse gases, and as a standard set of calculations for validation of radiative forcing calculations for the Archean. Many of these gases can produce significant radiative forcings at low concentrations. Whether any of these gases could have been sustained at radiatively important concentrations during the Archean requires study with geochemical and atmospheric chemistry models.

Comparing our calculated forcings with previous work, we find that  $\text{CO}_2$  radiative forcings are consistent, but find a stronger shortwave absorption by  $\text{CH}_4$  than previously recorded. This is primarily due to strong absorption at wavenumbers less than  $11,502 \text{ cm}^{-1}$  where there are HITRAN line data. This new result suggests an upper limit to the warming  $\text{CH}_4$  could have provided of about  $10 \text{ Wm}^{-2}$ . Amongst the trace gases, we find that the forcing from  $\text{N}_2\text{O}$  was likely overestimated Roberson et al. (2011) due to underestimated overlap with  $\text{CO}_2$  and  $\text{CH}_4$ , and that the radiative forcing from OCS was greatly overestimated by Ueno et al. (2009).

# Chapter 5

## Conclusions

In this thesis I have examined the radiative forcings produced by extreme changes in greenhouse gases for both modern-type atmospheres with ozone layers and anoxic atmospheres. A summary of my general results are as follows:

### Modern Earth

I have provided new radiative forcing calculations for CO<sub>2</sub> (100–50,000 ppmv), CH<sub>4</sub> (100 ppbv–100 ppmv) and N<sub>2</sub>O (100 ppbv–100 ppmv) relevant to extreme anthropogenic climate change and Phanerozoic paleoclimate studies. I have examined the sensitivity of these forcings to spatial averaging and tropopause definition and found that only minor errors are introduced; differences in radiative forcing are less than 2% for CO<sub>2</sub> and N<sub>2</sub>O and about 7% for CH<sub>4</sub>. I provided simplified fits to these radiative forcings which are recommended in place of those from IPCC (2001) for high greenhouse gas concentrations. The IPCC fits for CO<sub>2</sub> based on WMO (1999) and Shi (1992) are in reasonable agreement with our calculations, however, the fit based on IPCC (1990) significantly underestimates the radiative forcing above 1000 ppmv, and the fits for CH<sub>4</sub> (> 20 ppmv) and N<sub>2</sub>O (> 10 ppmv) significantly overestimate the forcing.

I examined the reduction in radiative forcing due to overlap between CO<sub>2</sub>, CH<sub>4</sub> and N<sub>2</sub>O, which was found to be less than 0.1 Wm<sup>-2</sup> for concentrations up to RCP8.5 year 2250 values. For larger concentrations, N<sub>2</sub>O–CH<sub>4</sub> and N<sub>2</sub>O–CO<sub>2</sub> overlap can reduce the radiative forcing by several Wm<sup>-2</sup>. I provide simplified fits to account for this overlap.

The difference in radiative forcing between the tropics and the poles is consider-

able, and increases with the magnitude of radiative forcing (e.g., the meridional variation in forcing increases monotonically from 37% of the GAM forcing at 100 ppmv to 47% at 50,000 ppmv of CO<sub>2</sub>). Tables of these forcings are provided for use forcing intermediate complexity climate models.

### Early Earth

I have provided new radiative forcing calculations for CO<sub>2</sub> (1 ppmv–1 bar), CH<sub>4</sub> (500 ppbv–10,000 ppmv) and 18 other gases (10 ppbv–10 ppmv) for atmospheres with 0.5, 1, and 2 bar of N<sub>2</sub>. I recommend the forcings provided here be used as a standard set for validation of radiative forcing calculations.

I compared the forcings presented here with those recorded in literature. For CO<sub>2</sub>, I found that the radiative forcings presented here are consistent with previous results, although large uncertainty is introduced at very high concentrations (>0.1 bar) due to uncertainties in the atmospheric structure, shortwave absorption and scattering, and uncertainties in the parametrization of continuum absorption. For CH<sub>4</sub>, I found stronger shortwave absorption than previously recorded. I examined the cause of this and find that it is primarily due to strong absorption at wavenumbers less than 11,502 cm<sup>-1</sup> where HITRAN line data exists. This new result suggests an upper limit to the warming CH<sub>4</sub> could have provided of about 10 Wm<sup>-2</sup>.

For the other 18 gases, I found that significant radiative forcings can result from concentrations less than 1 ppmv. These results demonstrate that there exists a wide variety of greenhouse gases which could significantly warmed the Archean Earth if they were sustained at concentration of 0.1–10 ppmv. Whether any of these gases could have been sustained at radiatively important concentrations during the Archean requires study with geochemical and atmospheric chemistry models. Nevertheless, we can hypothesize about the likelihood of the gases examined here.

The Archean atmosphere was more reducing than the modern atmosphere. This would have favoured reduced gases and may have resulted in a lower rate of oxidation of many atmospheric greenhouse gases in the Archean relative today. There are several other gases which have oxidation by the hydroxyl radical as a major sink, including: CH<sub>3</sub>OH, CH<sub>3</sub>Cl, CH<sub>3</sub>Br, HCN, C<sub>2</sub>H<sub>2</sub>, C<sub>2</sub>H<sub>6</sub> and OCS.

CH<sub>3</sub>OH is of particular interest because it is the strongest greenhouse gas examined in this study, although the PNNL data suggests that the radiative forcings calculated here may be overestimates. Most absorption occurs due to a strong absorp-

tion band located in the water vapour window. Atmospheric  $\text{CH}_3\text{OH}$  concentrations in the modern atmosphere range from 0.1 to 1 ppbv in the free troposphere, which is among the largest concentrations of any of the non-traditional greenhouse gases examined in this work. The largest sources of  $\text{CH}_3\text{OH}$  in the modern atmosphere are the ocean biosphere, plant growth and decay, and atmospheric production from self reactions of  $\text{CH}_3\text{O}_2$  and with organic peroxy radicals. The largest sink of  $\text{CH}_3\text{OH}$  is oxidation by the hydroxyl radical. If sources in the Archean remained similar to today but the rate of oxidation decreased, it is plausible that  $\text{CH}_3\text{OH}$  could have had a significant effect on the planetary energy budget.

The effect of overlap and atmospheric pressure on radiative forcing is examined. Overlap can significantly reduce the radiative forcing due to coincident spectral bands. In particular, gases that have their strongest absorption bands on the edges of the water vapour window where  $\text{CO}_2$  and  $\text{CH}_4$  are strong absorbers can be very sensitive to the  $\text{CO}_2$  and  $\text{CH}_4$  concentrations. This work shows that there are many factors which affect radiative forcings which need to be considered more carefully in future research. Future studies examining the strength of a greenhouse gas in the Archean should test the sensitivity of their results to background greenhouse gas concentrations and atmospheric pressure.

# Appendix A

## Additional Information

### A.1 Upward and Downward Flux Equations

From the Schwarzschild equation,

$$\frac{d}{d\tau_\nu^*} I(\tau_\nu^*, \hat{n}, \nu) = -\frac{1}{\cos\theta} (I(\tau_\nu^*, \hat{n}, \nu) - B(\nu, T(\tau_\nu^*))), \quad (\text{A.0})$$

we can find the upward and downward flux equations. To get the net upward radiative flux ( $I_+$ ) for a given frequency we can multiply equation A.1 by  $\cos\theta$ , assume the distribution remains approximately isotropic, and then integrate over the upward facing hemisphere to get,

$$\frac{1}{2} \frac{d}{d\tau_\nu^*} I = -I + B(\nu, T(\tau_\nu^*)). \quad (\text{A.0})$$

Again assuming isotropy, the rate of decay of the isotropic beam is the same as for a unidirectional beam propagating at  $\bar{\theta} = 60^\circ$ . So,  $\tau_\nu = \tau_\nu^*/\cos\bar{\theta}$ , and we can re-write equation A.1 as,

$$\frac{d}{d\tau_\nu} I = -I + B(\nu, T(\tau)). \quad (\text{A.0})$$

Since, assuming isotropy,

$$\int_0^{2\pi} \int_0^{\frac{\pi}{2}} I \sin\theta d\theta d\phi = I \int_0^{2\pi} \int_0^{\frac{\pi}{2}} \sin\theta d\theta d\phi = 2\pi I,$$

the net upward flux per unit frequency  $I_+$  is given by,

$$I_+ = (2\pi I)\cos\bar{\theta} = (2\pi I)\left(\frac{1}{2}\right) = \pi I,$$

substituting for  $I_+$  into equation A.1, we get,

$$\frac{d}{d\tau_\nu}I_+ = -I_+ + \pi B(\nu, T(\tau)). \quad (\text{A.0})$$

Equation A.1 is the upward flux. Using the same method, the downward flux flux ( $I_-$ ) equation is,

$$\frac{d}{d\tau_\nu}I_- = I_- - \pi B(\nu, T(\tau)) \quad (\text{A.0})$$

## A.2 Sensitivity

Figure A.1 shows the fluxes, radiative forcings and percentage difference in radiative forcings for various possible GAM temperature and water vapour profiles for the early Earth. The effect on radiative forcing calculations from varying the stratospheric temperature from 170 K to 210 K while the tropopause temperature is kept constant are very small ( $< 3\%$ ). Varying the tropopause temperature between 170 K and 210 K results in larger differences in radiative forcing ( $< 10\%$ ). Changing the relative humidity effects radiative forcing by less than 5%. Radiative forcing calculations are sensitive to surface temperature. Changing the surface temperature from 290 K to 280 K or 300 K results in differences in radiative forcing of  $\leq 12\%$ . However, the difference in forcing between 270 K and 290 K is much larger (12–25%).

## A.3 Modern Earth Tables

This appendix contains the meridionally resolved forcings, atmospheric profiles and cloud climatology for chapter 3. Meridionally resolved radiative forcing are provided for  $\text{CO}_2$  (table A.1),  $\text{CH}_4$  (table A.2), and  $\text{N}_2\text{O}$  (table A.3). Atmospheric profiles are provided in tables C.4 through C.10 and cloud parameters are provided in tables C.11 through C.17.

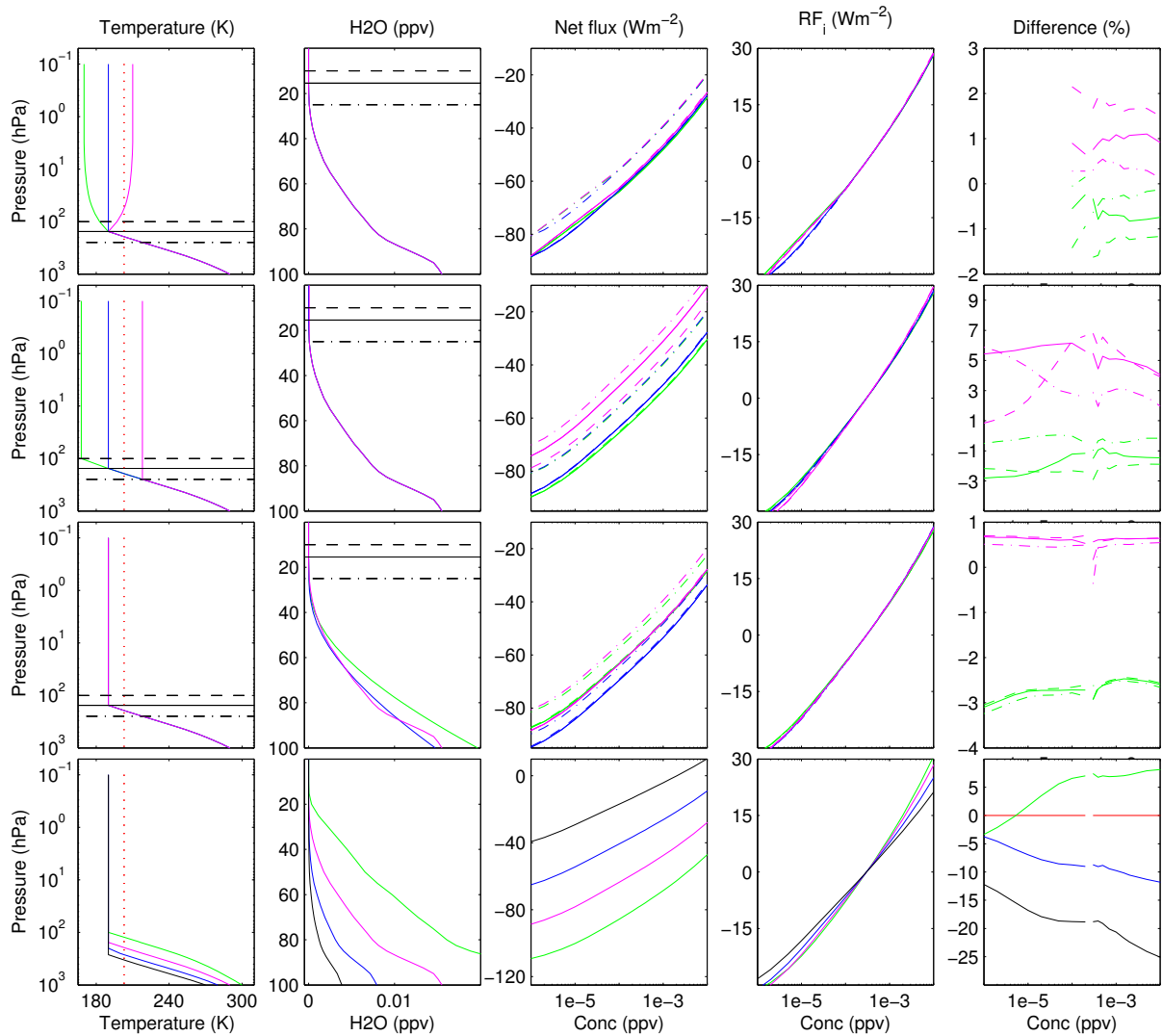


Figure A.1: **Sensitivity Study.** Columns from left to right: Temperature structure, H<sub>2</sub>O structure, Net flux of radiation at tropopause, radiative forcing, and percentage difference in radiative forcing. Solid, dashed and dashed-dotted curves represent different tropopause positions. Vertical dotted red line shows the atmospheric skin temperature (203 K).

Table A.1:  $\mathbf{F}_i$  ( $\text{Wm}^{-2}$ ) for  $\text{CO}_2$  as a function of latitude and concentrations. The average latitude ( $\text{Lat}_{avg}$ ) is the latitude at which there is an equal amount of area north and south within the segment.

		$\log_{10}(\text{CO}_2 \text{ concentration})$											
$\text{Lat}_{range}$	$\text{Lat}_{avg}$	-4.00	-3.80	-3.60	-3.56	-3.40	-3.20	-3.00	-2.80	-2.60	-2.40	-2.20	-2.00
GAM	$30.0^\circ$	-6.01	-3.32	-0.61	0	2.16	4.98	7.87	10.86	13.96	17.18	20.55	24.11
$00^\circ\text{-}15^\circ$	$7.5^\circ$	-6.28	-3.48	-0.65	0	2.25	5.21	8.26	11.43	14.76	18.25	21.92	25.82
$15^\circ\text{-}30^\circ$	$22.3^\circ$	-6.78	-3.75	-0.68	0	2.43	5.63	8.93	12.34	15.89	19.62	23.55	27.75
$30^\circ\text{-}45^\circ$	$37.1^\circ$	-6.05	-3.37	-0.61	0	2.18	5.04	7.92	10.91	13.99	17.19	20.54	24.09
$45^\circ\text{-}60^\circ$	$51.9^\circ$	-5.36	-2.95	-0.53	0	1.92	4.41	6.97	9.57	12.24	14.98	17.79	20.72
$60^\circ\text{-}75^\circ$	$66.3^\circ$	-4.87	-2.69	-0.49	0	1.74	4.00	6.32	8.67	11.07	13.51	16.02	18.64
$75^\circ\text{-}90^\circ$	$79.4^\circ$	-4.55	-2.51	-0.46	0	1.63	3.76	5.95	8.18	10.44	12.72	15.04	17.41

Table A.2:  $\mathbf{F}_i$  ( $\text{Wm}^{-2}$ ) for  $\text{CH}_4$  as a function of latitude and concentrations. The average latitude ( $\text{Lat}_{avg}$ ) is the latitude at which there is an equal amount of area north and south within the segment.

		$\log_{10}(\text{CH}_4 \text{ concentration})$																	
$\text{Lat}_{range}$	$\text{Lat}_{avg}$	-7.00	-6.80	-6.60	-6.57	-6.40	-6.20	-6.15	-6.00	-5.80	-5.60	-5.40	-5.20	-5.00	-4.80	-4.60	-4.40	-4.20	-4.00
GAM	$30.0^\circ$	-0.6	-0.55	-0.42	-0.40	-0.26	-0.06	0	0.18	0.47	0.82	1.24	1.74	2.32	3.01	3.79	4.67	5.64	6.66
$00^\circ-15^\circ$	$7.5^\circ$	-0.67	-0.58	-0.44	-0.42	-0.27	-0.06	0	0.19	0.49	0.86	1.29	1.82	2.42	3.15	3.98	4.91	5.94	7.02
$15^\circ-30^\circ$	$22.3^\circ$	-0.79	-0.67	-0.51	-0.49	-0.32	-0.07	0	0.22	0.58	1.00	1.51	2.12	2.82	3.65	4.60	5.68	6.84	8.08
$30^\circ-45^\circ$	$37.1^\circ$	-0.67	-0.57	-0.44	-0.42	-0.27	-0.07	0	0.18	0.49	0.84	1.28	1.80	2.41	3.13	3.96	4.90	5.93	7.04
$45^\circ-60^\circ$	$51.9^\circ$	-0.53	-0.45	-0.35	-0.33	-0.21	-0.05	0	0.17	0.39	0.68	1.02	1.43	1.90	2.46	3.08	3.77	4.52	5.31
$60^\circ-75^\circ$	$66.3^\circ$	-0.47	-0.39	-0.30	-0.29	-0.19	-0.04	0	0.13	0.34	0.59	0.88	1.24	1.65	2.13	2.68	3.29	3.96	4.67
$75^\circ-90^\circ$	$79.4^\circ$	-0.34	-0.34	-0.26	-0.25	-0.16	-0.04	0	0.11	0.29	0.50	0.75	1.04	1.37	1.74	2.18	2.65	3.15	3.67

Table A.3:  $\mathbf{F}_i$  ( $\text{Wm}^{-2}$ ) for  $\text{N}_2\text{O}$  as a function of latitude and concentrations. The average latitude ( $\text{Lat}_{avg}$ ) is the latitude at which there is an equal amount of area north and south within the segment.

$\text{Lat}_{range}$	$\text{Lat}_{avg}$	$\log_{10}(\text{N}_2\text{O concentration})$																
		-7.00	-6.80	-6.60	-6.57	-6.40	-6.20	-6.00	-5.80	-5.60	-5.40	-5.20	-5.00	-4.80	-4.60	-4.40	-4.20	-4.00
GAM	$30.0^\circ$	-0.77	-0.47	-0.07	0	0.44	1.09	1.90	2.89	4.09	5.51	7.18	9.12	11.32	13.80	16.49	19.35	22.29
$00^\circ-15^\circ$	$7.5^\circ$	-0.81	-0.49	-0.07	0	0.46	1.14	1.99	3.04	4.30	5.83	7.60	9.67	12.04	14.70	17.61	20.71	23.93
$15^\circ-30^\circ$	$22.3^\circ$	-0.92	-0.56	-0.09	0	0.52	1.29	2.25	3.41	4.81	6.47	8.41	10.66	13.21	16.07	19.18	22.45	25.83
$30^\circ-45^\circ$	$37.1^\circ$	-0.77	-0.47	-0.07	0	0.44	1.08	1.88	2.87	4.06	5.45	7.08	8.98	11.12	13.53	16.16	18.94	21.80
$45^\circ-60^\circ$	$51.9^\circ$	-0.65	-0.39	-0.06	0	0.38	0.94	1.63	2.49	3.53	4.76	6.20	7.88	9.80	11.95	14.30	16.78	19.30
$60^\circ-75^\circ$	$66.3^\circ$	-0.57	-0.35	-0.05	0	0.33	0.82	1.44	2.20	3.12	4.22	5.50	6.98	8.68	10.59	12.66	14.85	17.10
$75^\circ-90^\circ$	$79.4^\circ$	-0.54	-0.33	-0.05	0	0.32	0.79	1.40	2.15	3.06	4.16	5.43	6.91	8.60	10.49	12.54	14.67	16.86

## A.4 Early Earth Tables

This appendix contains the atmospheric profile for chapter 3. Atmospheric profiles for atmospheres with 0.5, 1 and 2 bar of N<sub>2</sub> are provided.

Table A.4: **Atmospheric structure for GAM**  
GAM Profile

P (Pa)	T (K)	H <sub>2</sub> O (ppv)	O <sub>3</sub> (ppv)
$1.00 \times 10^1$	$2.3090 \times 10^2$	$3.7110 \times 10^{-6}$	$2.7553 \times 10^{-6}$
$3.00 \times 10^1$	$2.5008 \times 10^2$	$4.0178 \times 10^{-6}$	$2.3885 \times 10^{-6}$
$4.00 \times 10^1$	$2.5487 \times 10^2$	$4.0519 \times 10^{-6}$	$2.6965 \times 10^{-6}$
$5.00 \times 10^1$	$2.5804 \times 10^2$	$4.0639 \times 10^{-6}$	$3.0663 \times 10^{-6}$
$7.00 \times 10^1$	$2.6180 \times 10^2$	$4.0593 \times 10^{-6}$	$3.8287 \times 10^{-6}$
$1.00 \times 10^2$	$2.6301 \times 10^2$	$4.0156 \times 10^{-6}$	$4.9232 \times 10^{-6}$
$2.00 \times 10^2$	$2.5762 \times 10^2$	$3.8528 \times 10^{-6}$	$8.1090 \times 10^{-6}$
$3.00 \times 10^2$	$2.4964 \times 10^2$	$3.7131 \times 10^{-6}$	$1.0585 \times 10^{-5}$
$4.00 \times 10^2$	$2.4346 \times 10^2$	$3.5825 \times 10^{-6}$	$1.2036 \times 10^{-5}$
$5.00 \times 10^2$	$2.3914 \times 10^2$	$3.4659 \times 10^{-6}$	$1.2842 \times 10^{-5}$
$7.00 \times 10^2$	$2.3357 \times 10^2$	$3.3177 \times 10^{-6}$	$1.3520 \times 10^{-5}$
$1.00 \times 10^3$	$2.2894 \times 10^2$	$3.1658 \times 10^{-6}$	$1.3540 \times 10^{-5}$
$2.00 \times 10^3$	$2.2158 \times 10^2$	$2.9343 \times 10^{-6}$	$1.0288 \times 10^{-5}$
$3.00 \times 10^3$	$2.1753 \times 10^2$	$2.8355 \times 10^{-6}$	$7.3036 \times 10^{-6}$
$4.00 \times 10^3$	$2.1447 \times 10^2$	$2.7575 \times 10^{-6}$	$5.0405 \times 10^{-6}$
$5.00 \times 10^3$	$2.1194 \times 10^2$	$2.6933 \times 10^{-6}$	$3.4087 \times 10^{-6}$
$7.00 \times 10^3$	$2.0754 \times 10^2$	$2.6063 \times 10^{-6}$	$1.6882 \times 10^{-6}$
$1.00 \times 10^4$	$2.0578 \times 10^2$	$2.7685 \times 10^{-6}$	$7.8225 \times 10^{-7}$
$1.50 \times 10^4$	$2.1176 \times 10^2$	$7.3212 \times 10^{-6}$	$3.9893 \times 10^{-7}$
$2.00 \times 10^4$	$2.1878 \times 10^2$	$2.8445 \times 10^{-5}$	$2.5456 \times 10^{-7}$
$2.50 \times 10^4$	$2.2618 \times 10^2$	$8.6150 \times 10^{-5}$	$1.5667 \times 10^{-7}$
$3.00 \times 10^4$	$2.3392 \times 10^2$	$1.8858 \times 10^{-4}$	$1.0867 \times 10^{-7}$
$3.50 \times 10^4$	$2.4134 \times 10^2$	$3.3540 \times 10^{-4}$	$9.0312 \times 10^{-8}$
$4.00 \times 10^4$	$2.4791 \times 10^2$	$5.1532 \times 10^{-4}$	$8.4024 \times 10^{-8}$
$4.50 \times 10^4$	$2.5381 \times 10^2$	$7.7878 \times 10^{-4}$	$8.0766 \times 10^{-8}$
$5.00 \times 10^4$	$2.5897 \times 10^2$	$1.1353 \times 10^{-3}$	$7.8163 \times 10^{-8}$
$5.50 \times 10^4$	$2.6355 \times 10^2$	$1.6339 \times 10^{-3}$	$7.5431 \times 10^{-8}$
$6.00 \times 10^4$	$2.6744 \times 10^2$	$2.1607 \times 10^{-3}$	$7.2923 \times 10^{-8}$
$6.50 \times 10^4$	$2.7083 \times 10^2$	$2.7393 \times 10^{-3}$	$7.0508 \times 10^{-8}$
$7.00 \times 10^4$	$2.7401 \times 10^2$	$3.3183 \times 10^{-3}$	$6.8145 \times 10^{-8}$
$7.25 \times 10^4$	$2.7559 \times 10^2$	$3.6496 \times 10^{-3}$	$6.6924 \times 10^{-8}$
$7.50 \times 10^4$	$2.7707 \times 10^2$	$3.9954 \times 10^{-3}$	$6.5661 \times 10^{-8}$
$7.75 \times 10^4$	$2.7846 \times 10^2$	$4.3507 \times 10^{-3}$	$6.4332 \times 10^{-8}$
$8.00 \times 10^4$	$2.7976 \times 10^2$	$4.7274 \times 10^{-3}$	$6.2873 \times 10^{-8}$
$8.25 \times 10^4$	$2.8092 \times 10^2$	$5.1375 \times 10^{-3}$	$6.1326 \times 10^{-8}$
$8.50 \times 10^4$	$2.8194 \times 10^2$	$5.6437 \times 10^{-3}$	$5.9634 \times 10^{-8}$
$8.75 \times 10^4$	$2.8281 \times 10^2$	$6.3038 \times 10^{-3}$	$5.7747 \times 10^{-8}$
$9.00 \times 10^4$	$2.8358 \times 10^2$	$7.1277 \times 10^{-3}$	$5.5706 \times 10^{-8}$
$9.25 \times 10^4$	$2.8447 \times 10^2$	$8.0097 \times 10^{-3}$	$5.3819 \times 10^{-8}$
$9.50 \times 10^4$	$2.8556 \times 10^2$	$8.7684 \times 10^{-3}$	$5.2366 \times 10^{-8}$
$9.75 \times 10^4$	$2.8677 \times 10^2$	$9.3820 \times 10^{-3}$	$5.1275 \times 10^{-8}$
$1.00 \times 10^5$	$2.8824 \times 10^2$	$9.9597 \times 10^{-3}$	$5.0847 \times 10^{-8}$

Table A.5: **Atmospheric structure for 00°-15°**  
 Profile 1: 00°-15°

P (Pa)	T (K)	H <sub>2</sub> O (ppv)	O <sub>3</sub> (ppv)
1.00×10 <sup>1</sup>	2.2473×10 <sup>2</sup>	3.9749×10 <sup>-6</sup>	2.6403×10 <sup>-6</sup>
3.00×10 <sup>1</sup>	2.4683×10 <sup>2</sup>	4.1505×10 <sup>-6</sup>	2.3688×10 <sup>-6</sup>
4.00×10 <sup>1</sup>	2.5322×10 <sup>2</sup>	4.1496×10 <sup>-6</sup>	2.6832×10 <sup>-6</sup>
5.00×10 <sup>1</sup>	2.5777×10 <sup>2</sup>	4.1338×10 <sup>-6</sup>	3.0594×10 <sup>-6</sup>
7.00×10 <sup>1</sup>	2.6343×10 <sup>2</sup>	4.0832×10 <sup>-6</sup>	3.8103×10 <sup>-6</sup>
1.00×10 <sup>2</sup>	2.6585×10 <sup>2</sup>	3.9798×10 <sup>-6</sup>	4.8414×10 <sup>-6</sup>
2.00×10 <sup>2</sup>	2.6068×10 <sup>2</sup>	3.6851×10 <sup>-6</sup>	8.0989×10 <sup>-6</sup>
3.00×10 <sup>2</sup>	2.5206×10 <sup>2</sup>	3.4721×10 <sup>-6</sup>	1.0952×10 <sup>-5</sup>
4.00×10 <sup>2</sup>	2.4539×10 <sup>2</sup>	3.2942×10 <sup>-6</sup>	1.2872×10 <sup>-5</sup>
5.00×10 <sup>2</sup>	2.4085×10 <sup>2</sup>	3.1530×10 <sup>-6</sup>	1.4166×10 <sup>-5</sup>
7.00×10 <sup>2</sup>	2.3522×10 <sup>2</sup>	2.9615×10 <sup>-6</sup>	1.5788×10 <sup>-5</sup>
1.00×10 <sup>3</sup>	2.3061×10 <sup>2</sup>	2.8017×10 <sup>-6</sup>	1.6653×10 <sup>-5</sup>
2.00×10 <sup>3</sup>	2.2192×10 <sup>2</sup>	2.6100×10 <sup>-6</sup>	1.1658×10 <sup>-5</sup>
3.00×10 <sup>3</sup>	2.1602×10 <sup>2</sup>	2.5379×10 <sup>-6</sup>	7.0050×10 <sup>-6</sup>
4.00×10 <sup>3</sup>	2.1121×10 <sup>2</sup>	2.4827×10 <sup>-6</sup>	3.9981×10 <sup>-6</sup>
5.00×10 <sup>3</sup>	2.0689×10 <sup>2</sup>	2.4352×10 <sup>-6</sup>	2.1497×10 <sup>-6</sup>
7.00×10 <sup>3</sup>	1.9838×10 <sup>2</sup>	2.3728×10 <sup>-6</sup>	6.6715×10 <sup>-7</sup>
1.00×10 <sup>4</sup>	1.9354×10 <sup>2</sup>	2.3116×10 <sup>-6</sup>	2.2943×10 <sup>-7</sup>
1.50×10 <sup>4</sup>	2.0517×10 <sup>2</sup>	1.0670×10 <sup>-5</sup>	1.0580×10 <sup>-7</sup>
2.00×10 <sup>4</sup>	2.1939×10 <sup>2</sup>	5.2553×10 <sup>-5</sup>	8.1277×10 <sup>-8</sup>
2.50×10 <sup>4</sup>	2.3192×10 <sup>2</sup>	1.6102×10 <sup>-4</sup>	7.5167×10 <sup>-8</sup>
3.00×10 <sup>4</sup>	2.4212×10 <sup>2</sup>	3.4968×10 <sup>-4</sup>	7.2805×10 <sup>-8</sup>
3.50×10 <sup>4</sup>	2.5054×10 <sup>2</sup>	6.2578×10 <sup>-4</sup>	7.1585×10 <sup>-8</sup>
4.00×10 <sup>4</sup>	2.5717×10 <sup>2</sup>	9.4776×10 <sup>-4</sup>	7.1313×10 <sup>-8</sup>
4.50×10 <sup>4</sup>	2.6294×10 <sup>2</sup>	1.4481×10 <sup>-3</sup>	7.0326×10 <sup>-8</sup>
5.00×10 <sup>4</sup>	2.6787×10 <sup>2</sup>	2.1532×10 <sup>-3</sup>	6.8519×10 <sup>-8</sup>
5.50×10 <sup>4</sup>	2.7230×10 <sup>2</sup>	3.1731×10 <sup>-3</sup>	6.5587×10 <sup>-8</sup>
6.00×10 <sup>4</sup>	2.7582×10 <sup>2</sup>	4.1177×10 <sup>-3</sup>	6.3359×10 <sup>-8</sup>
6.50×10 <sup>4</sup>	2.7878×10 <sup>2</sup>	5.0934×10 <sup>-3</sup>	6.1420×10 <sup>-8</sup>
7.00×10 <sup>4</sup>	2.8193×10 <sup>2</sup>	5.9541×10 <sup>-3</sup>	5.9773×10 <sup>-8</sup>
7.25×10 <sup>4</sup>	2.8359×10 <sup>2</sup>	6.4651×10 <sup>-3</sup>	5.8806×10 <sup>-8</sup>
7.50×10 <sup>4</sup>	2.8519×10 <sup>2</sup>	7.0027×10 <sup>-3</sup>	5.7736×10 <sup>-8</sup>
7.75×10 <sup>4</sup>	2.8671×10 <sup>2</sup>	7.5521×10 <sup>-3</sup>	5.6541×10 <sup>-8</sup>
8.00×10 <sup>4</sup>	2.8816×10 <sup>2</sup>	8.1485×10 <sup>-3</sup>	5.5103×10 <sup>-8</sup>
8.25×10 <sup>4</sup>	2.8946×10 <sup>2</sup>	8.7924×10 <sup>-3</sup>	5.3525×10 <sup>-8</sup>
8.50×10 <sup>4</sup>	2.9057×10 <sup>2</sup>	9.5997×10 <sup>-3</sup>	5.1716×10 <sup>-8</sup>
8.75×10 <sup>4</sup>	2.9153×10 <sup>2</sup>	1.0644×10 <sup>-2</sup>	4.9609×10 <sup>-8</sup>
9.00×10 <sup>4</sup>	2.9249×10 <sup>2</sup>	1.1892×10 <sup>-2</sup>	4.7369×10 <sup>-8</sup>
9.25×10 <sup>4</sup>	2.9359×10 <sup>2</sup>	1.3308×10 <sup>-2</sup>	4.5206×10 <sup>-8</sup>
9.50×10 <sup>4</sup>	2.9494×10 <sup>2</sup>	1.4487×10 <sup>-2</sup>	4.3633×10 <sup>-8</sup>
9.75×10 <sup>4</sup>	2.9655×10 <sup>2</sup>	1.5273×10 <sup>-2</sup>	4.2705×10 <sup>-8</sup>
1.00×10 <sup>5</sup>	2.9857×10 <sup>2</sup>	1.5909×10 <sup>-2</sup>	4.2144×10 <sup>-8</sup>

Table A.6: **Atmospheric structure for 15°-30°**  
Profile 2: 15°-30°

P (Pa)	T (K)	H <sub>2</sub> O (ppv)	O <sub>3</sub> (ppv)
1.00×10 <sup>1</sup>	2.2669×10 <sup>2</sup>	3.8990×10 <sup>-6</sup>	2.6498×10 <sup>-6</sup>
3.00×10 <sup>1</sup>	2.4736×10 <sup>2</sup>	4.1298×10 <sup>-6</sup>	2.4155×10 <sup>-6</sup>
4.00×10 <sup>1</sup>	2.5286×10 <sup>2</sup>	4.1352×10 <sup>-6</sup>	2.7455×10 <sup>-6</sup>
5.00×10 <sup>1</sup>	2.5663×10 <sup>2</sup>	4.1243×10 <sup>-6</sup>	3.1194×10 <sup>-6</sup>
7.00×10 <sup>1</sup>	2.6125×10 <sup>2</sup>	4.0852×10 <sup>-6</sup>	3.8481×10 <sup>-6</sup>
1.00×10 <sup>2</sup>	2.6348×10 <sup>2</sup>	4.0075×10 <sup>-6</sup>	4.8975×10 <sup>-6</sup>
2.00×10 <sup>2</sup>	2.5947×10 <sup>2</sup>	3.7913×10 <sup>-6</sup>	8.2126×10 <sup>-6</sup>
3.00×10 <sup>2</sup>	2.5123×10 <sup>2</sup>	3.6259×10 <sup>-6</sup>	1.0973×10 <sup>-5</sup>
4.00×10 <sup>2</sup>	2.4472×10 <sup>2</sup>	3.4767×10 <sup>-6</sup>	1.2719×10 <sup>-5</sup>
5.00×10 <sup>2</sup>	2.4027×10 <sup>2</sup>	3.3483×10 <sup>-6</sup>	1.3762×10 <sup>-5</sup>
7.00×10 <sup>2</sup>	2.3473×10 <sup>2</sup>	3.1842×10 <sup>-6</sup>	1.4766×10 <sup>-5</sup>
1.00×10 <sup>3</sup>	2.3024×10 <sup>2</sup>	3.0324×10 <sup>-6</sup>	1.4988×10 <sup>-5</sup>
2.00×10 <sup>3</sup>	2.2225×10 <sup>2</sup>	2.8241×10 <sup>-6</sup>	1.1133×10 <sup>-5</sup>
3.00×10 <sup>3</sup>	2.1727×10 <sup>2</sup>	2.7476×10 <sup>-6</sup>	7.5186×10 <sup>-6</sup>
4.00×10 <sup>3</sup>	2.1298×10 <sup>2</sup>	2.6872×10 <sup>-6</sup>	4.6424×10 <sup>-6</sup>
5.00×10 <sup>3</sup>	2.0897×10 <sup>2</sup>	2.6429×10 <sup>-6</sup>	2.6820×10 <sup>-6</sup>
7.00×10 <sup>3</sup>	2.0151×10 <sup>2</sup>	2.6162×10 <sup>-6</sup>	9.7400×10 <sup>-7</sup>
1.00×10 <sup>4</sup>	1.9840×10 <sup>2</sup>	2.8840×10 <sup>-6</sup>	3.6135×10 <sup>-7</sup>
1.50×10 <sup>4</sup>	2.0772×10 <sup>2</sup>	8.5104×10 <sup>-6</sup>	1.7538×10 <sup>-7</sup>
2.00×10 <sup>4</sup>	2.1925×10 <sup>2</sup>	3.6517×10 <sup>-5</sup>	1.1818×10 <sup>-7</sup>
2.50×10 <sup>4</sup>	2.2999×10 <sup>2</sup>	1.0660×10 <sup>-4</sup>	9.7739×10 <sup>-8</sup>
3.00×10 <sup>4</sup>	2.3925×10 <sup>2</sup>	2.2047×10 <sup>-4</sup>	8.9530×10 <sup>-8</sup>
3.50×10 <sup>4</sup>	2.4718×10 <sup>2</sup>	3.7444×10 <sup>-4</sup>	8.5678×10 <sup>-8</sup>
4.00×10 <sup>4</sup>	2.5396×10 <sup>2</sup>	5.5514×10 <sup>-4</sup>	8.3844×10 <sup>-8</sup>
4.50×10 <sup>4</sup>	2.5998×10 <sup>2</sup>	8.0182×10 <sup>-4</sup>	8.2337×10 <sup>-8</sup>
5.00×10 <sup>4</sup>	2.6525×10 <sup>2</sup>	1.1380×10 <sup>-3</sup>	8.0615×10 <sup>-8</sup>
5.50×10 <sup>4</sup>	2.6990×10 <sup>2</sup>	1.6346×10 <sup>-3</sup>	7.8356×10 <sup>-8</sup>
6.00×10 <sup>4</sup>	2.7388×10 <sup>2</sup>	2.2371×10 <sup>-3</sup>	7.5931×10 <sup>-8</sup>
6.50×10 <sup>4</sup>	2.7735×10 <sup>2</sup>	2.9339×10 <sup>-3</sup>	7.3475×10 <sup>-8</sup>
7.00×10 <sup>4</sup>	2.8059×10 <sup>2</sup>	3.6598×10 <sup>-3</sup>	7.1036×10 <sup>-8</sup>
7.25×10 <sup>4</sup>	2.8218×10 <sup>2</sup>	4.0699×10 <sup>-3</sup>	6.9746×10 <sup>-8</sup>
7.50×10 <sup>4</sup>	2.8370×10 <sup>2</sup>	4.4979×10 <sup>-3</sup>	6.8404×10 <sup>-8</sup>
7.75×10 <sup>4</sup>	2.8513×10 <sup>2</sup>	4.9345×10 <sup>-3</sup>	6.6982×10 <sup>-8</sup>
8.00×10 <sup>4</sup>	2.8648×10 <sup>2</sup>	5.3903×10 <sup>-3</sup>	6.5396×10 <sup>-8</sup>
8.25×10 <sup>4</sup>	2.8769×10 <sup>2</sup>	5.8963×10 <sup>-3</sup>	6.3665×10 <sup>-8</sup>
8.50×10 <sup>4</sup>	2.8872×10 <sup>2</sup>	6.5524×10 <sup>-3</sup>	6.1678×10 <sup>-8</sup>
8.75×10 <sup>4</sup>	2.8956×10 <sup>2</sup>	7.4439×10 <sup>-3</sup>	5.9350×10 <sup>-8</sup>
9.00×10 <sup>4</sup>	2.9025×10 <sup>2</sup>	8.5749×10 <sup>-3</sup>	5.6777×10 <sup>-8</sup>
9.25×10 <sup>4</sup>	2.9117×10 <sup>2</sup>	9.7319×10 <sup>-3</sup>	5.4511×10 <sup>-8</sup>
9.50×10 <sup>4</sup>	2.9229×10 <sup>2</sup>	1.0775×10 <sup>-2</sup>	5.2791×10 <sup>-8</sup>
9.75×10 <sup>4</sup>	2.9341×10 <sup>2</sup>	1.1786×10 <sup>-2</sup>	5.1447×10 <sup>-8</sup>
1.00×10 <sup>5</sup>	2.9494×10 <sup>2</sup>	1.2728×10 <sup>-2</sup>	5.0534×10 <sup>-8</sup>

Table A.7: **Atmospheric structure for 30°-45°**  
Profile 3: 30°-45°

P (Pa)	T (K)	H <sub>2</sub> O (ppv)	O <sub>3</sub> (ppv)
1.00×10 <sup>1</sup>	2.2892×10 <sup>2</sup>	3.7054×10 <sup>-6</sup>	2.5940×10 <sup>-6</sup>
3.00×10 <sup>1</sup>	2.4810×10 <sup>2</sup>	4.0556×10 <sup>-6</sup>	2.4181×10 <sup>-6</sup>
4.00×10 <sup>1</sup>	2.5292×10 <sup>2</sup>	4.0885×10 <sup>-6</sup>	2.7497×10 <sup>-6</sup>
5.00×10 <sup>1</sup>	2.5602×10 <sup>2</sup>	4.0974×10 <sup>-6</sup>	3.1201×10 <sup>-6</sup>
7.00×10 <sup>1</sup>	2.5968×10 <sup>2</sup>	4.0898×10 <sup>-6</sup>	3.8853×10 <sup>-6</sup>
1.00×10 <sup>2</sup>	2.6115×10 <sup>2</sup>	4.0499×10 <sup>-6</sup>	5.0419×10 <sup>-6</sup>
2.00×10 <sup>2</sup>	2.5674×10 <sup>2</sup>	3.9095×10 <sup>-6</sup>	8.4087×10 <sup>-6</sup>
3.00×10 <sup>2</sup>	2.4933×10 <sup>2</sup>	3.7861×10 <sup>-6</sup>	1.0892×10 <sup>-5</sup>
4.00×10 <sup>2</sup>	2.4343×10 <sup>2</sup>	3.6677×10 <sup>-6</sup>	1.2258×10 <sup>-5</sup>
5.00×10 <sup>2</sup>	2.3918×10 <sup>2</sup>	3.5565×10 <sup>-6</sup>	1.2930×10 <sup>-5</sup>
7.00×10 <sup>2</sup>	2.3354×10 <sup>2</sup>	3.4255×10 <sup>-6</sup>	1.3295×10 <sup>-5</sup>
1.00×10 <sup>3</sup>	2.2891×10 <sup>2</sup>	3.2857×10 <sup>-6</sup>	1.2995×10 <sup>-5</sup>
2.00×10 <sup>3</sup>	2.2212×10 <sup>2</sup>	3.0501×10 <sup>-6</sup>	1.0231×10 <sup>-5</sup>
3.00×10 <sup>3</sup>	2.1853×10 <sup>2</sup>	2.9586×10 <sup>-6</sup>	7.6823×10 <sup>-6</sup>
4.00×10 <sup>3</sup>	2.1579×10 <sup>2</sup>	2.8767×10 <sup>-6</sup>	5.5319×10 <sup>-6</sup>
5.00×10 <sup>3</sup>	2.1370×10 <sup>2</sup>	2.8083×10 <sup>-6</sup>	3.8559×10 <sup>-6</sup>
7.00×10 <sup>3</sup>	2.1076×10 <sup>2</sup>	2.7082×10 <sup>-6</sup>	1.9298×10 <sup>-6</sup>
1.00×10 <sup>4</sup>	2.1008×10 <sup>2</sup>	3.0409×10 <sup>-6</sup>	8.5325×10 <sup>-7</sup>
1.50×10 <sup>4</sup>	2.1407×10 <sup>2</sup>	6.2131×10 <sup>-6</sup>	4.5498×10 <sup>-7</sup>
2.00×10 <sup>4</sup>	2.1800×10 <sup>2</sup>	1.9561×10 <sup>-5</sup>	2.7692×10 <sup>-7</sup>
2.50×10 <sup>4</sup>	2.2410×10 <sup>2</sup>	6.1011×10 <sup>-5</sup>	1.6472×10 <sup>-7</sup>
3.00×10 <sup>4</sup>	2.3171×10 <sup>2</sup>	1.3825×10 <sup>-4</sup>	1.1721×10 <sup>-7</sup>
3.50×10 <sup>4</sup>	2.3918×10 <sup>2</sup>	2.4593×10 <sup>-4</sup>	9.8844×10 <sup>-8</sup>
4.00×10 <sup>4</sup>	2.4598×10 <sup>2</sup>	3.9039×10 <sup>-4</sup>	9.1354×10 <sup>-8</sup>
4.50×10 <sup>4</sup>	2.5212×10 <sup>2</sup>	5.9185×10 <sup>-4</sup>	8.7295×10 <sup>-8</sup>
5.00×10 <sup>4</sup>	2.5754×10 <sup>2</sup>	8.4418×10 <sup>-4</sup>	8.4318×10 <sup>-8</sup>
5.50×10 <sup>4</sup>	2.6233×10 <sup>2</sup>	1.1571×10 <sup>-3</sup>	8.1649×10 <sup>-8</sup>
6.00×10 <sup>4</sup>	2.6654×10 <sup>2</sup>	1.5330×10 <sup>-3</sup>	7.9062×10 <sup>-8</sup>
6.50×10 <sup>4</sup>	2.7028×10 <sup>2</sup>	1.9677×10 <sup>-3</sup>	7.6517×10 <sup>-8</sup>
7.00×10 <sup>4</sup>	2.7353×10 <sup>2</sup>	2.4515×10 <sup>-3</sup>	7.3929×10 <sup>-8</sup>
7.25×10 <sup>4</sup>	2.7507×10 <sup>2</sup>	2.7196×10 <sup>-3</sup>	7.2599×10 <sup>-8</sup>
7.50×10 <sup>4</sup>	2.7650×10 <sup>2</sup>	2.9945×10 <sup>-3</sup>	7.1245×10 <sup>-8</sup>
7.75×10 <sup>4</sup>	2.7783×10 <sup>2</sup>	3.2840×10 <sup>-3</sup>	6.9830×10 <sup>-8</sup>
8.00×10 <sup>4</sup>	2.7906×10 <sup>2</sup>	3.5898×10 <sup>-3</sup>	6.8321×10 <sup>-8</sup>
8.25×10 <sup>4</sup>	2.8015×10 <sup>2</sup>	3.9278×10 <sup>-3</sup>	6.6722×10 <sup>-8</sup>
8.50×10 <sup>4</sup>	2.8113×10 <sup>2</sup>	4.3376×10 <sup>-3</sup>	6.4971×10 <sup>-8</sup>
8.75×10 <sup>4</sup>	2.8193×10 <sup>2</sup>	4.8859×10 <sup>-3</sup>	6.2975×10 <sup>-8</sup>
9.00×10 <sup>4</sup>	2.8260×10 <sup>2</sup>	5.6478×10 <sup>-3</sup>	6.0742×10 <sup>-8</sup>
9.25×10 <sup>4</sup>	2.8343×10 <sup>2</sup>	6.4520×10 <sup>-3</sup>	5.8710×10 <sup>-8</sup>
9.50×10 <sup>4</sup>	2.8457×10 <sup>2</sup>	7.1352×10 <sup>-3</sup>	5.7165×10 <sup>-8</sup>
9.75×10 <sup>4</sup>	2.8595×10 <sup>2</sup>	7.6986×10 <sup>-3</sup>	5.6016×10 <sup>-8</sup>
1.00×10 <sup>5</sup>	2.8729×10 <sup>2</sup>	8.2899×10 <sup>-3</sup>	5.4962×10 <sup>-8</sup>

Table A.8: **Atmospheric structure for 45°-60°**  
Profile 4: 45°-60°

P (Pa)	T (K)	H <sub>2</sub> O (ppv)	O <sub>3</sub> (ppv)
1.00×10 <sup>1</sup>	2.3568×10 <sup>2</sup>	3.4474×10 <sup>-6</sup>	2.6523×10 <sup>-6</sup>
3.00×10 <sup>1</sup>	2.5201×10 <sup>2</sup>	3.8811×10 <sup>-6</sup>	2.3065×10 <sup>-6</sup>
4.00×10 <sup>1</sup>	2.5569×10 <sup>2</sup>	3.9569×10 <sup>-6</sup>	2.6372×10 <sup>-6</sup>
5.00×10 <sup>1</sup>	2.5795×10 <sup>2</sup>	4.0013×10 <sup>-6</sup>	3.0315×10 <sup>-6</sup>
7.00×10 <sup>1</sup>	2.6037×10 <sup>2</sup>	4.0460×10 <sup>-6</sup>	3.8847×10 <sup>-6</sup>
1.00×10 <sup>2</sup>	2.6034×10 <sup>2</sup>	4.0582×10 <sup>-6</sup>	5.1021×10 <sup>-6</sup>
2.00×10 <sup>2</sup>	2.5392×10 <sup>2</sup>	4.0051×10 <sup>-6</sup>	8.2281×10 <sup>-6</sup>
3.00×10 <sup>2</sup>	2.4663×10 <sup>2</sup>	3.9229×10 <sup>-6</sup>	1.0343×10 <sup>-5</sup>
4.00×10 <sup>2</sup>	2.4101×10 <sup>2</sup>	3.8283×10 <sup>-6</sup>	1.1339×10 <sup>-5</sup>
5.00×10 <sup>2</sup>	2.3694×10 <sup>2</sup>	3.7297×10 <sup>-6</sup>	1.1714×10 <sup>-5</sup>
7.00×10 <sup>2</sup>	2.3151×10 <sup>2</sup>	3.6093×10 <sup>-6</sup>	1.1634×10 <sup>-5</sup>
1.00×10 <sup>3</sup>	2.2701×10 <sup>2</sup>	3.4749×10 <sup>-6</sup>	1.1015×10 <sup>-5</sup>
2.00×10 <sup>3</sup>	2.2142×10 <sup>2</sup>	3.2148×10 <sup>-6</sup>	9.2256×10 <sup>-6</sup>
3.00×10 <sup>3</sup>	2.1932×10 <sup>2</sup>	3.0898×10 <sup>-6</sup>	7.6165×10 <sup>-6</sup>
4.00×10 <sup>3</sup>	2.1819×10 <sup>2</sup>	2.9871×10 <sup>-6</sup>	6.1374×10 <sup>-6</sup>
5.00×10 <sup>3</sup>	2.1766×10 <sup>2</sup>	2.8996×10 <sup>-6</sup>	4.7784×10 <sup>-6</sup>
7.00×10 <sup>3</sup>	2.1723×10 <sup>2</sup>	2.7529×10 <sup>-6</sup>	2.8511×10 <sup>-6</sup>
1.00×10 <sup>4</sup>	2.1763×10 <sup>2</sup>	2.9367×10 <sup>-6</sup>	1.4372×10 <sup>-6</sup>
1.50×10 <sup>4</sup>	2.1894×10 <sup>2</sup>	4.5446×10 <sup>-6</sup>	7.4896×10 <sup>-7</sup>
2.00×10 <sup>4</sup>	2.1865×10 <sup>2</sup>	8.9411×10 <sup>-6</sup>	4.6507×10 <sup>-7</sup>
2.50×10 <sup>4</sup>	2.2006×10 <sup>2</sup>	2.8891×10 <sup>-5</sup>	2.4683×10 <sup>-7</sup>
3.00×10 <sup>4</sup>	2.2498×10 <sup>2</sup>	7.3723×10 <sup>-5</sup>	1.4313×10 <sup>-7</sup>
3.50×10 <sup>4</sup>	2.3131×10 <sup>2</sup>	1.4236×10 <sup>-4</sup>	1.0457×10 <sup>-7</sup>
4.00×10 <sup>4</sup>	2.3768×10 <sup>2</sup>	2.4075×10 <sup>-4</sup>	9.1628×10 <sup>-8</sup>
4.50×10 <sup>4</sup>	2.4360×10 <sup>2</sup>	3.8097×10 <sup>-4</sup>	8.5837×10 <sup>-8</sup>
5.00×10 <sup>4</sup>	2.4886×10 <sup>2</sup>	5.5527×10 <sup>-4</sup>	8.2208×10 <sup>-8</sup>
5.50×10 <sup>4</sup>	2.5352×10 <sup>2</sup>	7.7058×10 <sup>-4</sup>	7.9277×10 <sup>-8</sup>
6.00×10 <sup>4</sup>	2.5762×10 <sup>2</sup>	1.0260×10 <sup>-3</sup>	7.6502×10 <sup>-8</sup>
6.50×10 <sup>4</sup>	2.6123×10 <sup>2</sup>	1.3177×10 <sup>-3</sup>	7.3722×10 <sup>-8</sup>
7.00×10 <sup>4</sup>	2.6432×10 <sup>2</sup>	1.6626×10 <sup>-3</sup>	7.0780×10 <sup>-8</sup>
7.25×10 <sup>4</sup>	2.6582×10 <sup>2</sup>	1.8515×10 <sup>-3</sup>	6.9331×10 <sup>-8</sup>
7.50×10 <sup>4</sup>	2.6720×10 <sup>2</sup>	2.0479×10 <sup>-3</sup>	6.7880×10 <sup>-8</sup>
7.75×10 <sup>4</sup>	2.6848×10 <sup>2</sup>	2.2520×10 <sup>-3</sup>	6.6425×10 <sup>-8</sup>
8.00×10 <sup>4</sup>	2.6968×10 <sup>2</sup>	2.4640×10 <sup>-3</sup>	6.4958×10 <sup>-8</sup>
8.25×10 <sup>4</sup>	2.7078×10 <sup>2</sup>	2.6885×10 <sup>-3</sup>	6.3498×10 <sup>-8</sup>
8.50×10 <sup>4</sup>	2.7182×10 <sup>2</sup>	2.9311×10 <sup>-3</sup>	6.2061×10 <sup>-8</sup>
8.75×10 <sup>4</sup>	2.7278×10 <sup>2</sup>	3.2118×10 <sup>-3</sup>	6.0627×10 <sup>-8</sup>
9.00×10 <sup>4</sup>	2.7367×10 <sup>2</sup>	3.5516×10 <sup>-3</sup>	5.9183×10 <sup>-8</sup>
9.25×10 <sup>4</sup>	2.7460×10 <sup>2</sup>	3.8990×10 <sup>-3</sup>	5.7837×10 <sup>-8</sup>
9.50×10 <sup>4</sup>	2.7570×10 <sup>2</sup>	4.2011×10 <sup>-3</sup>	5.6703×10 <sup>-8</sup>
9.75×10 <sup>4</sup>	2.7689×10 <sup>2</sup>	4.4613×10 <sup>-3</sup>	5.5690×10 <sup>-8</sup>
1.00×10 <sup>5</sup>	2.7778×10 <sup>2</sup>	4.6728×10 <sup>-3</sup>	5.4387×10 <sup>-8</sup>

Table A.9: **Atmospheric structure for 60°-75°**  
Profile 5: 60°-75°

P (Pa)	T (K)	H <sub>2</sub> O (ppv)	O <sub>3</sub> (ppv)
1.00×10 <sup>1</sup>	2.4389×10 <sup>2</sup>	3.2390×10 <sup>-6</sup>	3.0354×10 <sup>-6</sup>
3.00×10 <sup>1</sup>	2.6017×10 <sup>2</sup>	3.7047×10 <sup>-6</sup>	2.2816×10 <sup>-6</sup>
4.00×10 <sup>1</sup>	2.6246×10 <sup>2</sup>	3.8046×10 <sup>-6</sup>	2.5369×10 <sup>-6</sup>
5.00×10 <sup>1</sup>	2.6347×10 <sup>2</sup>	3.8731×10 <sup>-6</sup>	2.8982×10 <sup>-6</sup>
7.00×10 <sup>1</sup>	2.6405×10 <sup>2</sup>	3.9577×10 <sup>-6</sup>	3.6888×10 <sup>-6</sup>
1.00×10 <sup>2</sup>	2.6223×10 <sup>2</sup>	4.0114×10 <sup>-6</sup>	4.7915×10 <sup>-6</sup>
2.00×10 <sup>2</sup>	2.5364×10 <sup>2</sup>	4.0257×10 <sup>-6</sup>	7.4710×10 <sup>-6</sup>
3.00×10 <sup>2</sup>	2.4584×10 <sup>2</sup>	3.9770×10 <sup>-6</sup>	9.2046×10 <sup>-6</sup>
4.00×10 <sup>2</sup>	2.4026×10 <sup>2</sup>	3.9047×10 <sup>-6</sup>	9.9359×10 <sup>-6</sup>
5.00×10 <sup>2</sup>	2.3625×10 <sup>2</sup>	3.8234×10 <sup>-6</sup>	1.0124×10 <sup>-5</sup>
7.00×10 <sup>2</sup>	2.3074×10 <sup>2</sup>	3.7215×10 <sup>-6</sup>	9.8060×10 <sup>-6</sup>
1.00×10 <sup>3</sup>	2.2582×10 <sup>2</sup>	3.5657×10 <sup>-6</sup>	9.0837×10 <sup>-6</sup>
2.00×10 <sup>3</sup>	2.1955×10 <sup>2</sup>	3.2700×10 <sup>-6</sup>	7.7603×10 <sup>-6</sup>
3.00×10 <sup>3</sup>	2.1776×10 <sup>2</sup>	3.1055×10 <sup>-6</sup>	6.7579×10 <sup>-6</sup>
4.00×10 <sup>3</sup>	2.1717×10 <sup>2</sup>	2.9863×10 <sup>-6</sup>	5.8424×10 <sup>-6</sup>
5.00×10 <sup>3</sup>	2.1708×10 <sup>2</sup>	2.8875×10 <sup>-6</sup>	4.8875×10 <sup>-6</sup>
7.00×10 <sup>3</sup>	2.1696×10 <sup>2</sup>	2.7309×10 <sup>-6</sup>	3.1889×10 <sup>-6</sup>
1.00×10 <sup>4</sup>	2.1737×10 <sup>2</sup>	2.8500×10 <sup>-6</sup>	1.7107×10 <sup>-6</sup>
1.50×10 <sup>4</sup>	2.1851×10 <sup>2</sup>	3.7953×10 <sup>-6</sup>	8.6146×10 <sup>-7</sup>
2.00×10 <sup>4</sup>	2.1836×10 <sup>2</sup>	4.4630×10 <sup>-6</sup>	5.4578×10 <sup>-7</sup>
2.50×10 <sup>4</sup>	2.1757×10 <sup>2</sup>	1.2895×10 <sup>-5</sup>	2.9491×10 <sup>-7</sup>
3.00×10 <sup>4</sup>	2.2011×10 <sup>2</sup>	3.7679×10 <sup>-5</sup>	1.5646×10 <sup>-7</sup>
3.50×10 <sup>4</sup>	2.2535×10 <sup>2</sup>	7.8834×10 <sup>-5</sup>	1.0481×10 <sup>-7</sup>
4.00×10 <sup>4</sup>	2.3132×10 <sup>2</sup>	1.4012×10 <sup>-4</sup>	8.9142×10 <sup>-8</sup>
4.50×10 <sup>4</sup>	2.3698×10 <sup>2</sup>	2.2638×10 <sup>-4</sup>	8.2669×10 <sup>-8</sup>
5.00×10 <sup>4</sup>	2.4204×10 <sup>2</sup>	3.3362×10 <sup>-4</sup>	7.8786×10 <sup>-8</sup>
5.50×10 <sup>4</sup>	2.4653×10 <sup>2</sup>	4.6519×10 <sup>-4</sup>	7.5741×10 <sup>-8</sup>
6.00×10 <sup>4</sup>	2.5044×10 <sup>2</sup>	6.2036×10 <sup>-4</sup>	7.2923×10 <sup>-8</sup>
6.50×10 <sup>4</sup>	2.5384×10 <sup>2</sup>	8.0009×10 <sup>-4</sup>	7.0207×10 <sup>-8</sup>
7.00×10 <sup>4</sup>	2.5692×10 <sup>2</sup>	1.0191×10 <sup>-3</sup>	6.7498×10 <sup>-8</sup>
7.25×10 <sup>4</sup>	2.5843×10 <sup>2</sup>	1.1415×10 <sup>-3</sup>	6.6221×10 <sup>-8</sup>
7.50×10 <sup>4</sup>	2.5982×10 <sup>2</sup>	1.2706×10 <sup>-3</sup>	6.4964×10 <sup>-8</sup>
7.75×10 <sup>4</sup>	2.6107×10 <sup>2</sup>	1.4039×10 <sup>-3</sup>	6.3713×10 <sup>-8</sup>
8.00×10 <sup>4</sup>	2.6217×10 <sup>2</sup>	1.5390×10 <sup>-3</sup>	6.2476×10 <sup>-8</sup>
8.25×10 <sup>4</sup>	2.6315×10 <sup>2</sup>	1.6774×10 <sup>-3</sup>	6.1257×10 <sup>-8</sup>
8.50×10 <sup>4</sup>	2.6402×10 <sup>2</sup>	1.8167×10 <sup>-3</sup>	6.0086×10 <sup>-8</sup>
8.75×10 <sup>4</sup>	2.6477×10 <sup>2</sup>	1.9620×10 <sup>-3</sup>	5.8949×10 <sup>-8</sup>
9.00×10 <sup>4</sup>	2.6538×10 <sup>2</sup>	2.1096×10 <sup>-3</sup>	5.7846×10 <sup>-8</sup>
9.25×10 <sup>4</sup>	2.6593×10 <sup>2</sup>	2.2466×10 <sup>-3</sup>	5.6824×10 <sup>-8</sup>
9.50×10 <sup>4</sup>	2.6647×10 <sup>2</sup>	2.3618×10 <sup>-3</sup>	5.5938×10 <sup>-8</sup>
9.75×10 <sup>4</sup>	2.6692×10 <sup>2</sup>	2.4443×10 <sup>-3</sup>	5.5085×10 <sup>-8</sup>
1.00×10 <sup>5</sup>	2.6784×10 <sup>2</sup>	2.6762×10 <sup>-3</sup>	5.7871×10 <sup>-8</sup>

Table A.10: **Atmospheric structure for 75°-90°**  
 Profile 6: 75°-90°

P (Pa)	T (K)	H <sub>2</sub> O (ppv)	O <sub>3</sub> (ppv)
1.00×10 <sup>1</sup>	2.4988×10 <sup>2</sup>	3.0227×10 <sup>-6</sup>	5.0140×10 <sup>-6</sup>
3.00×10 <sup>1</sup>	2.6359×10 <sup>2</sup>	3.5428×10 <sup>-6</sup>	2.8630×10 <sup>-6</sup>
4.00×10 <sup>1</sup>	2.6519×10 <sup>2</sup>	3.6650×10 <sup>-6</sup>	2.8716×10 <sup>-6</sup>
5.00×10 <sup>1</sup>	2.6574×10 <sup>2</sup>	3.7529×10 <sup>-6</sup>	3.0704×10 <sup>-6</sup>
7.00×10 <sup>1</sup>	2.6581×10 <sup>2</sup>	3.8675×10 <sup>-6</sup>	3.6366×10 <sup>-6</sup>
1.00×10 <sup>2</sup>	2.6358×10 <sup>2</sup>	3.9501×10 <sup>-6</sup>	4.5580×10 <sup>-6</sup>
2.00×10 <sup>2</sup>	2.5425×10 <sup>2</sup>	3.9988×10 <sup>-6</sup>	6.9461×10 <sup>-6</sup>
3.00×10 <sup>2</sup>	2.4595×10 <sup>2</sup>	3.9655×10 <sup>-6</sup>	8.3735×10 <sup>-6</sup>
4.00×10 <sup>2</sup>	2.4030×10 <sup>2</sup>	3.9113×10 <sup>-6</sup>	8.9009×10 <sup>-6</sup>
5.00×10 <sup>2</sup>	2.3623×10 <sup>2</sup>	3.8460×10 <sup>-6</sup>	8.9655×10 <sup>-6</sup>
7.00×10 <sup>2</sup>	2.3046×10 <sup>2</sup>	3.7683×10 <sup>-6</sup>	8.5396×10 <sup>-6</sup>
1.00×10 <sup>3</sup>	2.2492×10 <sup>2</sup>	3.5324×10 <sup>-6</sup>	7.8000×10 <sup>-6</sup>
2.00×10 <sup>3</sup>	2.1742×10 <sup>2</sup>	3.1816×10 <sup>-6</sup>	6.6161×10 <sup>-6</sup>
3.00×10 <sup>3</sup>	2.1559×10 <sup>2</sup>	2.9932×10 <sup>-6</sup>	5.8879×10 <sup>-6</sup>
4.00×10 <sup>3</sup>	2.1519×10 <sup>2</sup>	2.8762×10 <sup>-6</sup>	5.3236×10 <sup>-6</sup>
5.00×10 <sup>3</sup>	2.1524×10 <sup>2</sup>	2.7786×10 <sup>-6</sup>	4.6731×10 <sup>-6</sup>
7.00×10 <sup>3</sup>	2.1505×10 <sup>2</sup>	2.6394×10 <sup>-6</sup>	3.2077×10 <sup>-6</sup>
1.00×10 <sup>4</sup>	2.1547×10 <sup>2</sup>	2.7414×10 <sup>-6</sup>	1.7524×10 <sup>-6</sup>
1.50×10 <sup>4</sup>	2.1683×10 <sup>2</sup>	3.4915×10 <sup>-6</sup>	8.7861×10 <sup>-7</sup>
2.00×10 <sup>4</sup>	2.1724×10 <sup>2</sup>	3.4818×10 <sup>-6</sup>	5.6442×10 <sup>-7</sup>
2.50×10 <sup>4</sup>	2.1610×10 <sup>2</sup>	7.3388×10 <sup>-6</sup>	3.1805×10 <sup>-7</sup>
3.00×10 <sup>4</sup>	2.1725×10 <sup>2</sup>	2.3089×10 <sup>-5</sup>	1.6385×10 <sup>-7</sup>
3.50×10 <sup>4</sup>	2.2159×10 <sup>2</sup>	4.9887×10 <sup>-5</sup>	1.0451×10 <sup>-7</sup>
4.00×10 <sup>4</sup>	2.2708×10 <sup>2</sup>	8.8595×10 <sup>-5</sup>	8.6832×10 <sup>-8</sup>
4.50×10 <sup>4</sup>	2.3240×10 <sup>2</sup>	1.4279×10 <sup>-4</sup>	8.0024×10 <sup>-8</sup>
5.00×10 <sup>4</sup>	2.3721×10 <sup>2</sup>	2.0957×10 <sup>-4</sup>	7.5958×10 <sup>-8</sup>
5.50×10 <sup>4</sup>	2.4143×10 <sup>2</sup>	2.8866×10 <sup>-4</sup>	7.2868×10 <sup>-8</sup>
6.00×10 <sup>4</sup>	2.4497×10 <sup>2</sup>	3.7849×10 <sup>-4</sup>	7.0274×10 <sup>-8</sup>
6.50×10 <sup>4</sup>	2.4849×10 <sup>2</sup>	4.8751×10 <sup>-4</sup>	6.7913×10 <sup>-8</sup>
7.00×10 <sup>4</sup>	2.5151×10 <sup>2</sup>	6.1047×10 <sup>-4</sup>	6.5740×10 <sup>-8</sup>
7.25×10 <sup>4</sup>	2.5319×10 <sup>2</sup>	6.8093×10 <sup>-4</sup>	6.4957×10 <sup>-8</sup>
7.50×10 <sup>4</sup>	2.5464×10 <sup>2</sup>	7.5008×10 <sup>-4</sup>	6.4193×10 <sup>-8</sup>
7.75×10 <sup>4</sup>	2.5579×10 <sup>2</sup>	8.1302×10 <sup>-4</sup>	6.3391×10 <sup>-8</sup>
8.00×10 <sup>4</sup>	2.5671×10 <sup>2</sup>	8.6904×10 <sup>-4</sup>	6.2362×10 <sup>-8</sup>
8.25×10 <sup>4</sup>	2.5752×10 <sup>2</sup>	9.2264×10 <sup>-4</sup>	6.1304×10 <sup>-8</sup>
8.50×10 <sup>4</sup>	2.5817×10 <sup>2</sup>	9.7368×10 <sup>-4</sup>	6.0224×10 <sup>-8</sup>
8.75×10 <sup>4</sup>	2.5870×10 <sup>2</sup>	1.0368×10 <sup>-3</sup>	5.9468×10 <sup>-8</sup>
9.00×10 <sup>4</sup>	2.5887×10 <sup>2</sup>	1.0832×10 <sup>-3</sup>	5.8341×10 <sup>-8</sup>
9.25×10 <sup>4</sup>	2.5863×10 <sup>2</sup>	1.1150×10 <sup>-3</sup>	5.7077×10 <sup>-8</sup>
9.50×10 <sup>4</sup>	2.5799×10 <sup>2</sup>	1.1357×10 <sup>-3</sup>	5.5826×10 <sup>-8</sup>
9.75×10 <sup>4</sup>	2.5666×10 <sup>2</sup>	1.1425×10 <sup>-3</sup>	5.4580×10 <sup>-8</sup>
1.00×10 <sup>5</sup>	2.5750×10 <sup>2</sup>	1.3374×10 <sup>-3</sup>	5.7036×10 <sup>-8</sup>

Table A.11: **Cloud climatology for GAM Profile**  
GAM Profile

P (Pa)	tau	fraction
$2.50 \times 10^4$	$4.50 \times 10^{-1}$	$2.243 \times 10^{-1}$
$6.00 \times 10^4$	8.56	$2.1260 \times 10^{-1}$
$8.00 \times 10^4$	6.11	$4.1670 \times 10^{-1}$

Table A.12: **Cloud climatology for 00°-15°**  
Profile 1: 00°-15°

P (Pa)	tau	fraction
$2.50 \times 10^4$	$6.43 \times 10^{-1}$	$2.753 \times 10^{-1}$
$5.50 \times 10^4$	4.97	$1.842 \times 10^{-1}$
$8.00 \times 10^4$	4.90	$3.314 \times 10^{-1}$

Table A.13: **Cloud climatology for 15°-30°**  
Profile 2: 15°-30°

P (Pa)	tau	fraction
$2.50 \times 10^4$	$3.69 \times 10^{-1}$	$2.107 \times 10^{-1}$
$6.00 \times 10^4$	6.53	$1.466 \times 10^{-1}$
$8.25 \times 10^4$	4.47	$3.758 \times 10^{-1}$

Table A.14: **Cloud climatology for 30°-45°**  
Profile 3: 30°-45°

P (Pa)	tau	fraction
$2.50 \times 10^4$	$3.93 \times 10^{-1}$	$2.186 \times 10^{-1}$
$5.50 \times 10^4$	7.05	$2.253 \times 10^{-1}$
$8.00 \times 10^4$	4.89	$4.691 \times 10^{-1}$

Table A.15: **Cloud climatology for 45°-60°**  
Profile 4: 45°-60°

P (Pa)	tau	fraction
$2.50 \times 10^4$	$3.07 \times 10^{-1}$	$1.919 \times 10^{-1}$
$5.50 \times 10^4$	8.48	$3.376 \times 10^{-1}$
$8.00 \times 10^4$	6.90	$5.432 \times 10^{-1}$

Table A.16: **Cloud climatology for 60°-75°**  
Profile 5: 60°-75°

P (Pa)	tau	fraction
$2.50 \times 10^4$	$2.53 \times 10^{-1}$	$1.841 \times 10^{-1}$
$5.50 \times 10^4$	9.48	$3.646 \times 10^{-1}$
$8.00 \times 10^4$	13.4	$5.202 \times 10^{-1}$

Table A.17: **Cloud climatology for 75°-90°**

Profile 6: 75°-90°

P (Pa)	tau	fraction
$3.00 \times 10^4$	$1.59 \times 10^{-1}$	$1.841 \times 10^{-1}$
$5.50 \times 10^4$	14.3	$3.646 \times 10^{-1}$
$8.00 \times 10^4$	21.7	$5.202 \times 10^{-1}$

Table A.18: **Atmospheric structure for 0.5 bar of N<sub>2</sub>**  
 GAM Profile

P (Pa)	T (K)	H <sub>2</sub> O (mass fraction)	N <sub>2</sub> (mass fraction)
$5.0249 \times 10^0$	$2.0300 \times 10^2$	$7.8796 \times 10^{-6}$	$9.9999 \times 10^{-1}$
$1.5075 \times 10^1$	$2.0300 \times 10^2$	$7.8796 \times 10^{-6}$	$9.9999 \times 10^{-1}$
$2.0100 \times 10^1$	$2.0300 \times 10^2$	$7.8796 \times 10^{-6}$	$9.9999 \times 10^{-1}$
$2.5124 \times 10^1$	$2.0300 \times 10^2$	$7.8796 \times 10^{-6}$	$9.9999 \times 10^{-1}$
$3.5174 \times 10^1$	$2.0300 \times 10^2$	$7.8796 \times 10^{-6}$	$9.9999 \times 10^{-1}$
$5.0249 \times 10^1$	$2.0300 \times 10^2$	$7.8796 \times 10^{-6}$	$9.9999 \times 10^{-1}$
$1.0050 \times 10^2$	$2.0300 \times 10^2$	$7.8796 \times 10^{-6}$	$9.9999 \times 10^{-1}$
$1.5075 \times 10^2$	$2.0300 \times 10^2$	$7.8796 \times 10^{-6}$	$9.9999 \times 10^{-1}$
$2.0100 \times 10^2$	$2.0300 \times 10^2$	$7.8796 \times 10^{-6}$	$9.9999 \times 10^{-1}$
$2.5124 \times 10^2$	$2.0300 \times 10^2$	$7.8796 \times 10^{-6}$	$9.9999 \times 10^{-1}$
$3.5174 \times 10^2$	$2.0300 \times 10^2$	$7.8796 \times 10^{-6}$	$9.9999 \times 10^{-1}$
$5.0249 \times 10^2$	$2.0300 \times 10^2$	$7.8796 \times 10^{-6}$	$9.9999 \times 10^{-1}$
$1.0050 \times 10^3$	$2.0300 \times 10^2$	$7.8796 \times 10^{-6}$	$9.9999 \times 10^{-1}$
$1.5075 \times 10^3$	$2.0300 \times 10^2$	$7.8796 \times 10^{-6}$	$9.9999 \times 10^{-1}$
$2.0100 \times 10^3$	$2.0300 \times 10^2$	$7.8796 \times 10^{-6}$	$9.9999 \times 10^{-1}$
$2.5124 \times 10^3$	$2.0300 \times 10^2$	$7.8796 \times 10^{-6}$	$9.9999 \times 10^{-1}$
$3.5174 \times 10^3$	$2.0300 \times 10^2$	$7.8796 \times 10^{-6}$	$9.9999 \times 10^{-1}$
$5.0249 \times 10^3$	$2.0300 \times 10^2$	$7.8796 \times 10^{-6}$	$9.9999 \times 10^{-1}$
$7.5247 \times 10^3$	$2.0300 \times 10^2$	$7.8796 \times 10^{-6}$	$9.9999 \times 10^{-1}$
$7.5373 \times 10^3$	$2.0311 \times 10^2$	$7.9180 \times 10^{-6}$	$9.9999 \times 10^{-1}$
$1.0050 \times 10^4$	$2.2072 \times 10^2$	$7.1484 \times 10^{-5}$	$9.9993 \times 10^{-1}$
$1.1017 \times 10^4$	$2.2600 \times 10^2$	$1.6833 \times 10^{-4}$	$9.9983 \times 10^{-1}$
$1.2562 \times 10^4$	$2.3443 \times 10^2$	$3.4760 \times 10^{-4}$	$9.9965 \times 10^{-1}$
$1.5075 \times 10^4$	$2.4479 \times 10^2$	$9.1247 \times 10^{-4}$	$9.9909 \times 10^{-1}$
$1.7587 \times 10^4$	$2.5254 \times 10^2$	$1.6120 \times 10^{-3}$	$9.9839 \times 10^{-1}$
$2.0100 \times 10^4$	$2.5849 \times 10^2$	$2.4013 \times 10^{-3}$	$9.9760 \times 10^{-1}$
$2.2612 \times 10^4$	$2.6324 \times 10^2$	$3.1905 \times 10^{-3}$	$9.9681 \times 10^{-1}$
$2.5016 \times 10^4$	$2.6700 \times 10^2$	$3.9457 \times 10^{-3}$	$9.9605 \times 10^{-1}$
$2.5124 \times 10^4$	$2.6717 \times 10^2$	$3.9841 \times 10^{-3}$	$9.9602 \times 10^{-1}$
$2.7637 \times 10^4$	$2.7051 \times 10^2$	$5.0553 \times 10^{-3}$	$9.9494 \times 10^{-1}$
$3.0149 \times 10^4$	$2.7340 \times 10^2$	$6.3234 \times 10^{-3}$	$9.9368 \times 10^{-1}$
$3.2662 \times 10^4$	$2.7598 \times 10^2$	$7.2918 \times 10^{-3}$	$9.9271 \times 10^{-1}$
$3.5174 \times 10^4$	$2.7831 \times 10^2$	$8.2867 \times 10^{-3}$	$9.9171 \times 10^{-1}$
$3.6430 \times 10^4$	$2.7940 \times 10^2$	$8.8656 \times 10^{-3}$	$9.9113 \times 10^{-1}$
$3.7154 \times 10^4$	$2.8000 \times 10^2$	$9.1997 \times 10^{-3}$	$9.9080 \times 10^{-1}$
$3.7687 \times 10^4$	$2.8044 \times 10^2$	$9.4394 \times 10^{-3}$	$9.9056 \times 10^{-1}$
$3.8943 \times 10^4$	$2.8144 \times 10^2$	$9.9618 \times 10^{-3}$	$9.9004 \times 10^{-1}$
$4.0199 \times 10^4$	$2.8240 \times 10^2$	$1.0487 \times 10^{-2}$	$9.8951 \times 10^{-1}$
$4.1455 \times 10^4$	$2.8333 \times 10^2$	$1.1196 \times 10^{-2}$	$9.8880 \times 10^{-1}$
$4.2711 \times 10^4$	$2.8422 \times 10^2$	$1.2286 \times 10^{-2}$	$9.8771 \times 10^{-1}$
$4.3968 \times 10^4$	$2.8508 \times 10^2$	$1.3786 \times 10^{-2}$	$9.8621 \times 10^{-1}$
$4.5224 \times 10^4$	$2.8592 \times 10^2$	$1.5477 \times 10^{-2}$	$9.8452 \times 10^{-1}$
$4.6480 \times 10^4$	$2.8672 \times 10^2$	$1.7054 \times 10^{-2}$	$9.8295 \times 10^{-1}$
$4.7736 \times 10^4$	$2.8751 \times 10^2$	$1.8293 \times 10^{-2}$	$9.8171 \times 10^{-1}$
$4.8993 \times 10^4$	$2.8826 \times 10^2$	$1.8689 \times 10^{-2}$	$9.8131 \times 10^{-1}$
$5.0249 \times 10^4$	$2.8900 \times 10^2$	$1.8947 \times 10^{-2}$	$9.8105 \times 10^{-1}$

Table A.19: **Atmospheric structure for 1 bar of N<sub>2</sub>**  
GAM Profile

P (Pa)	T (K)	H <sub>2</sub> O (mass fraction)	N <sub>2</sub> (mass fraction)
$1.0025 \times 10^1$	$2.0300 \times 10^2$	$4.3187 \times 10^{-6}$	$9.9999 \times 10^{-1}$
$3.0075 \times 10^1$	$2.0300 \times 10^2$	$4.3187 \times 10^{-6}$	$9.9999 \times 10^{-1}$
$4.0100 \times 10^1$	$2.0300 \times 10^2$	$4.3187 \times 10^{-6}$	$9.9999 \times 10^{-1}$
$5.0124 \times 10^1$	$2.0300 \times 10^2$	$4.3187 \times 10^{-6}$	$9.9999 \times 10^{-1}$
$7.0174 \times 10^1$	$2.0300 \times 10^2$	$4.3187 \times 10^{-6}$	$9.9999 \times 10^{-1}$
$1.0025 \times 10^2$	$2.0300 \times 10^2$	$4.3187 \times 10^{-6}$	$9.9999 \times 10^{-1}$
$2.0050 \times 10^2$	$2.0300 \times 10^2$	$4.3187 \times 10^{-6}$	$9.9999 \times 10^{-1}$
$3.0075 \times 10^2$	$2.0300 \times 10^2$	$4.3187 \times 10^{-6}$	$9.9999 \times 10^{-1}$
$4.0100 \times 10^2$	$2.0300 \times 10^2$	$4.3187 \times 10^{-6}$	$9.9999 \times 10^{-1}$
$5.0124 \times 10^2$	$2.0300 \times 10^2$	$4.3187 \times 10^{-6}$	$9.9999 \times 10^{-1}$
$7.0174 \times 10^2$	$2.0300 \times 10^2$	$4.3187 \times 10^{-6}$	$9.9999 \times 10^{-1}$
$1.0025 \times 10^3$	$2.0300 \times 10^2$	$4.3187 \times 10^{-6}$	$9.9999 \times 10^{-1}$
$2.0050 \times 10^3$	$2.0300 \times 10^2$	$4.3187 \times 10^{-6}$	$9.9999 \times 10^{-1}$
$3.0075 \times 10^3$	$2.0300 \times 10^2$	$4.3187 \times 10^{-6}$	$9.9999 \times 10^{-1}$
$4.0100 \times 10^3$	$2.0300 \times 10^2$	$4.3187 \times 10^{-6}$	$9.9999 \times 10^{-1}$
$5.0124 \times 10^3$	$2.0300 \times 10^2$	$4.3187 \times 10^{-6}$	$9.9999 \times 10^{-1}$
$7.0174 \times 10^3$	$2.0300 \times 10^2$	$4.3187 \times 10^{-6}$	$9.9999 \times 10^{-1}$
$1.0025 \times 10^4$	$2.0300 \times 10^2$	$4.3187 \times 10^{-6}$	$9.9999 \times 10^{-1}$
$1.5037 \times 10^4$	$2.0300 \times 10^2$	$4.3187 \times 10^{-6}$	$9.9999 \times 10^{-1}$
$2.0050 \times 10^4$	$2.0300 \times 10^2$	$4.3187 \times 10^{-6}$	$9.9999 \times 10^{-1}$
$2.1443 \times 10^4$	$2.0300 \times 10^2$	$4.3187 \times 10^{-6}$	$9.9999 \times 10^{-1}$
$2.5062 \times 10^4$	$2.1275 \times 10^2$	$1.2022 \times 10^{-5}$	$9.9999 \times 10^{-1}$
$3.0075 \times 10^4$	$2.2434 \times 10^2$	$4.6206 \times 10^{-5}$	$9.9995 \times 10^{-1}$
$3.0902 \times 10^4$	$2.2600 \times 10^2$	$5.9372 \times 10^{-5}$	$9.9994 \times 10^{-1}$
$3.5087 \times 10^4$	$2.3439 \times 10^2$	$1.2202 \times 10^{-4}$	$9.9988 \times 10^{-1}$
$4.0100 \times 10^4$	$2.4306 \times 10^2$	$2.6402 \times 10^{-4}$	$9.9974 \times 10^{-1}$
$4.5112 \times 10^4$	$2.5048 \times 10^2$	$4.8188 \times 10^{-4}$	$9.9952 \times 10^{-1}$
$5.0124 \times 10^4$	$2.5677 \times 10^2$	$7.7779 \times 10^{-4}$	$9.9922 \times 10^{-1}$
$5.5137 \times 10^4$	$2.6212 \times 10^2$	$1.2086 \times 10^{-3}$	$9.9879 \times 10^{-1}$
$6.0149 \times 10^4$	$2.6668 \times 10^2$	$1.7765 \times 10^{-3}$	$9.9822 \times 10^{-1}$
$6.0554 \times 10^4$	$2.6700 \times 10^2$	$1.8262 \times 10^{-3}$	$9.9817 \times 10^{-1}$
$6.5162 \times 10^4$	$2.7063 \times 10^2$	$2.3816 \times 10^{-3}$	$9.9762 \times 10^{-1}$
$7.0174 \times 10^4$	$2.7408 \times 10^2$	$3.0298 \times 10^{-3}$	$9.9697 \times 10^{-1}$
$7.2680 \times 10^4$	$2.7566 \times 10^2$	$3.3666 \times 10^{-3}$	$9.9663 \times 10^{-1}$
$7.5187 \times 10^4$	$2.7716 \times 10^2$	$3.7070 \times 10^{-3}$	$9.9629 \times 10^{-1}$
$7.7693 \times 10^4$	$2.7859 \times 10^2$	$4.0392 \times 10^{-3}$	$9.9596 \times 10^{-1}$
$8.0199 \times 10^4$	$2.7995 \times 10^2$	$4.3754 \times 10^{-3}$	$9.9562 \times 10^{-1}$
$8.0297 \times 10^4$	$2.8000 \times 10^2$	$4.3896 \times 10^{-3}$	$9.9561 \times 10^{-1}$
$8.2705 \times 10^4$	$2.8125 \times 10^2$	$4.7962 \times 10^{-3}$	$9.9520 \times 10^{-1}$
$8.5211 \times 10^4$	$2.8249 \times 10^2$	$5.3959 \times 10^{-3}$	$9.9460 \times 10^{-1}$
$8.7718 \times 10^4$	$2.8368 \times 10^2$	$6.1941 \times 10^{-3}$	$9.9381 \times 10^{-1}$
$9.0224 \times 10^4$	$2.8483 \times 10^2$	$7.0992 \times 10^{-3}$	$9.9290 \times 10^{-1}$
$9.2730 \times 10^4$	$2.8593 \times 10^2$	$7.9759 \times 10^{-3}$	$9.9202 \times 10^{-1}$
$9.5236 \times 10^4$	$2.8699 \times 10^2$	$8.7132 \times 10^{-3}$	$9.9129 \times 10^{-1}$
$9.7743 \times 10^4$	$2.8801 \times 10^2$	$9.0575 \times 10^{-3}$	$9.9094 \times 10^{-1}$
$1.0025 \times 10^5$	$2.8900 \times 10^2$	$9.3308 \times 10^{-3}$	$9.9067 \times 10^{-1}$

]Atmospheric structure for 2 bar of N<sub>2</sub>

## GAM Profile

P (Pa)	T (K)	H <sub>2</sub> O (mass fraction)	N <sub>2</sub> (mass fraction)
2.0025×10 <sup>1</sup>	2.0300×10 <sup>2</sup>	1.6596×10 <sup>-6</sup>	9.9999×10 <sup>-1</sup>
6.0075×10 <sup>1</sup>	2.0300×10 <sup>2</sup>	1.6596×10 <sup>-6</sup>	9.9999×10 <sup>-1</sup>
8.0100×10 <sup>1</sup>	2.0300×10 <sup>2</sup>	1.6596×10 <sup>-6</sup>	9.9999×10 <sup>-1</sup>
1.0012×10 <sup>2</sup>	2.0300×10 <sup>2</sup>	1.6596×10 <sup>-6</sup>	9.9999×10 <sup>-1</sup>
1.4017×10 <sup>2</sup>	2.0300×10 <sup>2</sup>	1.6596×10 <sup>-6</sup>	9.9999×10 <sup>-1</sup>
2.0025×10 <sup>2</sup>	2.0300×10 <sup>2</sup>	1.6596×10 <sup>-6</sup>	9.9999×10 <sup>-1</sup>
4.0050×10 <sup>2</sup>	2.0300×10 <sup>2</sup>	1.6596×10 <sup>-6</sup>	9.9999×10 <sup>-1</sup>
6.0075×10 <sup>2</sup>	2.0300×10 <sup>2</sup>	1.6596×10 <sup>-6</sup>	9.9999×10 <sup>-1</sup>
8.0100×10 <sup>2</sup>	2.0300×10 <sup>2</sup>	1.6596×10 <sup>-6</sup>	9.9999×10 <sup>-1</sup>
1.0012×10 <sup>3</sup>	2.0300×10 <sup>2</sup>	1.6596×10 <sup>-6</sup>	9.9999×10 <sup>-1</sup>
1.4017×10 <sup>3</sup>	2.0300×10 <sup>2</sup>	1.6596×10 <sup>-6</sup>	9.9999×10 <sup>-1</sup>
2.0025×10 <sup>3</sup>	2.0300×10 <sup>2</sup>	1.6596×10 <sup>-6</sup>	9.9999×10 <sup>-1</sup>
4.0050×10 <sup>3</sup>	2.0300×10 <sup>2</sup>	1.6596×10 <sup>-6</sup>	9.9999×10 <sup>-1</sup>
6.0075×10 <sup>3</sup>	2.0300×10 <sup>2</sup>	1.6596×10 <sup>-6</sup>	9.9999×10 <sup>-1</sup>
8.0100×10 <sup>3</sup>	2.0300×10 <sup>2</sup>	1.6596×10 <sup>-6</sup>	9.9999×10 <sup>-1</sup>
1.0012×10 <sup>4</sup>	2.0300×10 <sup>2</sup>	1.6596×10 <sup>-6</sup>	9.9999×10 <sup>-1</sup>
1.4017×10 <sup>4</sup>	2.0300×10 <sup>2</sup>	1.6596×10 <sup>-6</sup>	9.9999×10 <sup>-1</sup>
2.0025×10 <sup>4</sup>	2.0300×10 <sup>2</sup>	1.6596×10 <sup>-6</sup>	9.9999×10 <sup>-1</sup>
3.0037×10 <sup>4</sup>	2.0300×10 <sup>2</sup>	1.6596×10 <sup>-6</sup>	9.9999×10 <sup>-1</sup>
4.0050×10 <sup>4</sup>	2.0300×10 <sup>2</sup>	1.6596×10 <sup>-6</sup>	9.9999×10 <sup>-1</sup>
5.0062×10 <sup>4</sup>	2.0300×10 <sup>2</sup>	1.6596×10 <sup>-6</sup>	9.9999×10 <sup>-1</sup>
5.0885×10 <sup>4</sup>	2.0300×10 <sup>2</sup>	1.6596×10 <sup>-6</sup>	9.9999×10 <sup>-1</sup>
6.0075×10 <sup>4</sup>	2.1323×10 <sup>2</sup>	5.5496×10 <sup>-6</sup>	9.9999×10 <sup>-1</sup>
7.0087×10 <sup>4</sup>	2.2310×10 <sup>2</sup>	1.6186×10 <sup>-5</sup>	9.9998×10 <sup>-1</sup>
7.3373×10 <sup>4</sup>	2.2600×10 <sup>2</sup>	2.3852×10 <sup>-5</sup>	9.9998×10 <sup>-1</sup>
8.0100×10 <sup>4</sup>	2.3194×10 <sup>2</sup>	3.9254×10 <sup>-5</sup>	9.9996×10 <sup>-1</sup>
9.0112×10 <sup>4</sup>	2.3991×10 <sup>2</sup>	8.1710×10 <sup>-5</sup>	9.9992×10 <sup>-1</sup>
1.0012×10 <sup>5</sup>	2.4711×10 <sup>2</sup>	1.5223×10 <sup>-4</sup>	9.9985×10 <sup>-1</sup>
1.1014×10 <sup>5</sup>	2.5357×10 <sup>2</sup>	2.7372×10 <sup>-4</sup>	9.9973×10 <sup>-1</sup>
1.2015×10 <sup>5</sup>	2.5937×10 <sup>2</sup>	4.6244×10 <sup>-4</sup>	9.9954×10 <sup>-1</sup>
1.3016×10 <sup>5</sup>	2.6455×10 <sup>2</sup>	7.0383×10 <sup>-4</sup>	9.9930×10 <sup>-1</sup>
1.3548×10 <sup>5</sup>	2.6700×10 <sup>2</sup>	8.6121×10 <sup>-4</sup>	9.9914×10 <sup>-1</sup>
1.4017×10 <sup>5</sup>	2.6917×10 <sup>2</sup>	1.0103×10 <sup>-3</sup>	9.9899×10 <sup>-1</sup>
1.4518×10 <sup>5</sup>	2.7129×10 <sup>2</sup>	1.1975×10 <sup>-3</sup>	9.9880×10 <sup>-1</sup>
1.5019×10 <sup>5</sup>	2.7330×10 <sup>2</sup>	1.3995×10 <sup>-3</sup>	9.9860×10 <sup>-1</sup>
1.5519×10 <sup>5</sup>	2.7520×10 <sup>2</sup>	1.5814×10 <sup>-3</sup>	9.9842×10 <sup>-1</sup>

# Bibliography

- Abbot, D. S., Voigt, A., Li, D., Le Hir, G., Pierrehumbert, R. T., Branson, M., Pollard, D., and Koll, D. D. B. (2013). Robust elements of Snowball Earth atmospheric circulation and oases for life. *J. Geophys. Res.-Atmos.*, 118(12):6017–6027.
- Beerling, D., Berner, R. A., Mackenzie, F. T., Harfoot, M. B., and Pyle, J. A. (2009). Methane and the CH<sub>4</sub>-related greenhouse effect over the past 400 million years. *Am. J. Sci.*, 309(2):97–113.
- Buick, R. (2007). Did the Proterozoic ‘Canfield Ocean’ cause a laughing gas greenhouse? *Geobiology*, 5(2):97–100.
- Byrne, B. and Goldblatt, C. (2014). Radiative forcing at high concentrations of well-mixed greenhouse gases. *Geophys. Res. Lett.*, 41.
- Charnay, B., Forget, F., Wordsworth, R., Leconte, J., Millour, E., Codron, F., and Spiga, A. (2013). Exploring the faint young Sun problem and the possible climates of the Archean Earth with a 3-D GCM. *J. Geophys. Res. Atmos.*, 118:10414.
- Collins, W. D., Ramaswamy, V., Schwarzkopf, M. D., Sun, Y., Portmann, R. W., Fu, Q., Casanova, S. E. B., Dufresne, J. L., Fillmore, D. W., Forster, P. M. D., Galin, V. Y., Gohar, L. K., Ingram, W. J., Kratz, D. P., Lefebvre, M. P., Li, J., Marquet, P., Oinas, V., Tsushima, Y., Uchiyama, T., and Zhong, W. Y. (2006). Radiative forcing by well-mixed greenhouse gases: Estimates from climate models in the Intergovernmental Panel on Climate Change (IPCC) Fourth Assessment Report (AR4). *J. Geophys. Res.*, 111(D14).
- Crisp, D. (1997). Absorption of sunlight by water vapor in cloudy conditions: A partial explanation for the cloud absorption anomaly. *Geophys. Res. Lett.*, 24(5):571–574.

- Donn, W. L., Donn, B. D., and Valentine, W. G. (1965). On the early history of the earth. *Geol. Soc. Am. Bull.*, 76:287–306.
- Driese, S. G., Jirsa, M. A., Ren, M., Brantley, S. L., Sheldon, N. D., Parker, D., and Schmitz, M. (2011). Neoproterozoic paleoweathering of tonalite and metabasalt: Implications for reconstructions of 2.69 Ga early terrestrial ecosystems and paleoatmospheric chemistry. *Precambrian Res.*, 189(1-2):1–17.
- Freckleton, R., Highwood, E., Shine, K., Wild, O., Law, K., and Sanderson, M. (1998). Greenhouse gas radiative forcing: Effects of averaging and inhomogeneities in trace gas distribution. *Q. J. Roy. Meteor. Soc.*, 124(550, Part b):2099–2127.
- Fu, Q. and Liou, K. (1992). On the correlated K-distribution method for radiative-transfer in nonhomogeneous atmospheres. *J. Atmos. Sci.*, 49(22):2139–2156.
- Goldblatt, C., Claire, M. W., Lenton, T. M., Matthews, A. J., Watson, A. J., and Zahnle, K. J. (2009a). Nitrogen-enhanced greenhouse warming on early Earth. *Nat. Geosci.*, 2(12):891–896.
- Goldblatt, C., Lenton, T. M., and Watson, A. J. (2006). Bistability of atmospheric oxygen and the Great Oxidation. *Nature*, 443(7112):683–686.
- Goldblatt, C., Lenton, T. M., and Watson, A. J. (2009b). An evaluation of the long-wave radiative transfer code used in the Met Office Unified Model. *Quarterly Journal of The Royal Meteorological Society*, 135(640):619–633.
- Goldblatt, C. and Zahnle, K. J. (2011a). Clouds and the Faint Young Sun Paradox. *Clim. Past*, 7(1):203–220.
- Goldblatt, C. and Zahnle, K. J. (2011b). Faint young Sun paradox remains. *Nature*, 474(7349):E3–E4.
- Goody, R., West, R., Chen, L., and Crisp, D. (1989). The correlated-K method for radiation calculations in nonhomogeneous atmospheres. *J. Quant. Spectrosc. Ra.*, 42(6):539–550.
- Goody, R. and Yung, Y. (1995). *Atmospheric radiation: theoretical basis*. Oxford University Press, USA.

- Gough, D. (1981). Solar interior structure and luminosity variations. *Sol. Phys.*, 74(1):21–34.
- Hale, G. M. and Querry, M. R. (1973). Optical Constants of Water in the 200–nm to 200- $\mu\text{m}$  Wavelength Region. *Applied Optics*, 12(3):555–563.
- Halevy, I., Pierrehumbert, R. T., and Schrag, D. P. (2009a). Radiative transfer in CO<sub>2</sub>-rich paleoatmospheres. *J. Geophys. Res.*, 114.
- Halevy, I., Pierrehumbert, R. T., and Schrag, D. P. (2009b). Radiative transfer in CO<sub>2</sub>-rich paleoatmospheres. *J. Geophys. Res. Atmos.*, 114.
- Halthore, R., Crisp, D., Schwartz, S., Anderson, G., Berk, A., Bonnel, B., Boucher, O., Chang, F., Chou, M., Clothiaux, E., Dubuisson, P., Fomin, B., Fouquart, Y., Freidenreich, S., Gautier, C., Kato, S., Laszlo, I., Li, Z., Mather, J., Plana-Fattori, A., Ramaswamy, V., Ricchiazzi, P., Shiren, Y., Trishchenko, A., and Wiscombe, W. (2005). Intercomparison of shortwave radiative transfer codes and measurements. *J. Geophys. Res.*, 110(D11).
- Hansen, J., Fing, I., Lacis, A., Rind, D., Lebedeff, S., Ruedy, R., Russell, G., and Stone, P. (1988). Global climate changes as forecast by Goddard Institute for space studies 3-dimensional model. *J. Geophys. Res.-Atmos.*, 93(D8):9341–9364.
- Hansen, J., Sato, M., and Ruedy, R. (1997). Radiative forcing and climate response. *J. Geophys. Res.*, 102(D6):6831–6864.
- Hansen, J., Sato, M., Ruedy, R., Nazarenko, L., Lacis, A., Schmidt, G., Russell, G., Aleinov, I., Bauer, M., Bauer, S., Bell, N., Cairns, B., Canuto, V., Chandler, M., Cheng, Y., Del Genio, A., Faluvegi, G., Fleming, E., Friend, A., Hall, T., Jackman, C., Kelley, M., Kiang, N., Koch, D., Lean, J., Lerner, J., Lo, K., Menon, S., Miller, R., Minnis, P., Novakov, T., Oinas, V., Perlwitz, J., Perlwitz, J., Rind, D., Romanou, A., Shindell, D., Stone, P., Sun, S., Tausnev, N., Thresher, D., Wielicki, B., Wong, T., Yao, M., and Zhang, S. (2005). Efficacy of climate forcings. *J. Geophys. Res.-Atmos.*, 110(D18).
- Haqq-Misra, J. D., Domagal-Goldman, S. D., Kasting, P. J., and Kasting, J. F. (2008). A Revised, Hazy Methane Greenhouse for the Archean Earth. *Astrobiology*, 8(6):1127–1137.

- Hattori, S., Danielache, S. O., Johnson, M. S., Schmidt, J. A., Kjaergaard, H. G., Toyoda, S., Ueno, Y., and Yoshida, N. (2011). Ultraviolet absorption cross sections of carbonyl sulfide isotopologues (OCS)-S-32, (OCS)-S-33, (OCS)-S-34 and (OCS)-C-13: isotopic fractionation in photolysis and atmospheric implications. *Atmos. Chem. Phys.*, 11(19):10293–10303.
- Hua, Z., Guangyu, S., and Yi, L. (2008). The effects of line-wing cutoff in LBL integration on radiation calculations. *Acta Meteorologica Sinica*, 22(2):248–255.
- IPCC (1990). *Climate Change: The IPCC Scientific Assessment*. Cambridge University Press, Cambridge, United Kingdom and New York, NY, USA.
- IPCC (2001). *Climate Change 2001: The Scientific Basis. Contribution of Working Group I to the Third Assessment Report of the Intergovernmental Panel on Climate Change*. Cambridge University Press, Cambridge, United Kingdom and New York, NY, USA.
- IPCC (2013). *Climate Change 2013: The Scientific Basis. Contribution of Working Group I to the Fifth Assessment Report of the Intergovernmental Panel on Climate Change*. Cambridge University Press, Cambridge, U.K. and New York, NY, USA.
- Kasting, J. (1982). Stability of ammonia in the primitive terrestrial atmosphere. *J. Geophys. Res.-Oc. Atm.*, 87(NC4):3091–3098.
- Kasting, J. (2005). Methane and climate during the Precambrian era. *Precambrian Res.*, 137(3-4):119–129.
- Kasting, J., Pollack, J., and Crisp, D. (1984). Effects of high CO<sub>2</sub> levels on surface-temperature and atmospheric oxidation-state of the early Earth. *J. Atmos. Chem.*, 1(4):403–428.
- Kasting, J. F. (2013). How Was Early Earth Kept Warm? *Science*, 339(6115):44–45.
- Kavanagh, L. and Goldblatt, C. (2013). The som palaeobarometry method: A critical analysis. Abstract P21B-1719 presented at 2012 Fall Meeting, AGU, San Francisco, Calif., 3-7 Dec.
- Kiehl, J. and Dickinson, R. (1987). A study of the radiative effects of enhanced atmospheric CO<sub>2</sub> and CH<sub>4</sub> on early Earth surface temperatures. *J. Geophys. Res. Atmos.*, 92(D3):2991–2998.

- Kienert, H., Feulner, G., and Petoukhov, V. (2012). Faint young Sun problem more severe due to ice-albedo feedback and higher rotation rate of the early Earth. *Geophys. Res. Lett.*, 39.
- Kuhn, W. and Atreya, S. (1979). Ammonia photolysis and the greenhouse effect in the primordial atmosphere of the Earth. *Icarus*, 37(1):207–213.
- Kurten, T., Zhou, L., Makkonen, R., Merikanto, J., Raisanen, P., Boy, M., Richards, N., Rap, A., Smolander, S., Sogachev, A., Guenther, A., Mann, G. W., Carslaw, K., and Kulmala, M. (2011). Large methane releases lead to strong aerosol forcing and reduced cloudiness. *Atmos. Chem. Phys.*, 11(14):6961–6969.
- Ma, Q., Tipping, R. H., and Leforestier, C. (2008). Temperature dependences of mechanisms responsible for the water-vapor continuum absorption. I. Far wings of allowed lines. *Journal of Chemical Physics*, 128(12).
- Marty, B., Zimmermann, L., Pujol, M., Burgess, R., and Philippot, P. (2013). Nitrogen Isotopic Composition and Density of the Archean Atmosphere. *Science*, 342(6154):101–104.
- Meadows, V. and Crisp, D. (1996). Ground-based near-infrared observations of the Venus nightside: The thermal structure and water abundance near the surface. *J. Geophys. Res-Planet*, 101(E2):4595–4622.
- Meinshausen, M., Smith, S. J., Calvin, K., Daniel, J. S., Kainuma, M. L. T., Lamarque, J.-F., Matsumoto, K., Montzka, S. A., Raper, S. C. B., Riahi, K., Thomson, A., Velders, G. J. M., and van Vuuren, D. P. P. (2011). The RCP greenhouse gas concentrations and their extensions from 1765 to 2300. *Climatic Change*, 109(1-2, SI):213–241.
- Melsheimer, C., Verdes, C., Buehler, S., Emde, C., Eriksson, P., Feist, D., Ichizawa, S., John, V., Kasai, Y., Kopp, G., Koulev, N., Kuhn, T., Lemke, O., Ochiai, S., Schreier, F., Sreerekha, T., Suzuki, M., Takahashi, C., Tsujimaru, S., and Urban, J. (2005). Intercomparison of general purpose clear sky atmospheric radiative transfer models for the millimeter/submillimeter spectral range. *RADIO Science*, 40(1).
- Myhre, G. and Stordal, F. (1997). Role of spatial and temporal variations in the computation of radiative forcing and GWP. *J. Geophys. Res.*, 102(D10):11181–11200.

- O'Brien, D. and Dilley, A. (2000). Infrared cooling of the atmosphere: accuracy of correlated k-distributions. *J. Quant. Spectrosc. Ra.*, 64(5):483–497.
- Pavlov, A., Kasting, J., Brown, L., Rages, K., and Freedman, R. (2000). Greenhouse warming by CH<sub>4</sub> in the atmosphere of early Earth. *J. Geophys. Res-Planet*, 105(E5):11981–11990.
- Petty, G. (2006). *A first course in atmospheric radiation*. Sundog Pub.
- Pierrehumbert, R. (2010). *Principles of planetary climate*. Cambridge Univ Pr.
- Ptashnik, I. V., Shine, K. P., and Vigan, A. A. (2011). Water vapour self-continuum and water dimers: 1. Analysis of recent work. *J. Quant. Spectrosc. Ra.*, 112(8):1286–1303.
- Ramanathan, V., Callis, L., Cess, R., Hansen, J., Isaken, I., Kuhn, W., Lacis, A., Luther, F., Mahlman, J., Reck, R., and Schlesinger, M. (1987). Climate-Chemical Interactions and Effects of Changing Atmospheric Trace Gases. *Review Of Geophysics*, 25(7):1441–1482.
- Ramanathan, V. and Coakley, J. (1978). Climate modeling through radiative-convective models. *Reviews of geophysics*, 16(4):465–489.
- Rienecker, M. M., Suarez, M. J., Gelaro, R., Todling, R., Bacmeister, J., Liu, E., Bosilovich, M. G., Schubert, S. D., Takacs, L., Kim, G.-K., Bloom, S., Chen, J., Collins, D., Conaty, A., Da Silva, A., Gu, W., Joiner, J., Koster, R. D., Lucchesi, R., Molod, A., Owens, T., Pawson, S., Pegion, P., Redder, C. R., Reichle, R., Robertson, F. R., Ruddick, A. G., Sienkiewicz, M., and Woollen, J. (2011). MERRA: NASA's Modern-Era Retrospective Analysis for Research and Applications. *J. Climate*, 24(14):3624–3648.
- Roberson, A. L., Roadt, J., Halevy, I., and Kasting, J. F. (2011). Greenhouse warming by nitrous oxide and methane in the Proterozoic Eon. *Geobiology*, 9(4):313–320.
- Rondanelli, R. and Lindzen, R. S. (2010). Can thin cirrus clouds in the tropics provide a solution to the faint young Sun paradox? *J. Geophys. Res.*, 115.
- Rosing, M. T., Bird, D. K., Sleep, N. H., and Bjerrum, C. J. (2010). No climate paradox under the faint early Sun. *NATURE*, 464(7289):744–U117.

- Rossow, W., Zhang, Y., and Wang, J. (2005). A statistical model of cloud vertical structure based on reconciling cloud layer amounts inferred from satellites and radiosonde humidity profiles. *J. Climate*, 18(17):3587–3605.
- Rothman, L. S., Gordon, I. E., Babikov, Y., Barbe, A., Benner, D. C., Bernath, P. F., Birk, M., Bizzocchi, L., Boudon, V., Brown, L. R., Campargue, A., Chance, K., Cohen, E. A., Coudert, L. H., Devi, V. M., Drouin, B. J., Fayt, A., Flaud, J. M., Gamache, R. R., Harrison, J. J., Hartmann, J. M., Hill, C., Hodges, J. T., Jacquemart, D., Jolly, A., Lamouroux, J., Le Roy, R. J., Li, G., Long, D. A., Lyulin, O. M., Mackie, C. J., Massie, S. T., Mikhailenko, S., Mueller, H. S. P., Naumenko, O. V., Nikitin, A. V., Orphal, J., Perevalov, V., Perrin, A., Polovtseva, E. R., Richard, C., Smith, M. A. H., Starikova, E., Sung, K., Tashkun, S., Tennyson, J., Toon, G. C., Tyuterev, V. G., and Wagner, G. (2013). The HITRAN2012 molecular spectroscopic database. *J. Quant. Spectrosc. Ra.*, 130(SI):4–50.
- Rothman, L. S., Gordon, I. E., Barbe, A., Benner, D. C., Bernath, P. E., Birk, M., Boudon, V., Brown, L. R., Campargue, A., Champion, J. P., Chance, K., Coudert, L. H., Dana, V., Devi, V. M., Fally, S., Flaud, J. M., Gamache, R. R., Goldman, A., Jacquemart, D., Kleiner, I., Lacome, N., Lafferty, W. J., Mandin, J. Y., Massie, S. T., Mikhailenko, S. N., Miller, C. E., Moazzen-Ahmadi, N., Naumenko, O. V., Nikitin, A. V., Orphal, J., Perevalov, V. I., Perrin, A., Predoi-Cross, A., Rinsland, C. P., Rotger, M., Simeckova, M., Smith, M. A. H., Sung, K., Tashkun, S. A., Tennyson, J., Toth, R. A., Vandaele, A. C., and Vander Auwera, J. (2009). The HITRAN 2008 molecular spectroscopic database. *J. Quant. Spectrosc. Ra.*, 110(9-10):533–572.
- Royer, D. L. (2006). CO<sub>2</sub>-forced climate thresholds during the Phanerozoic. *Geochim. Cosmochim. Ac.*, 70(23):5665–5675.
- Russell, G. L., Lacis, A. A., Rind, D. H., Colose, C., and Opstbaum, R. F. (2013). Fast atmosphere-ocean model runs with large changes in CO<sub>2</sub>. *Geophys. Res. Lett.*, 40(21):5787–5792.
- Sagan, C. and Chyba, C. (1997). The early faint sun paradox: Organic shielding of ultraviolet-labile greenhouse gases. *Science*, 276(5316):1217–1221.
- Sagan, C. and Mullen, G. (1972). Earth and Mars - Evolution of atmospheres and surface temperatures. *Science*, 177(4043):52–&.

- Schmidt, G. and Shindell, D. (2003). Atmospheric composition, radiative forcing, and climate change as a consequence of a massive methane release from gas hydrates. *Paleoceanography*, 18(1).
- Shaffer, G., Olsen, S. M., and Pedersen, J. O. P. (2008). Presentation, calibration and validation of the low-order, DCESS Earth System Model (Version 1). *Geosci. Model Dev.*, 1(1):17–51.
- Sharpe, S., Johnson, T., Sams, R., Chu, P., Rhoderick, G., and Johnson, P. (2004). Gas-phase databases for quantitative infrared spectroscopy. *Appl. Spectrosc.*, 58(12):1452–1461.
- Shaviv, N. (2003). Toward a solution to the early faint Sun paradox: A lower cosmic ray flux from a stronger solar wind. *J. Geophys. Res.-Space*, 108(A12).
- Sheldon, N. (2006). Precambrian paleosols and atmospheric CO<sub>2</sub> levels. *Precambrian Res.*, 147(1-2):148–155.
- Shi, G. (1992). Radiative forcing and greenhouse effect due to the atmospheric trace gases. *Science in China (Series B)*, 35:217–229.
- Som, S., Catling, D. C., Jelte, P. H., Polivka, P. M., and Buick, R. (2012). Air density 2.7 billion years ago limited to less than twice modern levels by fossil raindrop imprints. *Nature*, ():.
- Tachiiri, K., Hargreaves, J. C., Annan, J. D., Oka, A., Abe-Ouchi, A., and Kawamiya, M. (2010). Development of a system emulating the global carbon cycle in Earth system models. *Geosci. Model Dev.*, 3(2):365–376.
- Thomas, G. and Stamnes, K. (2002). *Radiative transfer in the atmosphere and ocean*. Cambridge Univ Pr.
- Ueno, Y., Johnson, M. S., Danielache, S. O., Eskebjerg, C., Pandey, A., and Yoshida, N. (2009). Geological sulfur isotopes indicate elevated OCS in the Archean atmosphere, solving faint young sun paradox. *P. Natl. Acad. Sci. USA*, 106(35):14784–14789.
- von Paris, P., Rauer, H., Grenfell, J. L., Patzer, B., Hedelt, P., Stracke, B., Trautmann, T., and Schreier, F. (2008). Warming the early earth - CO<sub>2</sub> reconsidered. *Planet Space Sci.*, 56(9):1244–1259.

- Walker, J., Hays, P., and Kasting, J. (1981). A negative feedback mechanism for the longterm stabilization of Earth's surface temperature. *J. Geophys. Res.-Oc. Atm.*, 86(NC10):9776–9782.
- Weaver, A., Eby, M., Wiebe, E., Bitz, C., Duffy, P., Ewen, T., Fanning, A., Holland, M., MacFadyen, A., Matthews, H., Meissner, K., Saenko, O., Schmittner, A., Wang, H., and Yoshimori, M. (2001). The UVic Earth System Climate Model: Model description, climatology, and applications to past, present and future climates. *Atmos. Ocean.*, 39(4):361–428.
- West, R., Crisp, D., and Chen, L. (1990). Mapping Transformations for Broad-Band Atmospheric Radiation Calculations. *J. Quant. Spectrosc. Ra.*, 43(3):191–199.
- WMO (1985). *Atmospheric Ozone 1985 Assessment of Our Understanding of the Processes Controlling Its Present Distribution and Change*. WMO.
- WMO (1999). *Scientific Assessment of Ozone Depletion: 1998, Global Ozone Research and Monitoring Project*. WMO.
- Wolf, E. T. and Toon, O. B. (2013). Hospitable Archean Climates Simulated by a General Circulation Model. *Astrobiology*, 13(7):656–673.
- Wordsworth, R., Forget, F., and Eymet, V. (2010). Infrared collision-induced and far-line absorption in dense CO<sub>2</sub> atmospheres. *Icarus*, 210(2):992–997.
- Young, G. (1991). The geologic record of glaciation - Relevance to the climatic history of Earth. *Geosci. Can.*, 18(3):100–108.
- Zahnle, K. (1986). Photochemistry of methane and the formation of hydrocyanic acid (HCN) in the Earth's early atmosphere. *J. Geophys. Res.*, 91(D2):2819–2834.
- Zhang, H. and Shi, G. (2002). Numerical explanation for accurate radiative cooling rates resulting from the correlated k-distribution hypothesis. *J. Quant. Spectrosc. Ra.*, 74(3):299–306.